Correlation between SQUID and Fluxgate Magnetometer Data-sets for Geomagnetic Storms: Hermanus

by

Thabang-Kingsley Matladi

Thesis presented in partial fulfilment of the requirements for the degree of Master of Engineering (Research) in the Faculty of Engineering at Stellenbosch University

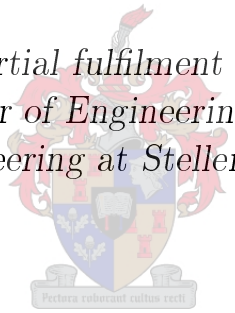

Department of Electrical and Electronic Engineering,
University of Stellenbosch,
Private Bag X1, Matieland 7602, South Africa.

Supervisors:

Prof Coenrad J. Fourie Mr. Daniel J. Gouws Mrs. Elda F. Saunderson

December 2013

Declaration

By submitting this thesis electronically, I declare that the entirety of the work contained therein is my own, original work, that I am the sole author thereof (save to the extent explicitly otherwise stated), that reproduction and publication thereof by Stellenbosch University will not infringe any third party rights and that I have not previously in its entirety or in part submitted it for obtaining any qualification.

Date: December 2013 .....

Abstract

Correlation between SQUID and Fluxgate Magnetometer Data-sets for Geomagnetic Storms: Hermanus

T. K. Matladi

Department of Electrical and Electronic Engineering,
University of Stellenbosch,
Private Bag X1, Matieland 7602, South Africa.

Thesis: M. Eng. (Elec)

December 2013

Superconducting QUantum Interference Devices (SQUIDs) are fairly recent types of magnetometers that use flux quantization combined with Josephson tunnelling to detect very faint ($< 10^{-15}$ T) magnetic fields. Recent scientific studies have shown that these highly sensitive magnetometers, located in an ultra-low-noise environment, are capable of observing Earth-ionosphere couplings, such as P waves emitted during earthquakes or magnetic storms in the upper atmosphere, S and T breathing modes of the Earth during quiet magnetic and seismic periods, signals in time correlating with sprites. Since SQUIDs are much more sensitive than conventional magnetometers, they are arguably the best tool for understanding space weather and natural hazards, whether they are produced from space or within the ionosphere by magnetic storms for instance, or natural disturbances, including magnetic disturbances produced by earthquakes or as a result of the dynamics of the earth's core.

A study was conducted at SANSA Space Science in Hermanus, Western Cape, in 2012, to find the correlation between SQUID and Fluxgate data-sets, with the aim of validating the use of a SQUID as a reliable instrument for Space Weather observations. In that study, SQUID data obtained from the Low Noise Laboratory (LSBB) in France was compared to Fluxgate data-sets from the three closest magnetic observatories to LSBB, namely Chambon la Forêt (France), Ebro (Spain) and Fürstenfeldbruck (Germany), all further than 500 km from LSBB. As a follow-up study, our aim is to correlate the SANSA Space Science SQUID data at Hermanus with Fluxgate magnetic data also recorded on-site (at Hermanus). There are notable differences between the previous study and the current study. In the previous study, the three-axis SQUID

used comprised of three low-T_c devices operated in liquid helium (4.2 K) in an underground, low noise environment shielded from most human interferences.

The SQUID magnetometer operated at Hermanus for the duration of this study is a high-T_c two-axis device (measuring the x and z components of the geomagnetic field). This SQUID magnetometer operates in liquid nitrogen (77 K), and is completely unshielded in the local geomagnetic field of about 26 μT. The environment is magnetically clean to observatory standards, but experiences more human interference than that at LSBB. The high-T_c SQUIDs also experience excessive 1/f noise at low frequencies which the low-T_c SQUIDs do not suffer from, but the big advantage of the current study is that the SQUIDs are located within 50 m from the observatory's fluxgate. We thus expect far better correlation between SQUID and fluxgate data than what was obtained in the previous study, which should improve the isolation of signals detected by the SQUID but not by the fluxgate.

Uittreksel

Korrelasie tussen SQUID en Fluxgate Magnetometer Datastelle vir Geomagnetiese Storms: Hermanus

("Correlation between SQUID and Fluxgate Magnetometer Data-sets for Geomagnetic Storms: Hermanus")

T. K. Matladi

Departement Elektries en Elektroniese Ingenieurswese,
Universiteit van Stellenbosch,
Privaatsak X1, Matieland 7602, Suid Afrika.

Tesis: M. Ing. (Navorsing) in Elektroniese Ingenieurswese

Desember 2013

SQUIDs (supergeleidende kwantuminterferensietoestelle) is redelik onlangse tipes magnetometers wat vloedkwantisering saam met Josephson-tonneling gebruik om baie klein ($< 10^{-15}$ T) magnetiese velde waar te neem. Onlangse wetenskaplike studies het getoon dat hierdie hoogs sensitiewe magnetometers die vermoë het om Aarde-ionosfeerkoppeling waar te neem wanneer dit in 'n ultra-laeruisomgewing geplaas word. Sodanige koppeling sluit in: P-golwe wat deur aardbewings or magnetiese storms in die boonste atmosfeer veroorsaak word; S- en T-asemhalingsmodusse van die Aarde gedurende stil magnetiese en seismiese periodes; en seine in tyd wat korreleer met weerligeffekte in die boonste atmosfeer. Aangesien SQUIDs heelwat meer sensistief is as konvensionele magnetometers, is dit moontlik die beste gereedskap om ruimteweer en geassosieerde natuurlike gevare mee te analiseer; hetsy sulke toestande veroorsaak word vanaf die ruimte (deur die son) of binne die ionosfeer deur magnetiese storms of natuurlike steurings wat deur aardbewings of die dinamika van die Aardkern veroorsaak word.

'n Studie is in 2012 gedoen by SANSA Space Science in Hermanus in die Wes-Kaap om die korrelasie tussen SQUID- en vloedhekdatastelle te vind met die doel om SQUIDs as betroubare instrumente vir ruimteweerwaarneming te bevestig. In daardie studie is SQUID-data verkry vanaf die Laeruis Ondergrondse Laboratorium (LSBB) in Frankryk, en is dit vergelyk met vloedhekdatastelle vanaf die drie naaste magnetiese observatoriums aan LSBB, naamlik: Chambon la Forêt (Frankryk), Ebro (Spanje) en Fürstenfeldbruck (Duitsland).

Al drie hierdie observatoriums is verder as 500 km vanaf LSBB. As 'n opvolgstudie is ons doelwit om SQUID- en vloedhekdata wat beide op die terrein van SANSA Space Science in Hermanus waargeneem word, te korreleer. Daar is merkbare verskille tussen hierdie en die vorige studies. In die vorige studie is 'n drie-as lae-T_c SQUID-magnetometer in vloeibare helium (4.2 K) in 'n laeruis ondergrondse laboratorium, afgeskerm teen menslike steurings, gebruik.

Die SQUID-magnetometer wat vir die duur van die huidige studie by Hermanus gebruik is, is 'n hoë-T_c twee-as toestel (wat die x- en z-komponente van die geomagnetiese veld meet). Hierdie SQUID-magnetometer opereer in vloeibare stikstof teen 77 K, sonder enige afskerming in die geomagnetiese veld van ongeveer 26 μT. Die omgewing is magneties skoon volgens observatoriumstandaarde, maar ondervind meer menslik-veroorsaakde steurings as LSBB. Die hoë-T_c SQUIDs tel ook heelwat $1/f$ ruis op (wat lae-frekwensiemetings beïnvloed); iets wat nie 'n rol speel by die lae-T_c SQUIDs nie. Die groot voordeel van die huidige studie is dat die SQUIDs binne 50 meter vanaf die observatorium vloedhekke geleë is. Ons verwag dus heelwat beter korrelasie tussen SQUID- en vloedhekdata as wat met die vorige studie verkry is, wat dit makliker sal maak om die isolasie te verbeter van seine wat deur die SQUIDs waargeneem is, maar nie deur die vloedhekke nie.

Acknowledgements

I would like to express my sincere gratitude to my supervisor, Prof. Coenrad Fourie, for his excellent guidance, patience and immense knowledge. It was a privilege to work with him; one simply could not wish for a better or friendlier supervisor. Besides my supervisor, I would also like to thank my co-external supervisors at SANSA Space Science in Hermanus, Mr. Danie Gouws and Mrs. Elda Saunderson. Their continuous support, encouragements and insightful comments are extremely appreciated.

I owe my deepest gratitude to the National Astrophysics and Space Science Programme (NASSP) for have introduced me to Space Weather and funded me through out my honours degree and for this study. I also wish to thank Mrs. Nicky Walker for all the support she provided while I was still at the University of Cape Town (UCT). Besides, NASSP, I would like to thank SANSA Space Science for the extra funding they provided for this study and for the South African Institute of Physics (SAIP) conference I attended in July 2013. I am also grateful for a research workshop visit to France in June 2013, which was funded by SANSA Space Science and National Research Foundation (NRF).

I would like to extend my gratitude to the SANSA Space Science management and staff for all the assistance and support they provided. I wish to acknowledge Mr. Emmanual Nahayo for sharing his knowledge and for always providing me with data I requested. Temwani Phiri has also contributed significantly to this study; his knowledge and the materials he provided made this study a lot easier.

I am indebted to many student colleagues at SANSA Space Science, for providing a stimulating and fun environment in which to learn and grow. Electdom Matandirotya was always there for me went I needed help: both academically and socially, for that I am thankful. Thinawanga Tshilande, Nigussie Giday, Netsanet Alamirew, Lifa Mbuli, Kabelo Tsamaisi, Malan Ahoua, Flavien Minko, the rest of my football teammates and all the great people that I met at SANSA, you guys rock.

I wish to thank my girlfriend and a friend, Kamogelo Betty Sethaiso, for all the emotional support, entertainment, care and love she provided through out. Lastly, and most importantly, I wish to thank my parents, Poni Gloria and Olefile David Matladi. They raised me, supported me through out my life, taught me and loved me: for that I'll always be grateful.

Dedications

Dedicated to my son: Reaobaka Botlhale Sethaiso-Matladi.
"We were born to shine"

Contents

List of Figures

List of Tables

Chapter 1

Introduction

Superconducting QUantum Interference Device (SQUID) magnetometers are cryogenic magnetometers that use the combined superconductivity effects of flux quantization and Josephson tunneling to measure relative changes in the applied magnetic field [1]. They are relatively new and highly sensitive magnetometers, that are capable of measuring fields as low as few femto-Tesla. Due to their high sensitivity and low noise levels, they are used for many applications; for instance, they are used for magnetoencephalography (MEG) in medical studies, mineralogical surveys, and geophysical studies [5]. Despite SQUIDs being more sensitive and having low noise levels compared to most conventional magnetometers, correlative studies between SQUIDs and other magnetometers are needed to validate the use for some applications, especially in research studies. In this study we present the correlation between SQUID and Fluxgate magnetometers for geomagnetic storms, with the aim of validating its use for space weather research.

The first Fluxgate magnetometer is said to have been developed in the 1930s. During the Second World War, more sensitive Fluxgate magnetometers were developed for submarine detection [6]. Ever since then Fluxgates have been used in various applications, including geophysical studies or research. In geophysics, 3-axis Fluxgate magnetometers are used world wide by magnetic observatories to monitor variations in the surface geomagnetic field. Monitoring the Earth's surface field forms an important part of geophysics, as it makes it possible to study and predict various geophysical or space weather phenomena. Geophysical phenomena, such as earthquakes and geomagnetic storms, are known to produce geomagnetic perturbations that are observable through geomagnetic data. Moreover, there is significant evidence that electromagnetic signals produced prior to earthquakes can be detected through geomagnetic data obtained by highly sensitive magnetometers like SQUIDs [7, 8]. Since Fluxgates have been used for decades in space weather research and have proved to be reliable, a comparative study of Fluxgate and SQUID data-sets is needed to investigate the reliability of SQUID magnetometers, with regards to space weather research.

This study is based on the correlative study [9], recently performed (in 2012) at the South African National Space Agency (SANSA) Space Science, between SQUID magnetometer and Fluxgate magnetometer data-sets for geomagnetic storms with an objective of validating the use of SQUID magnetometer for space weather research. In that study, SQUID data obtained from the Low Noise Laboratory (LSBB) in France was compared to Fluxgate data sets from three closest observatories to LSBB, namely Chambon la Foret (France), Ebro (Spain) and Fürstenfeldbruck (Germany), all further than 500 km from LSBB. The correlation between SQUID and fluxgate data-sets were found to be, at the very least, 59%. It was concluded that SQUID magnetometers can be used as a valid space weather research instrument. The correlation was based on the comparison of the frequency content of SQUID data with those of the above mentioned observatories closest to LSSB, for geomagnetic storms that occurred in the year 2011.

There are notable distinctions between this study and the previous study [9]. In the previous study, the three-axis SQUID used comprised of three low-T_c devices operated in liquid helium in an underground, low noise environment shielded from most human interferences. The SQUID magnetometer operated at Hermanus for the duration of this study is a high-T_c two-axis device (measuring the z and x components of the geomagnetic field). This SQUID magnetometer operates in liquid nitrogen, and is completely unshielded in the local geomagnetic field of about 26 μT. The environment is magnetically clean to observatory standards, but experiences more human interference than that at LSBB. The high-T_c SQUIDs also experience high 1/f noise at low frequencies which the low-T_c SQUIDs do not suffer from, however, this is compensated for in the high-T_c SQUIDs through ac bias reversal. The big advantage of the current study is that the SQUIDs are located within 50 m from the observatory's Fluxgates. We thus expect far better correlation between SQUID and Fluxgate data than what was obtained in the previous study, which should aid in the isolation of signals detected by the SQUID but not by the Fluxgates.

This document is structured as follows: Chapter 2 will be an introduction to superconductivity, which is essential in understanding the SQUID theory that will be presented is Chapter 3. SQUIDs use superconductive material thus the understanding of basic properties of superconductors is needed for better understanding how SQUID magnetometers operate. Chapter 3 will focus on different magnetometers used for space weather, with more attention paid to SQUID and Fluxgate magnetometers, as they are the subjects of this project. Chapter 4 will deal with space weather, with the aim to describe space weather and the importance of space weather research. Spectral analysis, which are techniques needed for data analysis, will be dealt with in Chapter 5. This will be followed by details about SANSA Space Science SQUID and the data-sets used for this study, in Chapter 6. The last two chapters, Chapter 7 and 8, will respectively focus on data analysis and the conclusion.

Chapter 2

Basics of superconductivity

Superconductivity is an effect in which the electrical resistance of certain materials reduce to zero when those materials are cooled below a certain temperature [10]. All materials exhibiting this phenomenon are termed superconductors, with the temperature at which a superconductor transits from normal conductivity to superconductivity known as the *critical temperature*, T_c or *transition temperature*, as it is sometimes referred to. These critical temperatures, even those of high-T_c superconductors, are extremely low, hence superconductivity is only observed at cryogenic temperatures.

2.1 Discovery of Superconductivity

Prior to 1911, it was already known that the electrical resistance of metals gradually decreases as the temperature of a given metal decreases. Even though this was an experimental fact, no one had observed zero resistance or knew what would happen to electrical resistance at temperatures close to or at absolute zero (0 K). Lord Kelvin postulated that, at absolute zero the flow of electrons in conductors will cease, thus making the electrical resistance infinitely high, since electrons are responsible for conductivity. However, Kamerlingh Onnes and other researchers hypothesized that the electrical resistance will gradually decrease with temperature until reaching zero resistance at absolute zero [11]. At that time, achieving temperatures close to absolute zero was one of the biggest challenges scientist faced. However, liquefaction of gases soon provided the right conditions to perform experiments at cryogenic temperatures.

The first scientist to successfully liquefy gas [12] was Michael Faraday *(1791 - 1867)*, in 1823. He compressed gaseous chlorine until it liquefied (liquid chlorine has a boiling point of 239 K), and he later did the same for almost all the known gases, except for nitrogen, hydrogen, oxygen, nitric-oxide, methane and carbon-monoxide. These gases were considered to be "permanent" gases, i.e., they cannot be liquefied, until Louis Cailletet and Raoul Pictet indepen-

dently liquefied both oxygen and nitrogen, in 1877 [11]. James Dewar [13], then liquefied hydrogen in 1898, leaving helium to be the only natural gas that had not been liquefied. Kamerlingh Onnes [14] *(1835 - 1926)*, in 1908, became the first person to ever liquefy helium. Soon after liquefying helium, which has a boiling point of 4.2 K, Onnes used it to study the electrical properties of metals (mercury wire) at low temperatures [15]. In 1911, Onnes discovered that the electrical resistance of mercury wire abruptly drops to zero at temperatures less than 4.1 K. This phenomenon, where the electrical resistance of some materials becomes zero when cooled below certain temperatures, has since been known as *superconductivity*.

2.2 Basic Properties of Superconductors

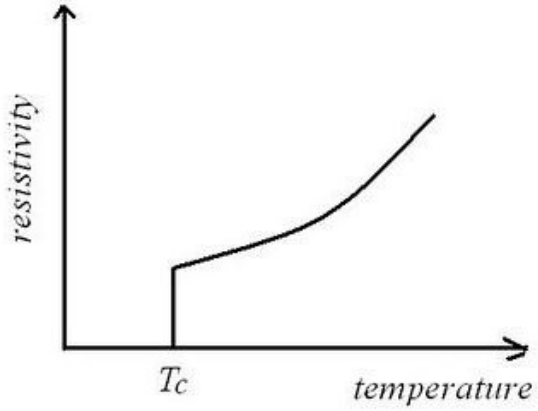

Figure 2.1: Resistance in a superconductive material gradually decreasing with the decrease temperature and abruptly dropping to zero at critical temperature.

A superconductor is any material that is capable of conducting electrical current without any electrical resistance when that material is cooled below a certain temperature, known as the *critical temperature* T_c [16]. Figure 2.1 shows the relationship between the electrical resistance and temperature of a superconductive material. Current in a lead (with $T_c = 7.22K$) ring immersed in a liquid helium bath has been observed to flow in the ring for two and half years without the electrical current diminishing at all times [17, 11], thus proving zero resistance in superconductors when cooled below T_c. Superconductors not only lose their superconductive properties when their temperature is increased above T_c, but also when a large current and/or strong magnetic field are applied to them. The maximum current density and magnetic field

that can be applied to a superconductor without the material losing its superconductive properties, are known as the *critical current density* (J_c) and *critical field* (H_c) [18], respectively. The critical current density and critical field becomes higher as the temperature is decreased below critical temperature. Consequently, superconductors are generally cooled to temperatures less than $0.6T_c$ for engineering applications.

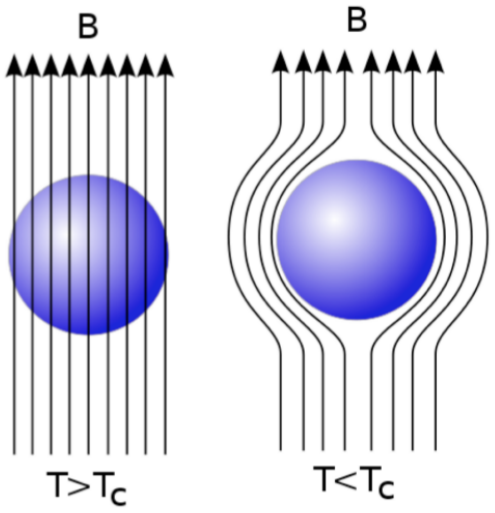

Figure 2.2: Meissner effect: The magnetic field lines penetrate a superconductive material while the temperature of the material is higher than the critical temperature, and are expelled when the temperature is below the critical temperature.

In 1933 it was discovered that if you apply a magnetic field which is less than H_c to the superconductor, the field will be expelled so as to keep $\mathbf{B} = 0$ in the interior of the superconductor [18, 10, 19]. Figure 2.2 shows that when the superconductor is non-superconductive, the field will penetrate the material, but once it is superconductive, i.e. when $T<T_c$, $J<J_c$ and $H<H_c$, the field will be expelled. This phenomenon is known as the *Meissner effect*, and it means that superconductors are perfectly diamagnetic. When a magnetic field is applied to a superconductor, the field induces current inside the superconductor which in turn creates a magnetic field which is equal but opposite to the applied field [20]. Since current flow without resistance in a superconductor, this means that as long as the magnetic field is applied to the superconductor, the induced currents will create an opposing field that expels the applied field indefinitely.

2.3 Models of Superconductivity

Since the discovery of superconductivity, different models have been developed aimed at explaining the underlying physics of superconductivity. The model that best describes how superconductivity occurs, is the BCS theory [21], which deals with the phenomenon of superconductivity at microscopic level. This model was proposed, in 1957, by John **B**ardeen, Leon **C**ooper, and Robert **S**chrieffer and it was subsequently named after them. Although the BCS model is considered to be the most robust, it only works well for conventional superconductors and becomes uncertain for superconductors with critical temperatures above liquid nitrogen temperatures ($77\,K$) [19, 22].

The BCS theory is based on the notion that electrons that carry current in normal conductors pair up in superconductors to form what is known as *Cooper pairs* (also referred to as *superelectrons*). The charge and mass of a superelectron is twice that of an electron, and since these superelectrons have the same momentum and wave vector, they do not undergo any scattering due to collisions with each other [23, 10]. This results in superelectrons carrying lossless supercurrents for a very long time. When energy is applied to a superconductor, such as applying an external magnetic field that is too strong or increasing the temperature above T_c, these superelectrons break up, hence the material loses its superconducting state [19].

The BCS theory fails in explaining the Meissner effect [22], but the classical model of superconductivity does that well as it deals with perfect diamagnetisism as well as zero resistance. These two properties are contained in two equations, known as *London equations* [10], namely,

$$\mathbf{E} = \frac{\partial}{\partial t}(\Lambda \mathbf{J}), \tag{2.1}$$

and

$$\nabla \times (\Lambda \mathbf{J}) = -\mathbf{B}, \tag{2.2}$$

where $\mathbf{E}$ is the electric field, $\mathbf{J}$ is the current density, $\mathbf{B}$ is the magnetic field and Λ is known as the *London coefficient*. The London coefficient is given by

$$\Lambda = \frac{m^\star}{n^\star (q^\star)^2}, \tag{2.3}$$

where $m^\star$, $n^\star$ and $q^\star$ are superelectron mass, superelectron density and superelectron charge, respectively. Equations 2.1 and 2.2, are respectively known as the *first* and *second* London equations. Substituting $\mathbf{J} = (\nabla \times B)/\mu_0)$, into Equation 2.1, then,

$$\mathbf{E} = \frac{\partial}{\partial t}\Big[\Lambda\big(\frac{\nabla \times \mathbf{B}}{\mu_0}\big)\Big] \tag{2.4}$$

$$= \frac{\Lambda}{\mu_0}\Big[\nabla \times \frac{\partial \mathbf{B}}{\partial t}\Big] \tag{2.5}$$

The term Λ/μ_0 has the dimension of unit square length. The square root of this term yields the penetration depth,

$$\lambda = \sqrt{\frac{\Lambda}{\mu_0}} \tag{2.6}$$

The penetration depth of a given superconductor is a measure of how deep an applied magnetic flux can penetrate that superconductor without the loss of superconductivity properties [21].

One of the other useful models of superconductivity is the Macroscopic Quantum Model. The Macroscopic Quantum Model (MQM), not only encompasses the classical model, but it also describes superconductivity as a macroscopic quantum phenomenon [23]. MQM is built on the notion that: macroscopic quantum wave function,

$$\Psi(\mathbf{r}, t) = \sqrt{n^\star(\mathbf{r}, t)}e^{i\theta(\mathbf{r},t)}, \tag{2.7}$$

describes the behaviour of superelectrons in a superconductor [10]. For an isotropic superconductor with a constant $n^\star$, the flow of probability of Ψ is equivalent to the flow of the macroscopic supercurrent, $\mathbf{J}_s$, given by,

$$\mathbf{J}_s = q^\star n^\star(\mathbf{r}, t)\Big(\frac{\hbar}{m^\star}\nabla\theta(\mathbf{r}, t) - \frac{q^\star}{m^\star}\mathbf{A}(\mathbf{r}, t)\Big), \tag{2.8}$$

where $\mathbf{A}$ is the magnetic vector potential and θ is the absolute phase of a wave function. From Equation 2.3, $m^\star = n^\star\Lambda(q^\star)^2$, thus replacing $m^\star$ in Equation 2.8, then

$$\mathbf{J}_s = -\frac{1}{\Lambda}\Big(\mathbf{A}(\mathbf{r}, t) - \frac{\hbar}{q^\star}\nabla\theta(\mathbf{r}, t)\Big). \tag{2.9}$$

Equation 2.9, is known as the *supercurrent equation* and the time derivative of this supercurrent equation yields the first London equation (Equation 2.1). Integrating Equation 2.9, along a closed line C, then

$$\oint_C \Lambda\mathbf{J}_s \cdot d\mathbf{l} + \oint_C \mathbf{A}(\mathbf{r}, t) \cdot d\mathbf{l} = \frac{\hbar}{q^\star}\oint_C \nabla\theta(\mathbf{r}, t) \cdot d\mathbf{l}. \tag{2.10}$$

From Stokes's theorem,

$$\oint_C \mathbf{A} \cdot d\mathbf{l} = \int_S (\nabla \times \mathbf{A}) \cdot ds, \tag{2.11}$$

and the fact that $\mathbf{B} = \nabla \times \mathbf{A}$, Equation 2.10, can be re-written as,

$$\oint_C \Lambda \mathbf{J}_s \cdot d\mathbf{l} + \int_S \mathbf{B} \cdot ds = \frac{\hbar}{q^\star} \oint_C \nabla\theta \cdot d\mathbf{l}. \tag{2.12}$$

In the limit $\oint_C \nabla\theta \cdot d\mathbf{l} = 2\pi n$, where $n = 0, 1, 2, 3, ...$ Equation 2.12 now becomes

$$\oint_C \Lambda \mathbf{J}_s \cdot d\mathbf{l} + \int_S \mathbf{B} \cdot ds = n\Phi_0, \tag{2.13}$$

where Φ_0, is known as *flux quantum* given by

$$\Phi_0 = \frac{2\pi\hbar}{|q^\star|} = \frac{h}{|q^\star|} = \frac{h}{2e} \approx 2.07 \times 10^{-15}\ Wb. \tag{2.14}$$

For $n = 0$, Equation 2.13 yields the second London equation, (Equation 2.2), in integral form. Equation 2.13 states that flux in a superconductor can only be contained in quantized amounts equivalent to Φ_0.

2.4 Type I and Type II Superconductors

Superconductors are classified into two types, *Type I* and *Type II* superconductors [16]. This classification is based on how a given superconductor responds to an applied magnetic field. Type I superconductors are perfectly diamagnetic, with their critical fields, H_c, typically less than 0.1 Tesla [23]. Type II superconductors, on the other hand, have two critical fields; a *lower critical field*, H_{c1} and an *upper critical field*, H_{c2}. When the applied field is less than the lower critical field, $H < H_{c1}$, type II superconductors are perfectly diamagnetic, however, they transform to a *mixed* (or *vortex*) state when the applied field strength is between the lower and upper critical field, $H_{c1} \leq H \leq Hc2$. In the mixed state, the magnetic field will penetrate the superconductor in the form of flux tubes or fluxons, but superconductivity still persists [10, 23, 16].

These flux tubes are non-superconducting and have radii of the London penetration depth, λ [24, 25]. The lower critical fields of type II superconductors are in the same range as type I critical fields, but the upper fields can be hundred times stronger than the critical fields of type I superconductors. This is one of the factors that makes type II superconductors more favourable for use than type I, since type II superconductors can withstand much more intense magnetic fluxes without losing their superconductivity. Some type II superconductors have been observed to have upper critical fields greater than 100 T [16, 24]. Type I superconductors are mostly metals, with critical temperatures typically less than 10 K, where as type II superconductors are mostly alloys and compounds, and can have critical temperatures greater than liquid nitrogen temperatures $(77\,K)$.

2.5 Josephson Junctions

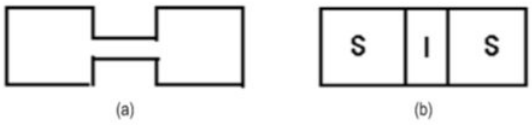

Figure 2.3: (a) A weak link and (b) the SIS junction

A Josephson junction is composed of two superconductors separated by a very thin barrier or a weak link [1], as shown in Figure 2.3. The barrier can either be a thin normal conducting material, forming a SNS junction or an insulating layer forming a SIS junction. In 1962 Brain Josephson [26, 27] postulated that suppercurrents, I_s, can flow from one superconductor to another via a thin barrier or weak link without causing any voltage drop across that barrier or weak link. This phenomenon was soon observed by Phillip Anderson and John Rowell [28], and this is now known as the *Josephson effect*. The supercurrent is defined as

$$I_s = I_c \sin \varphi, \tag{2.15}$$

where I_c is the *critical current*, which is the maximum supercurrent that can pass though a Josephson junction without the junction losing its Josephson effect properties, φ is the *gauge-invariant phase difference* across the junction given by

$$\varphi = \theta_1 - \theta_2 - \frac{2\pi}{\Phi_0} \int_1^2 \mathbf{A}.d\mathbf{l}, \tag{2.16}$$

where $\mathbf{A}$ is the magnetic vector potential and θ represents the phase of the wavefunction of the two superconductors in the junction [10, 23]. Voltage, V, develops across the Josephson junction if the dc current applied to the junction exceeds I_c [1]. Voltage can also develop across the junction if the phase difference changes with time or alternatively the phase difference changes with time when a voltage is applied to the junction. This gives rise to the *voltage-phase relation*, also known as the *second Josephson equation*, given by

$$\frac{d\varphi}{dt} = \frac{2\pi}{\Phi_0} V \tag{2.17}$$

The *dc Josephson effect* is when dc supercurrent flows without a voltage drop and the phases are time independent [26]. An ac current develops across the junction due to time-variation of the phases when a dc voltage is applied to the junction. This is known as the *ac Josephson effect* [29]. This ac current,

also known as *ac Josephson current*, oscillates with a frequency [30, 1], given by

$$f_J = \frac{\omega_J}{2\pi} = \frac{V}{\Phi_0} \approx V \times 483.6 MHz/\mu V. \tag{2.18}$$

Here Φ_0 is taken to be 2.0679 $fT\text{-}m^2$ and ω_J is the angular frequency of the ac Josephson current, which is given by

$$\omega_J = \frac{2\pi V}{\Phi_0}. \tag{2.19}$$

Integrating Equation 2.17, and substituting it in Equation 2.15, gives

$$I_s = I_c \sin\big(\frac{2\pi}{\Phi_0} Vt + \text{constant}\big). \tag{2.20}$$

Equation 2.20, simply means that the current through a Josephson junction oscillates with ω_J when a dc voltage, V, is applied across the junction.

2.5.1 Resistively Capacitively-Shunted Junction Model (RCSJ)

When the current through the Josephson junction, I_s, is less than the critical current, I_c, the voltage drop across the junction becomes zero and the suppercurrents are carried by Cooper pairs. However, for $I_s > I_c$, a voltage drop develops across the junction since now current is carried by normal electrons. The presence of normal electrons give rise to electric resistance and the separation between the superconductors result in capacitance [10]. To solve this resistance and capacitance problem, the RCSJ model is required. The RCSJ model, shown in Figure 2.4, consist of the Josephson element with critical current, I_c, which is parallel to both a capacitor with capacitance, C, and resistor of resistance,R.

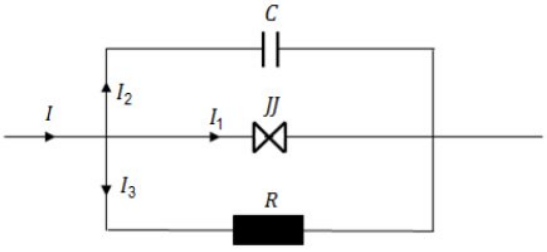

Figure 2.4: RCSJ model

Using Kirchhoff's law, the current through the circuit is

$$I = I_1 + I_2 + I_3 \tag{2.21}$$

$$= I_c \sin\varphi + C\frac{dV}{dt} + \frac{V}{R} \tag{2.22}$$

From Equation 2.17,

$$V = (\Phi_0/2\pi)\frac{d\varphi}{dt}, \tag{2.23}$$

thus

$$\frac{dV}{dt} = (\Phi_0/2\pi)\frac{d^2\varphi}{dt^2}. \tag{2.24}$$

Inserting Equation 2.23 and 2.24, into Equation 2.22, gives

$$I = (\Phi_0 C/2\pi)\frac{d^2\varphi}{dt^2} + (\Phi_0/2\pi R)\frac{d\varphi}{dt} + I_c \sin\varphi. \tag{2.25}$$

Equation 2.25 is a non-linear, second order differential equation, which can be written as a dimensionless equation by letting $\tau = (\Phi_0/2\pi I_c R)$ and dividing both sides by I_c, such as

$$i = \beta_c\frac{d^2\varphi}{dt^2} + \frac{d\varphi}{dt} + \sin\varphi. \tag{2.26}$$

Here, $i = I/I_c$, is the *normalized bias current*, and $\beta_c = (2\pi I_c R^2 C/\Phi_0)$ is the *Stewart-McCumber parameter*. The Stewart-McCumber parameter has two characteristic times, the Josephson time constant

$$\tau_J = \frac{\Phi_0}{2\pi I_c R}, \tag{2.27}$$

and the RC time constant

$$\tau_{RC} = RC. \tag{2.28}$$

Using the Josephson and the RC time constants, the Stewart-McCumber parameter can be written as

$$\beta_c = \frac{\tau_{RC}}{\tau_J}. \tag{2.29}$$

The Stewart-McCumber parameter determines whether the junction is more resistive or more capacitive. In the case of $\beta_c \gg 1$, the parallel combination of the resistor and the capacitor, RC-circuit, exclusively determines the dynamics of the junction . When $\beta_c \ll 1$, the dynamics of the junction are determined by the parallel combination of the basic Josephson junction and the resistor. For this case the RCSJ model is equivalent to the RSJ model used for SQUIDs [23, 10, 1].

2.6 Flux Quantization

Flux quantization was predicted by Fritz London [31, 32, 33] in 1950. He predicted that magnetic flux trapped in a superconducting ring or superconducting tube would be quantized in units of a flux quantum, $\Phi_0 = h/e$. Bascom Deaver and William Fairbank [32], in 1961, observed this phenomenon of flux quantization experimentally, however, they found that the unit at which the flux is quantized is half the value that London had predicted. They found the flux quantum to be, $\Phi_0 = h/2e \approx 2.07 \times 10^{-15}$ Wb. Almost at the same time that Deaver and Fairbank performed their experiment, R. Doll and M Näbaurer [31], also observed flux quantization with flux quantum similar to that of Deaver and Fairbank's experiment.

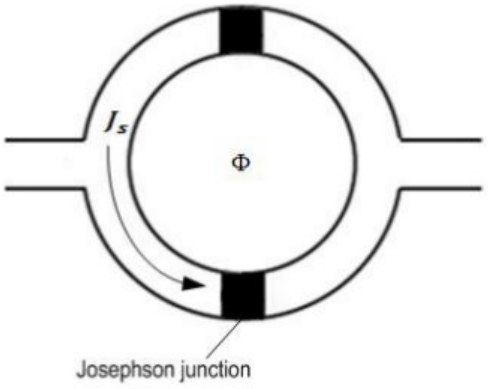

Figure 2.5: Superconducting ring, formed by two Josephson junctions

In a superconducting ring, similar to the one shown in Figure 2.5, the magnetic flux, Φ, passing through that ring is quantized in multiples of a flux quantum, Φ_0 [23]. Since the supercurrent density along the contour is often exponentially small [1], the term $\oint_C \Lambda \mathbf{J}_s \cdot d\mathbf{l}$ from Equation 2.13, becomes zero, thus Equation 2.13 reduces to,

$$\int \mathbf{B} \cdot ds = \Phi = n\Phi_0. \tag{2.30}$$

If a dc current I is applied to the ring, by law of conservation it will separate into I_1 and I_2

$$\begin{aligned} I &= I_1 + I_2 && (2.31)\\ &= I_c \sin\varphi_1 + I_c \sin\varphi_2. && (2.32) \end{aligned}$$

Here I_c is assumed to be the same for both Josephson junctions and φ_1 and φ_2 are phase differences in the respective Josephson junctions. The phase difference in the ring is then

$$\varphi_2 - \varphi_1 = \frac{2\pi}{\Phi_0}\Phi, \tag{2.33}$$

thus

$$\varphi_2 = \frac{2\pi}{\Phi_0}\Phi + \varphi_1. \tag{2.34}$$

Inserting Equation 2.34 into Equation 2.32, then

$$I = I_c\Big[\sin\varphi_1 + \sin\big(\frac{2\pi}{\Phi_0}\Phi + \varphi_1\big)\Big]. \tag{2.35}$$

If $\delta = \varphi_1 + (\pi/\Phi_0)\Phi$, then

$$I = I_c\Big[\sin\big(\delta - \frac{\pi}{\Phi_0}\Phi\big) + \sin\big(\delta + \frac{\pi}{\Phi_0}\Phi\big)\Big], \tag{2.36}$$

which is equivalent to

$$I = 2I_c \sin\delta \cos\left(\frac{\pi}{\Phi_0}\Phi\right). \tag{2.37}$$

Maximum current flows through the circuit when $\sin\delta = \pm 1$, and it is given by

$$I_{max} = 2I_c\left|\cos\left(\frac{\pi}{\Phi_0}\Phi\right)\right|. \tag{2.38}$$

$I_{max} = 2I_c$ is the maximum current that can flow in the parallel configuration Josephson junctions, which is a consequence of $\sin\varphi_1 = \sin\varphi_2 = 1$. When $\Phi = n\Phi_0$, I_{max} value is maximum and its minimum at $\Phi = (n+1/2)\Phi_0$, with $n = 0, \pm 1, \pm 2, ...$ [23]. The applied magnetic field causes the maximum supercurrents flowing in the superconducting ring to oscillate with periods of magnetic flux generated by the magnetic flux quantum. Flux quantization is one of the superconductive properties used in SQUID magnetometers to measure the relative changes in the applied magnetic flux.

2.7 Application of Superconductivity to Magnetometry

Superconductivity can be used to construct magnetometers, which are known as Superconducting QUantum Interference Devices (SQUIDs) [1, 19, 10]. SQUIDs use the concept of flux quantization and Josephson junctions to measure the relative changes of the magnetic field. They are typically formed by two parallel Josephson junctions and they are highly sensitive magnetometers with the

ability to measure magnetic fields as small as few femtotesla. Since SQUIDs use superconductivity technology they require cryogenic cooling, which means their operation is costly and logistically difficult, hence they are not widely used as magnetometers [4].

Chapter 3

Magnetometers

A magnetometer is an instrument essentially used to measure the magnetic flux density. Magnetometers are used by magnetic observatories world-wide to monitor variations in the Earth's magnetic field and for other magnetic observations. There are various types of magnetometers, but this chapter will focus only on two magnetometers and compare them to some of the most common magnetometers. *Fluxgate* and *SQUID* magnetometers will be discussed in this chapter.

3.1 SQUID

Superconducting QUantum Interference Devices (SQUIDs) are relatively new type of magnetometers which use the combined superconductive effects of flux quantization (see Section 2.6) and Josephson tunneling (see Section 2.5) to measure relative changes in the applied magnetic field [1]. They are capable of measuring magnetic fields in the order of femtotesla, thus making them one of the most sensitive magnetometers to date. In this section, we discuss the basic principles of SQUID magnetometer operation and some of their applications.

3.1.1 SQUID principles

SQUIDs are configured as a superconducting ring (which can be of any shape as long as it forms a loop) with one or two Josephson junctions in the loop [1]. SQUIDs with one Josephson junction are known as *rf SQUIDs*, while SQUIDs with two Josephson junctions are *dc SQUIDs*, as pictured in Figure 3.1. As the dc SQUID magnetometer is used for this study, we will discuss its basic principles here. The dc SQUID operation is based on two equations, namely the *first* (Equation 2.15) and *second* (Equation 2.17) Josephson relations. The first Josephson relation comes from the notion that supercurrent, I_s, can flow through a Josephson junction without causing any voltage drop across the

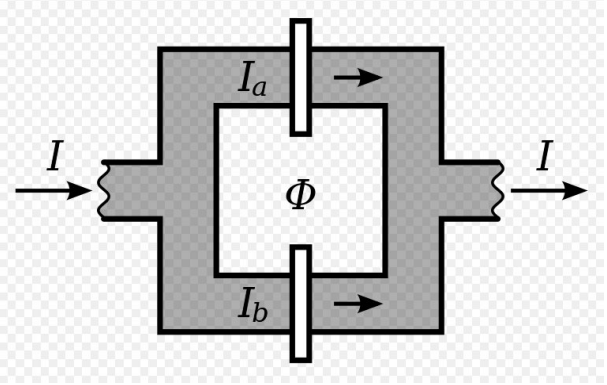

Figure 3.1: dc SQUID

junction [26]. This supercurrent is defined as,

$$I_s = I_c \sin\varphi, \tag{3.1}$$

where I_c is the *critical current*, which is the maximum supercurrent that can pass through the junction without creating any voltage drop across the Josephson junction, φ is the phase difference ($\triangle\ \theta$) of wavefunctions of the superconductors forming the Josephson junction. The dc SQUID ring is biased with constant current which, by using Kirchhoff's current law, is defined as

$$\begin{aligned} I_b &= I_{s1} + I_{s2} \\ &= I_{c1}\sin\varphi_1 + I_{c2}\sin\varphi_2, \end{aligned} \tag{3.2}$$

were I_{s1} and I_{s2} are the supercurrents passing through the respective Josephson junctions in the SQUID ring. This bias current is chosen so that the supercurrents through the Josephson junctions are slightly higher than the junctions' critical currents. According to the second Josephson relation a voltage, V, will develop across the Josephson junctions and this voltage is related to the phase difference as follows,

$$V = \frac{\Phi_0}{2\pi}\frac{d\varphi}{dt}. \tag{3.3}$$

When an external magnetic field, Φ_a, is applied to the SQUID loop, threading the SQUID loop, it will periodically modulate the critical current with a period of one flux quantum, Φ_0. This results in an oscillating voltage with a period of one flux quantum, which looks like a sine wave for $\Phi_a = n\Phi_0$. Using different read-out schemes, the change in this voltage can be output as the corresponding change in the applied magnetic field.

The read-out schemes of SQUIDs essentially linearise the response of the SQUID to the applied magnetic flux and it also plays a major role in the

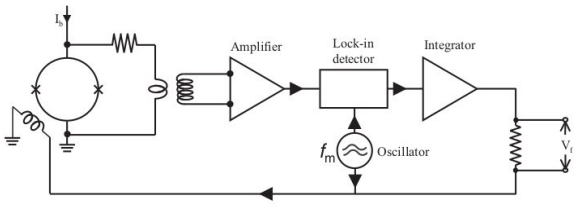

Figure 3.2: Flux modulation and feedback circuit for the dc SQUID: SQUID handbook page 11 [1].

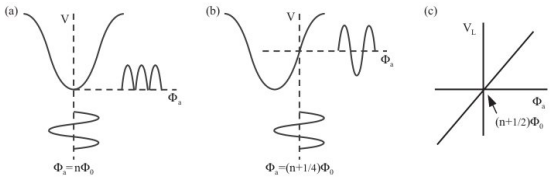

Figure 3.3: Flux modulation scheme showing voltage across the dc SQUID: SQUID handbook page 11 [1].

overall performance of the SQUID magnetometer. A SQUID typically uses a Flux-locked-loop (FLL) read-out scheme [1, 34], shown in Figure 3.2. The FLL circuit consists of an oscillator that modulates the magnetic flux applied to the SQUID ring and also acts as a reference for the lock-in detector. The frequency, f_m, of the applied modulation, typically ranges from 100 kHz to about 10 MHz with peak-to-peak value of $\Phi_0/2$. For $\Phi_a = n\Phi_0$, the voltage output from the SQUID ring that will be fed to the lock-in detector via the amplifier will be a sine wave, as showed on Figure 3.3(a). Using the frequency, f_m, from the oscillator as reference, the lock-in detector's output will be zero as a consequence of this sine shaped voltage. The lock-in detector's output reaches a maximum when the applied flux is $\Phi_a = (n + 1/4)\Phi_0$, Figure 3.3(b). Thus, the lock-in detector's output steadily increases from zero to positive as flux increases from $n\Phi_0$ to $(n+1/4)\Phi_0$, or vice visa as flux decreases from $n\Phi_0$ to $(n - 1/4)\Phi_0$. The lock-in detector's output is then integrated and fed, via a resistor, to the coil that produces modulation to the SQUID loop. When the applied field changes by $\delta\Phi_a$ through the feedback loop, the SQUID will produce an opposing flux, $-\delta\Phi_a$, consequently producing a voltage output across the resistor. This voltage is proportional to the applied magnetic flux and is defined as

$$\delta V = V_\Phi \delta\Phi_a, \tag{3.4}$$

where $V_\Phi = |(\partial V/\partial\Phi_a)_I|$, is the flux-to-voltage transfer coefficient and is a

maximum.

3.1.2 SQUID noise

For low-frequency applications, such as biomagnetism and geophysics, SQUID magnetometers are greatly affected by $1/f$ noise ("flicker noise"), where f is the frequency [5]. There are various sources of $1/f$ noise, however, fluctuations of Josephson junction critical current and motion of vortices are the two significant contributors [1]. Fluctuation of critical currents of the two Josephson junctions in the SQUID ring give rise to voltage and current noise which are both $1/f$ noise. This noise affect both low-T_c and high-T_c SQUIDs, but it is orders of magnitude higher for high-T_c SQUIDs. $1/f$ noise due to critical current fluctuations greatly depend on the quality of the Josephson junction used in the SQUID ring and it can significantly be reduced by reverse bias current feedback schemes, as it is done in the SANSA Space Science SQUIDs. Even though the quality of a superconductive material used to build the SQUID ring plays a significant role in the reduction of $1/f$ noise due to vortices, the ambient magnetic flux can greatly reduce or increase $1/f$, especially the cooling magnetic flux [35]. Cooling magnetic flux refers to the magnetic flux applied to the SQUID system when it is being cooled to a superconducting temperature.

When a SQUID magnetometer is cooled to its superconductive temperatures without being shielded from ambient magnetic flux, flux lines are trapped in the body of the SQUID [1]. As the thermal energy of these vortices gets sufficiently high to overcome the pinning energy of the SQUID ring, the vortices may jump back and forth between two or more adjacent pinning sites, thus giving rise to $1/f$ noise. Since the number of vortices trapped in the SQUID ring is proportional to the cooling field, the cooling of SQUID magnetometers in as low a magnetic field as possible can significantly reduce the $1/f$ noise that arises from these vortices [35]. The other way to reduce the effect of vortices is by improving the pinning of vortices in the SQUID ring. Low-T_c SQUIDs are not affected by $1/f$ noise due to vortices motion as much as high-T_c SQUID are. In fact, $1/f$ noise is not such a significant issue for low-T_c SQUIDs as it is for high-T_c. Using films with sufficiently strong enough flux pinning at helium temperature or above, such as YCBO, acceptable low levels of $1/f$ noise can be achieved in high-T_c SQUIDs [1].

3.1.3 SQUID applications

SQUID magnetometers are capable of measuring frequencies ranging form quasi-DC to a few GHz [34], with sensitivity as low as few femto-Tesla (fT) [36]. SQUIDs are used in variety of fields, notably in medical and geophysical studies. In medical studies, it can be used in a procedure known as *Magne-*

toencephalography (MEG) [37], which measures tiny magnetic fields (ranging from $0.1 - 1$ pT) associated with neutral currents due to brain activities. These measurements are essential in studying brain functions and diagnosing epilepsy, stroke and head trauma. When it comes to geophysical studies, SQUID applications are probably more diverse than in any other field. SQUID magnetometers can be used to measure properties associated with geophysical activities, such as electromagnetic signals associated with seismic activities, geomagnetic activities (geomagnetic storms, for instance), or even from human activities. They also measures things such as the variation in the Earth's magnetic field and gravitational field better than conventional instruments used to monitor these quantities. Commercially SQUIDs are being used, among other things, for mineralogical surveys and for detecting naval vessels and vehicles [5].

3.2 Fluxgate magnetometers

Fluxgate magnetometers measure the absolute strength and direction of magnetic fields. Their sensitivity ranges from 10^{-2} to 10^{7} nT, with bandwidth ranging from quasi-DC frequencies up to about 10 kHz [38].

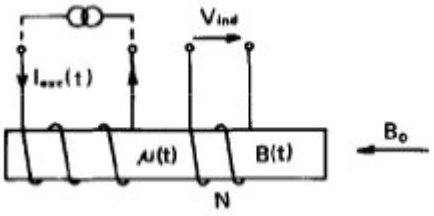

Figure 3.4: The basic configuration of a single-rod core fluxgate magnetometer

3.2.1 Fluxgate principles

Fluxgate sensors typically comprise a ferromagnetic core wound with two coils, the primary (excitation) coil and the pick-up coil [39, 6], as shown in Figure 3.4. Applying a high enough sinusoidal current (excitation current) through the primary coil will cause the core to saturate periodically, resulting in the periodical variation of the permeability of the core, μ_r. The frequency of μ_r is twice the frequency of the excitation current, as it saturates at peak positive as well as negative excitation. As a sinusoidal current is constantly applied and μ_r continuously vary with time, magnetic fields are induced within the core resulting in a voltage developing in the pick-up coil. Moreover, applying

an external magnetic field, $\boldsymbol{B}_{ext}$, parallel to the core, induces a magnetic flux $\boldsymbol{B}_{ind}A$ (where A is the *average cross-sectional area of the core*) inside the core, which modulates the voltage across the pick up coil. The voltage across the pick-coil, which is the output of the fluxgate sensor, is given by Equation 3.5, and is known as the *basic fluxgate equation*,

$$\begin{aligned} V_{ind} &= nA\frac{d\boldsymbol{B}_{ind}}{dt}, \\ &= \frac{nA\boldsymbol{B}_{ext}(1-\boldsymbol{D})}{[1+\boldsymbol{D}(\mu_r-1)]^2}\frac{d\mu_r}{dt}, \end{aligned} \tag{3.5}$$

where n is the number of turns in the pick-up coil and $\boldsymbol{D}$ is demagnetising factor. The voltage across the pick-up coil is a function of the external magnetic field and the time-varying permeability of the core, and it contains the second and higher even harmonics of the excitation current. Typically a *phase sensitive detector* is used to demodulate the voltage output across the pick-up coil to quasi-DC frequencies, yielding a voltage that corresponds to the applied external field [40]. However, there are other schemes that may be used to read out the voltage output of the pick-up coil and there also exist fluxgate sensors with the pick-up coil output as current (short-circuited) instead of voltage.

The fluxgate sensitivity increases with the increase in the excitation frequency, with the excitation typically being between 400 Hz and 100 kHz [40, 6]. Moreover, the sensitivity might be improved by using a core with high permeability and/or by carefully increasing the number of turns, n, in the pick-up coil. The geometry of the core also plays a role on the sensitivity of the fluxgate sensor. Sensors with a basic single-rod core (as in Figure 3.4) are the least sensitive, while sensors with a double-rod core or ring-core are more sensitive and reliable [40]. Fluxgate sensors are either sensitive to magnetic field applied parallel to their excitation field (along the core) or perpendicular to the sensitive axis. The former are know as *parallel types*, while the latter are *orthogonal types*.

3.2.2 Fluxgate applications

The first fluxgate is reported to have been developed in the 1930s, with more sensitive sensors being developed during World War II for detecting submarines [6]. Ever since then, fluxgates have been extensively used in various applications. In geophysics 3-axis fluxgate magnetometers are used world wide by magnetic observatories to monitor variations in the geomagnetic field. Fluxgates are also used for space applications, aircraft and vehicle navigation, reading magnetic marks and labels, and for detection of ferromagnetic objects [40]. For military applications, they are used for detecting submarines, vehicles, bombs, mines and also for missile navigation, among other applications [6, 41].

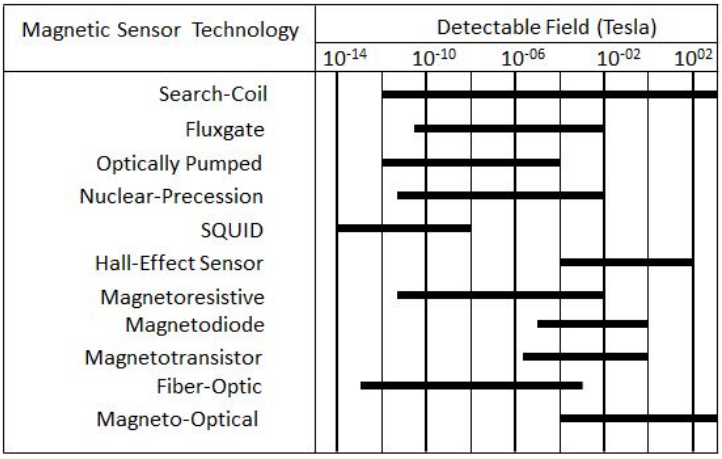

Figure 3.5: Comparison of different magnetometers, adopted from [2].

3.3 Comparison of magnetometers

Sensitivity range and frequency response of a given magnetometer are among the factors that determine which sensor is best suited for a specific application. See Figure 3.5 for approximate sensitivities of the most common magnetometer types. Practically, both the sensitivity range and frequency response of each magnetometer are limited or influenced by the readout electronics [2]. The appropriateness of using a certain magnetic sensor for an application, is also determined by size, power consumption, cost and whether a sensor is a vector or scalar magnetometer, among other considerations. Vector magnetometers measure the vector components of the magnetic field, whereas, scalar or total field magnetometers measure only the magnitude of the field [42]. Vector magnetometers include *search-coil, fluxgate, SQUID, Hall effect sensor, magnetoresistive, magnetotransistor, magnetodiode* and *magneto-optical* magnetometers, while scalar encompasses *optically pumped, nuclear-precession* and *Overhauser* magnetometers. Vector magnetometer provide more information about the measured field than scalar magnetometers. However, their major disadvantage is that they are affected by rotational vibrations which scalar magnetometers are insensitive to. Moreover, nearly all vector magnetometers suffer from noise, especially 1/f noise.

Chapter 4

Space Weather

Space weather is the study of the interaction between the sun-earth system and the effect it has on technology (space and ground based) and on society (human health and lives) [43]. The sun is the prime driver of space weather, thus the understanding and future prediction of its behaviour is key in understanding space weather. Solar activities such as coronal mass ejections, solar flares and dynamic changes of the solar wind are the major factors controlling space weather [44]. Such activities results in physical phenomena, such as geomagnetic storms and Geomagnetic Induced Currents at the earth's surface, which are capable of disrupting some of the ground and space technology systems that our lives have increasingly became dependent on.

4.1 The Sun

The Sun is one of the billions of stars found in our galaxy, *The Milky Way*. It is believed that the Earth and other planets in our solar system, were formed as a consequence of the birth of the Sun. The Sun is estimated to be 4.5 millions years old, with an average distance of 1.496×10^{11} m or, astronomically 1 AU, away from Earth. Like any other star, the Sun is a hot ball of gases which is held together (or stable) by the balance between the force of gravity, pulling the gases inward and pressure from the compressed gases, pushing the gases outward. From observations (solar spectrum), it is now known that the Sun contain all elements (natural) found on Earth and in the periodic table [43]. See Table 4.1, for the five most common elements in the Sun and their relative abundance and Table 4.2, for some interesting properties of the Sun.

4.1.1 Solar Structure

The Sun has three regions, namely the *core*, the *radiation zone* and the *convection zone*. Figure 4.1 shows different layers of the Sun including the solar atmosphere. The core, as the name suggests, is the inner-most layer of the

Table 4.1: The five most common elements in the Sun

Element	Symbol	Relative Abundance
Hydrogen	H	92.1%
Helium	He	7.8%
Oxygen	O	0.061%
Carbon	C	0.030%
Nitrogen	N	0.0084%

Table 4.2: Sun's properties

Age	$\sim$ 4.5 billion years old
Radius	6.69×10^8 m
Mass	1.9×10^{30} kg
Average density	1 410 kg m^{-3}
Average distance from Earth	1.496×10^{11} km (or 1 AU)
Surface temperature	5 800 K
Luminosity	3.86×10^{26} W

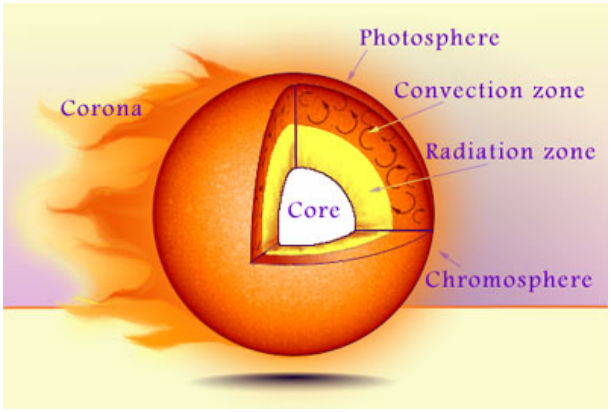

Figure 4.1: Space Weather: Artist impression of the interaction of the Sun and Earth system (courtesy of : solar-heliospheric.engin.umich.edu)

Sun. It is about 200 000 km across, with temperatures of about 1.5×10^7 K. All the energy of the Sun is generated in this region through *thermonuclear* reactions. Thermonuclear is a process were lighter elements fuse together to form heavier elements. Hydrogen is the most abundant element in the Sun and is also responsible for almost all the energy produced by the Sun. Due to the high pressure and high temperatures found in the core, Hydrogen protons, ^1H, collide with each other to form a Deuteron, ^2H,

$$^1H + \ ^1H \rightarrow \ ^2H + e^+ + \nu_e,$$

giving off a positron, e^+ and a neutrino, ν_e. The Deuteron then combines with another Hydrogen proton to form a light Helium,^3H,

$$^2H + \ ^1H \rightarrow \ ^3H + \gamma,$$

where energetic gamma-ray radiation, γ, is the by-product of this reaction. About 86% of the light Helium produced during this reaction, will in turn combine to form heaver Helium elements. At this stage, two light Helium collides, thus producing Helium and two Hydrogen protons,

$$^3H + \ ^3H \rightarrow \ ^4H + \ ^1H + \ ^1H.$$

This process of Hydrogen being converted to Helium, is known as the *proton-proton* chain. Since the produced Helium is 0.7% lighter than the 4 original Hydrogen protons that produced it, according to Einstein's energy formula, this process releases energy, $\triangle E$,

$$\begin{aligned} \triangle E &= \triangle mc^2 \\ &= (4m_H - m_{He})c^2 \\ &= 4.2 \times 10^{-12}\ J. \end{aligned}$$

The Sun radiates this energy away, most of it as visible light. Even though the Sun burns tons of Hydrogen per second, it still has enough Hydrogen to keep burning for about 10^{11} years more [45, 43, 46].

The Sun becomes less dense and cooler as one moves from the core outwards, thus allowing the energy produced in the core to be transported to surface of the Sun, where it will finally be radiated away into space. Energy is transfered in two ways inside the Sun, by radiation and convection. Right above the core lies a region known as the *radiative zone*, where energy is transported by radiation. In this region the plasma is steady and energy is primarily carried by electromagnetic particles (photons) [47]. Above this region to the surface, energy is transfered through convection. This region where energy is carried by packets of plasma (known as convection cells), is called the *convection zone*. The temperature at the bottom of the convection zone is about $1.5 \times 10^6\ K$ and about 5800 K at the surface.

Due to the high temperature at the bottom of the convection zone, the convection cells found at the bottom of the convection zone are hotter, hence less dense (lighter) than the cells above them. This causes the convection cells at the bottom of the convection zone, to raise outward until they reach the surface of the Sun, where the energy they carry is then radiated away. Thus the cells turn cooler and denser, and consequently they become heavier and start to sink back to the bottom of the convection zone. From the surface of the Sun the solar atmosphere starts extending to outer space. The solar

Table 4.3: Average temperatures of different solar regions

Region	Temperature (K)
Core	1.570×10^7
Radiation zone	1.5×10^6
Convection zone	$1.5 \times 10^6 - 5\,800$
Photosphere	$5\,800$
Chromosphere	$6 \times 10^3 - 2 \times 10^4$
Transition zone	$2 \times 10^4 - 2 \times 10^6$
Corona	$2 \times 10^6 - 3 \times 10^6$

atmosphere comprises of the *photosphere*, the visible layer of the Sun, with the *chromosphere* above it and the *corona* being the outer most region of the atmosphere. The zone between the chromosphere and the corona, where the temperature unexpectedly rises, is known as the *transition zone*. It is expected that moving outward from the Sun the temperature will gradually drop, as it does from the surface of the Sun to the chromosphere. Surprisingly, it rises towards the transition zone, thus making the corona the hottest region of the solar atmosphere [46, 43]. It is still unclear as to why the transition zone is so hot. See Table 4.3 for temperatures found in each region of the Sun and its atmosphere.

4.2 Solar Activities

To the naked eye the Sun appears peaceful and calm, but in reality, the Sun is very violent and active. The prime driving force of this violent behaviour of the Sun is thought to be its complicated magnetic field system. Basically, the solar magnetic field is generated and sustained by the rotational movement of the Sun. Since the Sun is made up of gases only and does not have a solid surface, it rotates differentially. The solar equator takes about 25 days to complete one revolution, while the poles takes about 36 days. This differential rotation combined with the movements of the convection cells, twist solar magnetic fields which leads to *sun-spots* being generated on the surface of the Sun.

4.2.1 Sun-spots

Sun-spots appear as dark regions on the surface of the Sun, see Figure 4.2. The darkest and inner-most part of a sun-spot is referred to as the *umbra*, while the surrounding hazy annulus is called the *penumbra*. The dipolar magnetic field of the Sun winds up, like toroidal field, as the Sun undergoes differential rotation. This results in magnetic loops created on the photosphere. As the magnetic loops exit and re-enter the photosphere, they block the energy carried

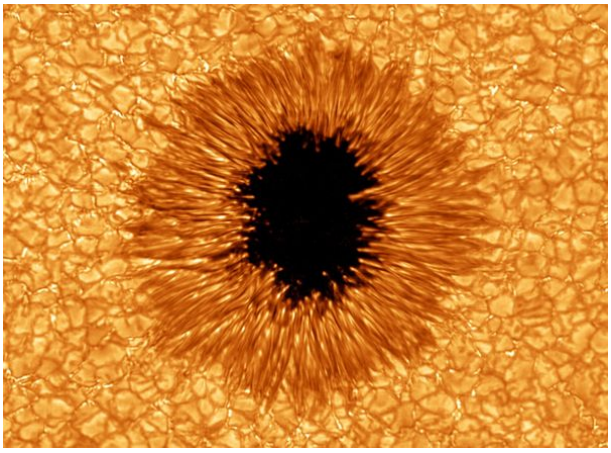

Figure 4.2: An image of a Sun-spot: the inner-most and darkest part of a sunspot is known as the umbra, and it's surrounded by a fuzzier annulus, penumbra (courtesy of: news.nationalgeographic.com)

by convection cells underneath, thus causing that region to be cooler compared to its surroundings [45]. At the centre of a sun-spot (umbra) the magnetic field is vertical, thus blocking more radiation. However, the inclination to the vertical increases as one moves outward, thus blocking less and less radiation [48]. Typically a sun-spot's temperature at the center is 4 000 K, which is about 2 000 K cooler than their surroundings.

Sun-spots can grow up to 6×10^7 m in diameter (approximately 5× Earth diameter), with the smallest typically not greater than 2.7×10^6 m in diameter. Small spots are generally referred to as *pores* and they can only last up to 15 minutes before fading away. In most cases, sun-spots appear for couple of days, but some last for few hours while other may be visible for weeks or even months [45]. Observations have shown that the number of sun-spots on the Sun changes with a period of 11 years resulting in a cycle referred to as the *solar-cycle*. At the beginning of this cycle, sun-spots appear near the solar equator and move towards high latitudes as time passes. In this cycle, *solar minimum* is referred to as time where the number of visible sun-spots are at their lowest. From solar minimum, the number of sun-spots observed gradually increases until they reach maximum, then reduce to solar minimum again. The time were most sun-spots are observed in the cycle is referred to as *solar maximum* [47]. Considering the magnetic polarity reversal of sun-spots, the solar-cycle is said to have a period of 22 years.

4.2.2 Solar flares

Magnetic fields responsible for the appearance of sun-spots are also thought to be the prime source of the phenomenon known as solar flares. Solar flares

produce a burst of electromagnetic radiation from radio waves up to gamma-rays, and also accelerates energetic particles found in the solar atmosphere as well as those escaping into interplanetary space [49]. Solar flares arise from the conversion of the magnetic energy of the sun-spots magnetic fields into thermal energy [50]. Solar flare bursts last from a few minutes to a few hours and their occurrence is generally correlated with the 11 year solar cycle. Small flares correlate well with the solar cycle, but major flares can occur at any time. Solar flares are one of the contributors to Space Weather, with major flares capable of causing radio blackouts on Earth. It takes about 8 minutes for X-ray and UV radiation from solar flares to reach the Earth [51]. Flares produce most of their energy as X-ray radiation, hence they are classified according to their X-ray brightness. Major flares are referred to as X-class flares, with medium-sized flares known as M-class flares, while C-class flares are the smallest [45].

4.2.3 Coronal Mass Ejections

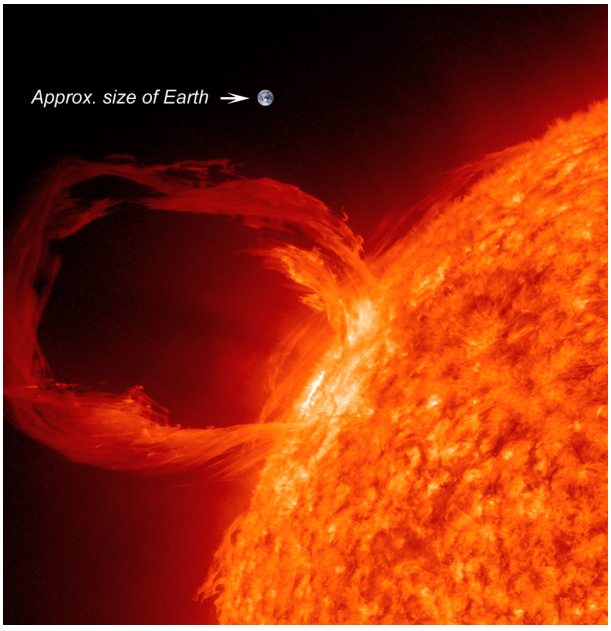

Figure 4.3: CME: coronal mass blown off into interplanetary space. (courtesy of: NASA/SDO)

Coronal Mass Ejections (CMEs) are also associated with the configuration of the solar magnetic field. CMEs result from coronal magnetic fields losing equilibrium or stability, thus releasing large (up to 10^{12} kg) amounts of magnetic coronal matter into interplanetary space, see Figure 4.3. CMEs can reach velocities over 1000 km/s, with high speed CMEs generating shock

waves. These shock waves in turn accelerate energetic particles in front of them [43]. Depending on the velocity of a given CME, it will slow down or accelerate solar winds as it moves through the interplanetary space. In some cases, but not always, CMEs are accompanied by solar flares and/or the eruptions of prominences or filaments. About 40% of solar flares have been observed to occur at the same location as CMEs. The flares occur either before, during or after the CMEs have been blown off the solar corona. Like solar flares, CMEs correlate positively with the 11 years solar cycle, with CMEs largely being observed around the solar equatorial region at solar minimum and at every latitude at solar maximum. CMEs take about 4 days to reach Earth, and they are the major cause of magnetic storms. Major CMEs may produce intense auroras, cause electrical power blackouts or even destroy satellites [45].

4.2.4 Solar Wind and Interplanetary Magnetic Field

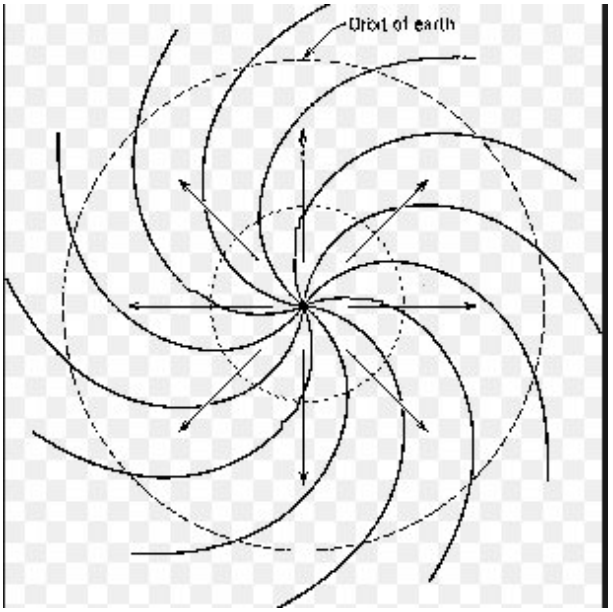

Figure 4.4: Schematic diagram, illustrating the spiral configuration of the IMF

Through observations, it has been long known that there exists a continuous radial flow of plasma from the Sun into interplanetary space. This plasma is a mixture of ions and electrons [44], and it is known as the *solar wind*. Due to the high electrical conductivity of the solar wind, some of the Sun's magnetic fields are frozen into the plasma and stretched into interplanetary space as the solar wind radially stream off the Sun [52]. These magnetic solar winds give rise to what is known as the *Interplanetary Magnetic Field* (IMF). Interplanetary Magnetic Field lines stretch from the Sun into interplanetary

Table 4.4: The average properties of the solar wind and IMF at the Earth's orbit.

Number density	5 particles cm^{-3}
Temperature	1×10^6 K
Velocity	400 $km\,s^{-1}$
Composition	90% H, 8% He, and other heavy ions
IMF	10 nT

space in a spiral form, see Figure 4.4. The spiral configuration, sometimes referred to as Archimedes spirals, is a consequence of the combined effects of the solar rotational motion and the radial flow of solar winds. As one move away from the Sun, the spirals becomes more apparent. The degree at which the spirals are twisted is largely determined by the speed of the solar wind, as opposed to the Sun's rotation [45].

Solar winds follow two patterns; slow and fast. Slow solar winds travel at velocities less than 450 km/s, whereas, fast solar winds can reach speeds of up to 800 km/s. Slow solar winds cause the interplanetary magnetic field lines to spiral more, while fast solar winds make them less spiral. The IMF plays an important role in Space Weather, as it interferes with the directions of material and radiation blown by the Sun into interplanetary space. Energetic particles and plasma from the Sun follows the IMF due to their electromagnetic properties. Thus, if these materials are traveling along IMF lines that intersects Earth's orbit, the materials will interact with the Earth [43, 46]. The IMF strength is known to be in the order of nanotesla at the Earth's orbit. Table 4.4 shows the average properties of the solar wind and IMF at the Earth's orbit. The orientation of the IMF also plays a major role in generating geomagnetic activities such as geomagnetic storms. Southward, $-\boldsymbol{B}_z$, directed IMF causes magnetic reconnection between the IMF and geomagnetic field, resulting in a significant transfer of energy, momentum and mass from solar wind into the Earth's magnetic field.

4.3 Magnetosphere

The Earth's magnetosphere is formed as a result of the Earth's magnetic field interacting with the magnetized solar winds (IMF) [53]. Figure 4.5 shows the geomagnetic field interacting with the solar wind and the structure of the magnetosphere. In the absence of the solar wind, the Earth's magnetic field would look more or less like a perfect dipole magnetic field. In reality, the solar winds compresses the Earth's magnetic field lines from the day side of the Earth (the side facing the Sun) and stretch them into outer space on the Earth's night side, thus deforming the dipole configuration of the Earth's

magnetic field. The deformed (non-dipolar) part is generally referred to as the *outer magnetosphere*, while the part of the geomagnetic field that still retains the dipole (on average) configuration is known as the *inner magnetosphere*.

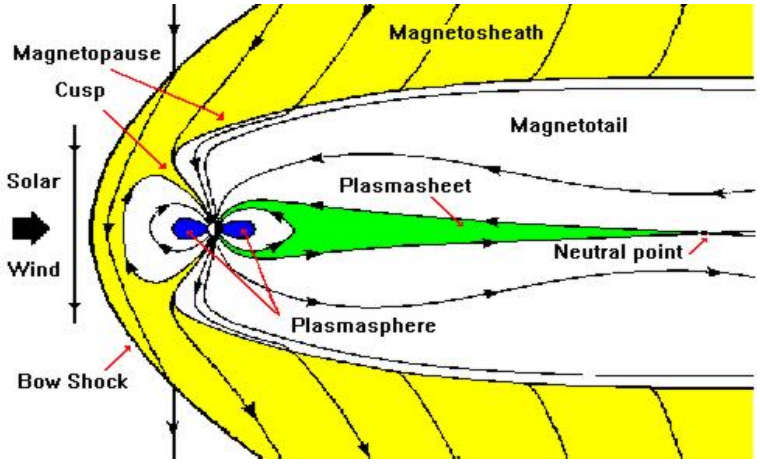

Figure 4.5: Schematic of the Magnetosphere: courtesy of helios.gsfc.nasa.gov

4.3.1 Structure of the Magnetosphere

The solar wind flows at very high velocities (almost supersonic), thus generating a shock wave as it collides with the magnetosphere. This shock is known as a *bow shock* and it is formed just above the magnetosheath, as seen from Figure 4.5. The bow shock deflects the solar wind around the magnetosphere while slowing down the solar wind in the process. The boundary between the solar wind and the magnetosphere is known as the *magnetopause*. This boundary can be as far as 10 Earth radii (R_E) from Earth, but it always moves back and forth as the dynamics of the solar wind vary. When the magnetic field of the solar wind (IMF) and the geomagnetic field are in opposite directions, *reconnection* of the solar wind and geomagnetic field lines take place. This results in open fields, with one end attached to Earth and the other to the solar wind. As the solar wind is swept behind the Earth (night side), it drags the magnetic field (open fields) along. At the night side of Earth, the open field lines reconnect to form a long tear-drop like shaped closed magnetic field lines known as *magnetotail* [43, 54].

The magnetotail is roughly 30 R_E across and extends beyond 1,500 R_E [3]. The magnetotail consists of two magnetic lobe regions; one fixed at the north polar cap with the other at the south polar cap. These two lobes are separated by a region known as the *plasma sheet*, which have higher plasma density than the lobes. Since the lobes contains open magnetic field lines, plasma can stream along the magnetic field lines into outer space thus making

the lobes less plasma dense than the plasma-sheet. The magnetotail lobes have opposite orientations; the north lobe points Earth-ward while the south lobe points away. At around $\pm 78^{\circ}$ magnetic latitude lies a region known as *polar cusps*. This a region where the magnetopause field lines are connected to the Earth's surface, thus making it possible for solar wind particles to enter the magnetosphere without crossing the field lines [3, 43].

The inner magnetosphere is characterized by closed magnetic field lines, i.e., field lines with both ends connected to the Earth's surface. Due to the closed field lines found in the inner magnetosphere, plasma and particles are trapped in field lines, thus forming regions such as the *plasmasphere* and *radiation belts* (Van Allen Belts). The plasmasphere consists of cold and dense plasmas that originate in the topside of the ionosphere [55]. Typically the plasmasphere is found between 3 and 6 R_E, but for geomagnetically active periods it can be as close as 2 R_E. The plasmasphere has high particle density compared to the radiation belts with particle energies of several electron volts. Radiation belts consist of high energetic particles ($>$ 100 keV), with the *inner* belt found between 1.2 - 2.5 R_E and the *outer* belt between 3 - 10 R_E. The outer belt is most intense between 4 and 5 R_E and is dominated by electrons, whereas the inner belt is dominated by protons [56]. The particle flux between the inner and outer radiation belts is small and this region is often refer to as the *slot*.

4.3.2 Particles in the dipole geomagnetic field

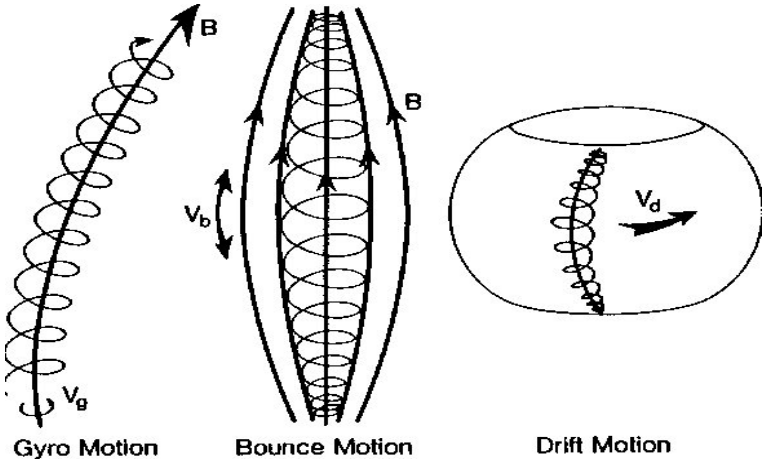

Figure 4.6: Three types of motion that a moving particle undergo as it interacts with the dipole geomagnetic field lines. (www-ssc.igpp.ucla.edu)

The plasma-sheet, Van Allen belts and the plasmasphere are formed by energetic particles trapped by geomagnetic field lines (closed loops). As moving electric particles interact with the dipole-like, static geomagnetic field they

gyrate around field lines, *bounce* back and forth between the northern and southern hemisphere and also *drift longitudinal*, as shown in Figure 4.6. This results in these particles being trapped along the field lines. Suppose a charged particle of mass m and charge e in the magnetosphere, have velocity $v_\perp$ perpendicular to the magnetic field and $v_{||}$ parallel to the field. Then the particle will gyrate in a spiral motion with the gyration radius of

$$r_B = \frac{mv}{\mathbf{B}e}, \tag{4.1}$$

where v is the total velocity of the particle and $\boldsymbol{B}$ is the magnetic flux the particle is gyrating on. The magnetic moment, μ, associated with the particle and its motion is invariant (i.e. if no work is done on or by the particle) and is given by

$$\mu = \frac{ev_\perp}{2\pi r_B} = \frac{mv_\perp}{2\mathbf{B}} = \frac{E_\perp}{\mathbf{B}} = \text{constant}, \tag{4.2}$$

where $E_\perp$ is the kinetic energy related to the transverse component of velocity $v_\perp$. If v is the total velocity of the particle, the

$$v_\perp = v \sin\alpha, \tag{4.3}$$

where α is the pitch angle, the angle between the velocity component and the magnetic field. Since there are no acceleration mechanisms acting on the particle, its total kinetic energy, E, is constant,

$$\frac{E_\perp}{\mathbf{B}} = E \sin^2\alpha\mathbf{B} = \text{constant}. \tag{4.4}$$

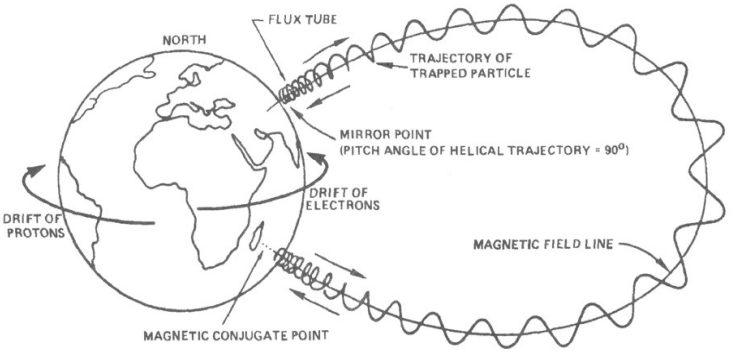

Figure 4.7: Motion of a charged particle in the magnetosphere. (astronautic-snow.com)

Thus $\sin^2\alpha \propto \mathbf{B}$. Hence, when the particle moves from the equator, where the magnetic field is weaker, to higher or lower latitudes, its pitch angle increases as a consequence of increasing $\boldsymbol{B}$. When the pitch angle, $\alpha = 90°$,

the particle stops and is reflected back to the equator. The point of reflection is referred to as the "*mirror point*". However, if the particle encounters the atmosphere before it reaches the mirror point it will be lost. Electrons have shorter *bounce times* compared to protons. Bounce time is the time needed for a particle to travel between mirror points. Figure 4.7 illustrates particle motions in the dipole geomagnetic field. Additional to the gyration and bouncing motion, the particles also drift longitudinal. The longitudinal drift is due to the curvature of field lines which produce a centrifugal force to which a particle responds by drifting. Moreover, as the particle gyrates in a slightly weaker field, its radius of gyration changes resulting in the shift in the orbit. The combination of these two effects is known as *gradient-curvature* drift and it is given by

$$v_{GC} = \frac{m}{e\mathbf{B}^2} \cdot \frac{\partial \mathbf{B}}{\partial \mathbf{R}} \cdot (\frac{1}{2}v_{\perp}^2 + v_{||}), \tag{4.5}$$

where $\mathbf{R}$ is the radial geocentric distance. For a particle with velocity v and pitch angle, α, $v_{||} = v\cos\alpha$ and $v_{\perp} = v\sin\alpha$, then

$$v_{GC} = \frac{1}{2}\frac{mv^2}{e\mathbf{B}^2} \cdot \frac{\partial \mathbf{B}}{\partial \mathbf{R}} \cdot (1 + \cos^2\alpha) \tag{4.6}$$

The gradient-curvature drift cause the electrons to drift east and protons to the west, as seen on Figure 4.7. This eastward drift of electrons and westward drift of protons result in a current flowing from the east to the west, known as the *ring current*. As the ring current increases, as is the case during magnetic storms (see Section 4.6.1), the Earth's surface magnetic field strength diminishes [3, 57].

4.4 Ionosphere

The *ionosphere* is a region of weakly ionized atmospheric gases, located about 50 km above the Earth's surface, and extends to magnetospheric regions. The term was coined in 1926 by R. Watson-Watt, but it only became popular about 1932 [3]. The ionosphere is formed when the high-energy solar rays (mostly UV and X-rays) ionize the upper atmosphere gases (such as N_2, O_2 and O) in a process known a *photo-ionization*. The intensity of the ionizing radiation decreases with decreasing altitude, which results in the rate of photo-ionization varying with altitude. As a consequence of the varying photo-ionization rate with altitude, the electron density within the ionosphere also varies with altitude, and this variation is used to divide the ionosphere into layers (characterised by their peak electron density). Figure 4.8 and Table 4.5 show the typical electron densities of different layers and their typical locations. The main layers of the ionosphere are the D, E, F_1 and F_2 layers. The D-layer ranges from about 50 - 90 km above the Earth's surface, with the E-layer starting just above it at around 100 km. The F_1 layer is from about

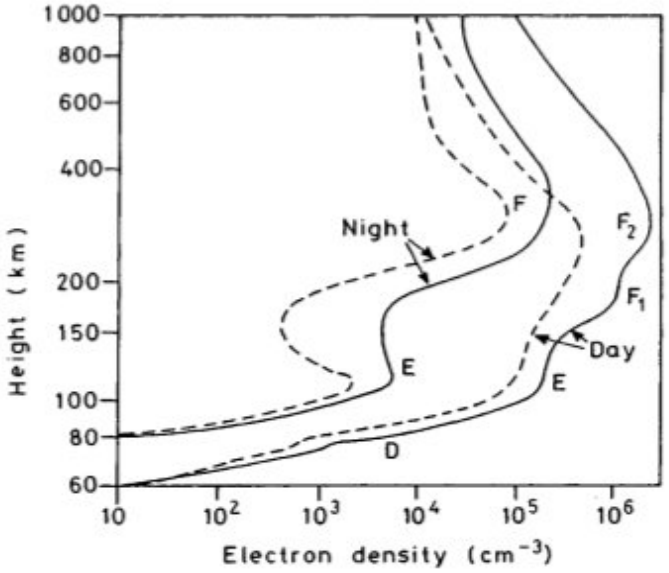

Figure 4.8: Typical profiles of electron density of the ionosphere. Solid lines show how electron density changes with height during solar maximum, while dashed lines show the change during solar minimum [3].

Table 4.5: Ionosphere layers with their typical electron densities

Layer	Location (From Earth's surface) [km]	Electron density [cm^{-3}]
D	50 – 90	$10^2 - 10^4$
E	100 – 150	several 10^5
F_1	150 – 200	several $10^5 - 10^6$
F_2	Maximum around 300 km	up to several 10^6

150 to 200 km, and above it is the F_2 layer, which extents to magnetospheric regions [3, 43].

The rate of change of the electron density is generally given by the *continuity equation*,

$$\frac{\partial N}{\partial t} = q - L - \text{div}(Nv), \tag{4.7}$$

where q is the production rate (photo-ionisation rate), L is the loss rate by recombination while div(Nv) expresses the loss of electrons by movement, with v being their drift velocity. Photo-ionisation begins when the sun rises, then the photo-ionisation rate gradually increases as the Sun makes its way to the highest point in the sky (local mid day), when photo-ionisation is maximum. Moreover, the rate of photo-ionisation gradually decreases as the Sun makes

its way to setting. This results in the electron density reaching its maximum around local noon. The process of electron loss via recombination (mostly) and electron movement never stops. Thus at night, when photo-ionisation has stopped, electron density decreases. However, the rate of electron loss due to both these effects is slow, hence some of the ionosphere layers persist through out the night. At night the D and F_1 layers disappear, leaving only the E and F layers, see Figure 4.8. The photo-ionisation is primarily due to solar radiation, however, energetic particles from the magnetosphere also play a part [43, 3, 58].

4.5 Geomagnetic components

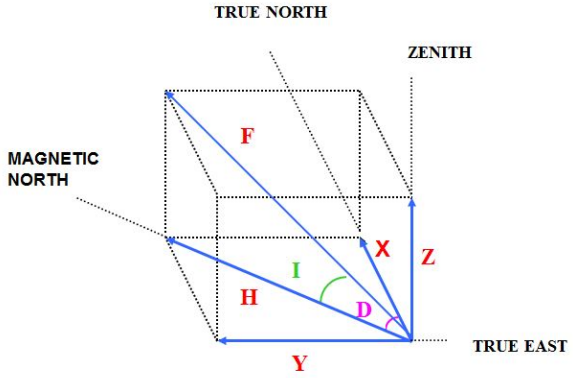

Figure 4.9: The Sourthern Hemisphere geomagnetic components.

The Earth's magnetic field is monitored worldwide by ground-based magnetic observatories using magnetometers, which measure variations (over time) of the magnetic field components on the Earth's surface. The Earth's magnetic field can, by international agreement, be represented by vectors as shown on Figure 4.9. The X-component represents the magnetic vector from geographical south to north, while the Y-component is the magnetic vector from geographical west to east and the magnetic vector that points vertically down to Earth (earthwards), is the Z-component (negative values for the opposite directions). The X, Y, and Z components are orthogonal; combined they form the geomagnetic field representation known as XYZ component representation. The geomagnetic field lines exit the Earth's surface close to the geographic south pole and enters close to the geographic north pole. This means that, in the southern hemisphere, the geomagnetic field lines are at an angle pointing vertically upwards, while in the northern hemisphere they are pointing in the

opposite direction (at an angle pointing vertically downwards). Thus the Z-component is measured as negative in the southern hemisphere and positive in the northern hemisphere.

Another representation is the combination of the H, D and Z components, called the HDZ component representation. Here the H-component represents a magnetic vector which is horizontal to Earth and points towards magnetic north, while the D-component, known as declination, is the angle between the H-component and the X-component. Mathematically it can be shown that,

$$X = H\cos(D) \quad \text{and} \quad Y = H\sin(D). \tag{4.8}$$

The total geomagnetic field strength is represented by the F-component, and is mathematically given by,

$$F = \sqrt{X^2 + Y^2 + Z^2} = \sqrt{H^2 + Z^2},$$

since,

$$H = \sqrt{X^2 + Y^2}.$$

From the F-component the inclination, I-component, which is the angle that the F-component makes with the horizontal plane, can be found from,

$$\tan(I) = \frac{Z}{H}.$$

The inclination is most useful in determining the geomagnetic dipole equation, as the geomagnetic equator is defined by a line along Earth's surface for which the inclination is zero, i.e. $I = 0$ [59].

4.6 Solar wind - Magnetosphere - Ionosphere coupling

There are various mechanisms responsible for coupling between the solar wind and the magnetosphere, but *reconnection* is thought to play a major role in energy transfer between these two systems [60]. When the interplanetary magnetic field (IMF) is oriented southward, the IMF reconnect with the geomagnetic field lines, allowing a significant amount of plasma from the solar wind to enter the magnetosphere. The longer the interplanetary magnetic field lines remain oriented southward, the more energy will be transfered to the magnetosphere. Moreover, since the magnetic field lines forming the magnetosphere thread the ionosphere, the energy will be further transfered to the ionosphere. The solar wind - magnetosphere - ionosphere coupling is still not well understood, but variations in the solar wind have been observed to be a driver of various magnetospheric processes such as geomagnetic storms and ionospheric processes such as auroras at high latitudes [54].

4.6.1 Storms

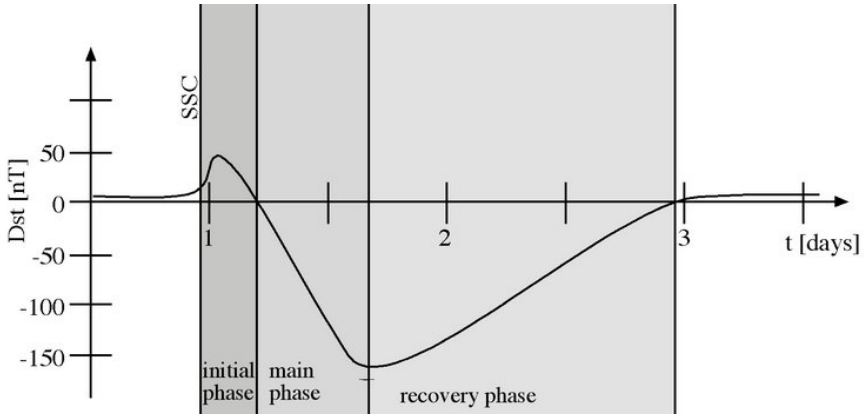

Figure 4.10: Dst - Variation of the geomagnetic surface field measured at mid-latitude observatories; pre-, during and post- geomagnetic storm.

Geomagnetic storms are characterized by a sudden drop of the geomagnetic surface field (H - component). Their intensities and duration are generally classified using the *Disturbed Storm Time Index* (Dst), which is associated with the ring current [3]. The Dst is computed using measurements of the geomagnetic surface field observed at middle and low latitude geomagnetic observatories. Geomagnetic storms generally last for a couple of days. They typically have three phases, the initial phase (often referred to as *sudden storm commencement* - SSC), the main phase and the recovery phase [61, 43], see Figure 4.10.

Geomagnetic storms are primarily due to high speed solar winds with south-ward IMF, caused by solar activities such as CMEs, solar flares or coronal holes. As the high speed solar winds interact with the magnetosphere they compress it, as a consequence the geomagnetic surface field strength increases. This results in the Dst value increasing, as seen in the Figure 4.10, and marks the initial phase of the storm. The initial phase only last for tens of minutes to hours before the Dst drops abruptly. The south-ward oriented IMF causes reconnection between the IMF and magnetosphere, causing large amounts of high energetic particles to be deposited into the magnetosphere. The increase of high energetic particles inside the magnetosphere enhances the ring current which in turn reduces the geomagnetic surface field.

The decrease of the geomagnetic surface field is reflected by the sudden drop in the Dst index value. This is the main phase of the storm. This phase, where the Dst index value decreases to negative values, can last for a couple of hours and ends when the Dst index value reaches its minimum. This is subsequently followed by the recovery phase, where the Dst index value

Table 4.6: Classification of Geomagnetic storms.

Storm strength	K_p	Dst[nT]
Minor	4,5	> -50
Moderate	6	$-50 > Dst > -100$
Intense	7-9	< -100

gradually increases to its normal quiet time value. The recovery phase usually takes days. During geomagnetic quiet times, the Dst ≈ 0 (± 20) nT, whereas during a storm it can be as low as -100 nT [62]. Another widely used index to measure the intensity of a geomagnetic storm is the K_p index. The K_p is a measure of the overall variability of the geomagnetic field at mid-latitude, taken in 3 hour intervals. Table 4.6 shows the classification of storms using the K_p index and the Dst index. The K_p index ranges from 0 to 9, with 0 representing geomagnetic quiet and 9 being the most active [63]. Geomagnetic storms can cause major damage or disruptions in some technological systems, both ground and space based.

4.6.2 Sub-storms

The other magnetic disturbance associated with southward IMF is the magnetospheric *substorm*. Substorms are very small and occur more frequently than geomagnetic storms. Storms occur on rare occasions and can last for days, while substorms happen a couple of times per day and only last for an hour or so. Moreover, the storms affect the magnetosphere globally, whereas, substorm effects are generally more localized on the nightside of Earth [43]. Storms are known to be due to the increase in ring current but substorms are often accompanied by loss of energy from the ring current [57], which is surprising as storms are associated with substorms (but not always). Substorms have been observed to occur most frequently when the IMF is oriented southward. However, there are cases where substorms are triggered by the IMF as it turns back northward after been oriented southward [3].

Southward IMF results in the IMF and geomagnetic field reconnecting, and as a consequence, the solar energy (plasma) is deposited into the magnetosphere. This energy is then transferred to the nightside of Earth, and returned back to the dayside as open lines reconnect in the nightside. If more energy is transferred to the nightside than returned to the dayside, energy will build up and be stored as magnetic energy at the nightside. Substorms will thus be triggered as this energy is released explosively [54], in a timescale that is much shorter than it took for the energy to be stored. Substorms are associated with magnetic waves referred to as Pi2, auroral displays, and intense ionospheric currents. They may also enhance energetic particles at radiation belts.

4.7 Geomagnetic pulsations

Geomagnetic pulsations are ultra-low-frequency (ULF) waves with frequencies ranging from approximately 1 mHz to more than 10 Hz. Depending on their waveform, they are classified in two types, the Pulsation *irregular* (Pi), which have irregular waveforms and Pulsation *continuous* (Pc), which comprises of quasi-sinusoidal waveforms. These types are further subdivided in a range of frequencies as shown in Table 4.7 [64]. Geomagnetic pulsations are produced by various mechanisms, both locally (Earth's surface, ionosphere and within the magnetosphere) and outside the magnetosphere.

Table 4.7: Classification of Geomagnetic pulsations.

Type	Period range(sec)	Frequency range(Hz)
Pc1	$0.2 - 5$	$0.2 - 5$
Pc2	$5 - 10$	$0.2 - 0.1$
Pc3	$10 - 45$	$0.1 - 0.02$
Pc4	$45 - 150$	$0.02 - 0.0067$
Pc5	$150 - 600$	$0.0067 - 0.00167$
Pi1	$1 - 40$	$1 - 0.025$
Pi2	$40 - 150$	$0.025 - 0.0067$

4.7.1 Alfvén model for wave generation

The Alfvén model considers an infinite volume of a fully ionized plasma with magnetic flux "frozen into" the plasma. Magnetic fields frozen in plasma move as charges in the plasma are displaced by any force and vice versa. The force applied orthogonal to the magnetic field flux density, $\mathbf{B}$, to move a rectangular section of plasma with velocity, $\mathbf{v}$, as shown in Figure 4.11(a), causes polarization of charges within the slab due to the Lorentz force,

$$\mathbf{F} = q(\mathbf{v} \times \mathbf{B}), \tag{4.9}$$

where q is charge in Coulombs. The Lorentz force will cause the electrons to drift to the left-side of the slab and protons to the right, as in Figure 4.11(b), creating an electric field $\mathbf{E}$ perpendicular to both $\mathbf{v}$ and $\mathbf{B}$. Since the slab of plasma is surrounded by plasma, charges can flow through the surrounding fluids in an attempt to neutralize the polarization. The motion of these charges results in current flowing across the magnetic field above and below the moving slab. This current exerts a force,

$$\mathbf{F} = \mathbf{J} \times \mathbf{B}, \tag{4.10}$$

on the plasma with the same direction as **v** (same direction as motion of the initial slab), where **J** is the current density, see Figure 4.11c. The plasma above and below begins to move. The same analogy can be applied to these two moving slabs. In Figure 4.11(d), they become polarized driving currents that cause the slabs farther below and above the initial moving slab to start moving. As the slab moves, it distorts the magnetic field that is frozen into plasma as shown in Figure 4.11(e). Moreover, tension develops as the field is distorted, creating a restoring force that eventually stops the slab and moves it towards its initial location. The moving slabs above and below the initial slab distort the magnetic line in the same way, Figure 4.11(f), thus the two pulses appear to propagate away from the origin. These pulses are known as Alfvén waves [64].

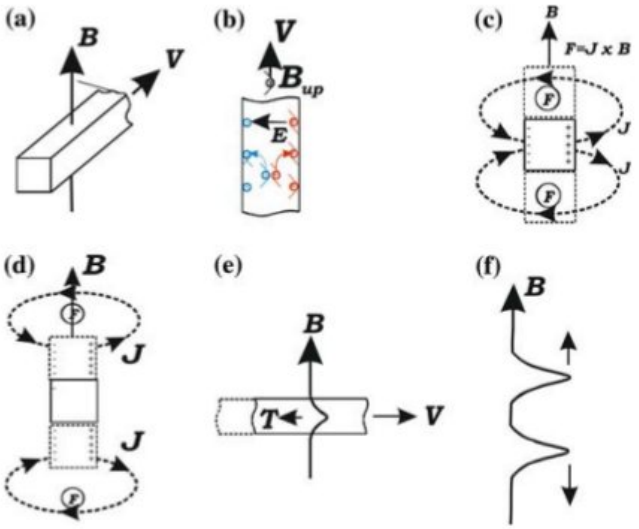

Figure 4.11: Alfvén model for wave generation

4.7.2 Sources of geomagnetic pulsations

Many of the geomagnetic pulsations are thought to originate from the Sun through various solar activities, such as solar flares. They are then both carried by and propagated through the solar wind, which transfers them past the magnetopause as the solar wind interacts with the magnetopause. Once inside the magnetosphere, they interact with waveguides, cavities and magnetic field lines, producing pulsations that are observable through magnetic data measured at the Earth's surface, ionosphere and also within the magnetosphere. Some pulsations are due to the variations in the dynamic pressure of the solar wind, as it causes the magnetosphere to oscillate. Multiple peaks at frequencies, including 0.4, 0.7, 1.0 and 1.3 mHz, have been associated with

the oscillations of the magnetosphere due to variations in the dynamic pressure of the solar wind. Although some frequency peaks are associated with certain phenomena, it is always a tough task to associate frequency peak(s) to one specific phenomenon. One peak or range of peaks can be due to difference sources. The magnetopause also generates ULF waves, with frequency peaks around 1.3, 1.9, 2.7, 3.1 and 4.1 mHz having high probability to occur. Substorms are thought to produce Pi2 waves, while geomagnetic storms are not related to any specific frequencies. ULF waves are also generated by geophysical activities such as earthquakes, lighting and variations in the motion of Earth's molten core [64].

4.8 Space Weather Effects

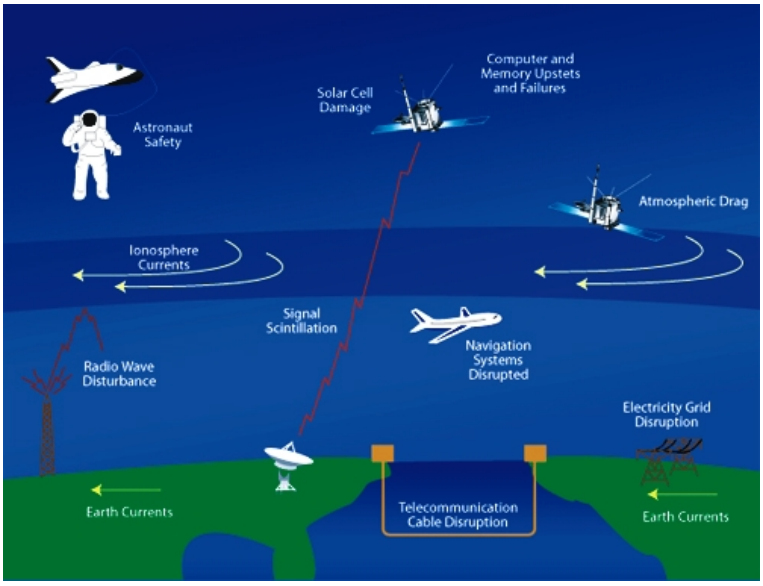

Figure 4.12: Different systems affected by space weather effects: courtesy of http://stix.i4ds.ch/public-outreach/space-weather-overview/

Solar activities, such as solar flares and CMEs, are the prime drivers of space weather events. Geomagnetic disturbances due to such solar activities can disrupt or even destroy some of our ground and space based technological systems. Figure 4.12 shows a list of systems susceptible to space weather events. Satellites, electrical power systems, telecommunication systems and pipe lines are among the systems that can be severely affected by space weather events. Satellites are used in everyday life for different purposes such as communication, Earth-observations, for weather and Global Position System (GPS), while electricity is a necessity for almost everything we do daily.

A power outage for a short period of time, even an hour, in major cities can result in major loss of revenue or car accidents, since traffic is controlled by systems powered by electricity. Not only does Space Weather events pose a threat to technological systems, but also on human lives. Increased radiation levels during Space Weather events can endanger lives of astronauts in space and might also cause health problems for passengers and crew in aircraft at high latitudes [44, 43]. Since Space Weather events pose a threat to most of the technological systems our lives are so much dependent on, the prediction of these events is of extreme importance from both the scientific and societal perspective.

Chapter 5

Spectral Analysis

Signals are generally represented in the *time-domain*. Unfortunately all the information that is contained in a signal is not always visible in the time-domain. In geophysics, our desire is to extract frequency components and their amplitudes that are encoded in any given signal. Using Fourier transforms, a time-domain signal can be transformed into a *frequency-domain* signal, thus revealing the hidden frequency components and their amplitudes. The graphical representation of a signal in the frequency domain is generally referred to as a *spectrum* or spectral representation, as in the frequency domain all the frequency components contained in the given signal are easily observed.

Spectral analysis can thus be defined as the technique of extracting hidden frequency components from a time-domain signal by transforming it into a frequency-domain signal [65, 66]. Figure 5.1, shows the spectral analysis of an artificial signal that contains 15, 30 and 50 Hz frequency components. In the time-domain (Figure 5.1-Top), one cannot identify the frequency components present in the signal, but once the signal is transformed to the frequency domain (Figure 5.1-Bottom), the frequency components contained in the signal are easily identified. In our case Fourier Transforms will be used to perform spectral analysis on geomagnetic signals. In this chapter we will discuss how Fourier Transforms work and the challenges that arise from using Fourier Transforms for spectral analysis.

5.1 Harmonic functions as the fundamental elements of Time Series Analysis

A time series is a collection of data points $x(t)$, observed at a particular time t [67]. The most interesting property of a time series is that it can be represented in both the *time-domain* and the *frequency-domain*. The advantage of analyzing a time series in the frequency-domain, is that hidden periodicities in a given data set are easily identified. Using Frourier Transforms, a

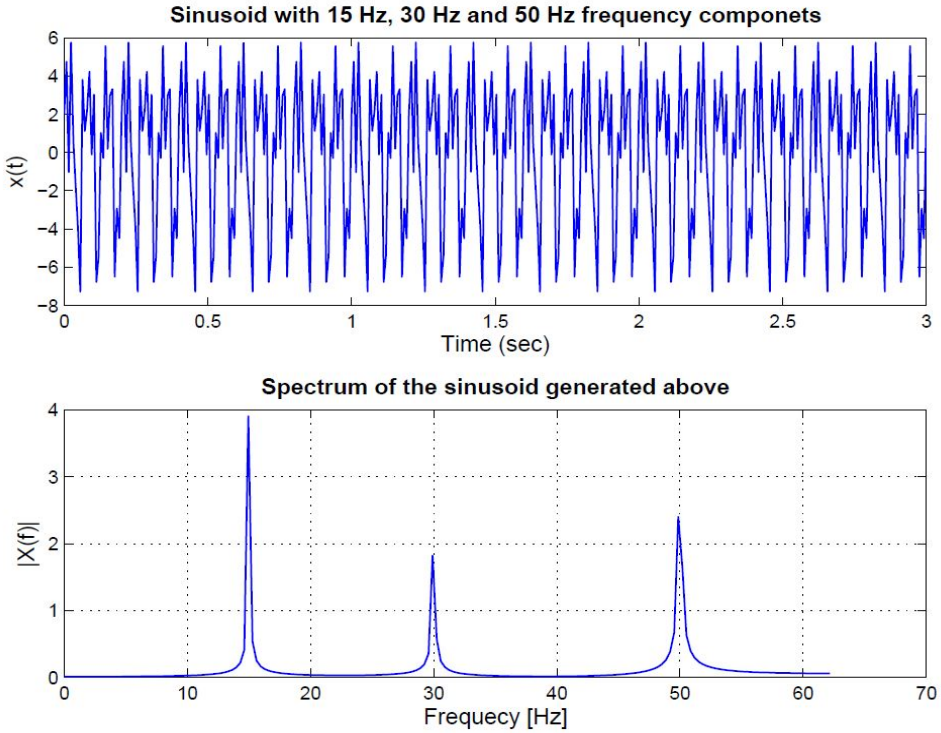

Figure 5.1: An artificial signal containing 15, 30 and 50 Hz frequency components: (Top) The signal is represented in the time-domain and in (Bottom) the signal is shown in the frequency-domain, where all the frequency components can easily be observed

time-domain time series is transformed into a frequency-domain time series by computing a weighted sum or integral of cosine and sine functions of harmonically increasing frequencies [65]. Periodic data with a single cosine wave, can be represented as [68]

$$x(t) = A\cos 2\pi(ft + \phi), \tag{5.1}$$

where A is an amplitude, f is the frequency of the sinusoid (in cycles per unit time) and ϕ is the phase. There are three basic properties of sinusoids that make them convenient for analysis of a time series. The first is that under change of time scales, the amplitude A remains unchanged. Let the time variable be $u = (t - a)/b$, so that $t = a + ub$, then $x(t)$ becomes,

$$\begin{aligned} x(u) &= x(a + ub) \\ &= A\cos 2\pi(fa + fub + \phi) \\ &= A\cos 2\pi(f'b + \phi'), \end{aligned}$$

where $f' = fb$ and $\phi' = \phi + fa$. The second property is that the sum of sinusoids with an identical frequency is another sinusoid with the same frequency. Any sinusoid with frequency f is a linear combination of two basic functions $\cos 2\pi ft$ and $\sin 2\pi ft$, and this is due to the fact that

$$A\cos 2\pi(ft+\phi) = A[\cos 2\pi ft \cos 2\pi\phi - \sin 2\pi ft \sin 2\pi\phi] \tag{5.2}$$

The third property is the orthogonality of the functions $\sin 2\pi ft$ and $\cos 2\pi ft$ [69].

$$\int_{T_0} \sin f_m t \sin f_n t dt = \begin{cases} 0, & m \neq n \\ T_0/2, & m = n \neq 0 \end{cases} \tag{5.3}$$

$$\int_{T_0} \cos f_m t \cos f_n t dt = \begin{cases} 0, & m \neq n \\ T_0, & m = n = 0 \\ T_0/2, & m = n \neq 0 \end{cases} \tag{5.4}$$

and

$$\int_{T_0} \sin f_m t \cos f_n t dt = 0, \qquad \text{all } m, n \tag{5.5}$$

where $T_0 = 1/f_0$ is a period of the fundamental, and n and m are integers. Equation 5.5 results from sine and cosine functions being $\pi/2$ out of phase.

5.2 Fourier Series

A Fourier Series is a representation of a periodic signal (time series) as a sum of weighted sinusoids whose frequencies are harmonics, or integer multiples, of a fundamental frequency [69]. This representation can either be in trigonometric or complex exponential form.

5.2.1 Trigonometric Series

The trigonometric Fourier Series of a periodic signal can be written as [70, 71]

$$\begin{aligned} x(t) = a_0 \quad &+ \quad a_1\cos(2\pi f_0 t) + a_2\cos(4\pi f_0 t) + \cdots \\ &+ \quad b_1\sin(2\pi f_0 t) + b_2\sin(4\pi f_0 t) + \cdots , \end{aligned} \tag{5.6}$$

which is evidently equivalent to

$$x(t) = a_0 + \sum_{n=1}^{\infty} a_n \cos 2\pi n f_0 t + \sum_{n=1}^{\infty} b_n \sin 2\pi n f_0 t. \tag{5.7}$$

Integrating Equation 5.7 term by term over one period of $x(t)$, a_0, which is the average of the waveform, is found to be

$$a_0 = \frac{1}{T_0}\int_{T_0} x(t)dt, \tag{5.8}$$

since the integration of a sine and cosine over a integral number of periods is equivalent to zero. Multiplying Equation 5.7 by $\cos 2\pi m f_0 t$, where m is integer valued, and using the orthogonality properties of the sine and cosine functions from Section 5.1, the equations to find a_n's and b_n's can be derived, and these are respectively as follows,

$$a_m = \frac{2}{T_0}\int_{T_0} x(t)\cos 2\pi m f_0 t, \quad m \neq 0, \tag{5.9}$$

and

$$b_m = \frac{2}{T_0}\int_{T_0} x(t)\sin 2\pi m f_0 t. \tag{5.10}$$

5.2.2 The Complex Exponential Fourier Series

The complex exponential Fourier series can be derived by substituting the complex exponential forms of cosine and sine into the trigonometric Fourier series Equation 5.7 [69]. Euler's formula states,

$$\sin 2\pi n f_0 t = \frac{e^{j2\pi n f_0 t} - e^{-j2\pi n f_0 t}}{2j}, \tag{5.11}$$

and

$$\cos 2\pi n f_0 t = \frac{e^{j2\pi n f_0 t} - e^{-j2\pi n f_0 t}}{2}, \tag{5.12}$$

where $j = \sqrt{-1}$. Thus Equation 5.7 can be mathematically manipulated to yield the complex exponential Fourier series in the form,

$$x(t) = \sum_{n=-\infty}^{\infty} X_n e^{j2\pi n f_0 t}, \tag{5.13}$$

where the X_n's are generally complex constants. Multiplying Equation 5.13 by $e^{-j2\pi n f_0 t}$ and integrating over any period of $x(t)$, X_n is found to be

$$X_m = \frac{1}{T_0}\int_{T_0} x(t)e^{-j2\pi m f_0 t}dt, \tag{5.14}$$

for $m = n$.

5.3 Fourier Transforms

The Fourier transform (sometimes referred to as a Fourier Integral) is generally considered as a formal limit of the Fourier series as the period approaches

infinity, i.e. $T_0 \to \infty$ [72]. Equations 5.13 and 5.14 can be conveniently rewritten in these forms [69], respectively,

$$x(t) = \sum_{nf_0=-\infty}^{\infty} \frac{X_n}{f_0} e^{j2\pi n f_0 t} \triangle (nf_0), \tag{5.15}$$

where $\triangle (nf_0)$ is the increment in the variable nf_0, i.e it increases by f_0. And,

$$X(f) \triangleq \frac{X_n}{f_0} = \int_{1/f_0} x(t) e^{-j2\pi m f_0 t} dt. \tag{5.16}$$

Since $f_0 = 1/T_0$, this means $f_0 \to 0$ as $T_0 \to \infty$, thus $n \to \infty$ such that $nf_0 \to f$ and $\triangle (nf_0) \to df$. This results in Equations 5.15 and 5.16 becoming

$$x(t) = \int_{-\infty}^{\infty} X(f) e^{j2\pi f t} df \tag{5.17}$$

and

$$X(f) = \int_{-\infty}^{\infty} x(t) e^{-j2\pi f t} dt. \tag{5.18}$$

These equations are often referred to as Fourier transform pairs and are denoted by the notation $x(t) \leftrightarrow X(f)$. This means that a continuous signal in the time-domain, $x(t)$, can be easily transformed to frequency domain, $X(t)$ (using Equation 5.18) and vice versa (using Equation 5.17). With all that said, one needs to note that not all signals can be Fourier transformed.

5.3.1 Dirichlet Conditions

For a function to be Fourier transformable it has to satisfy conditions known as *Dirichlet Conditions* [73, 71]. Those conditions are as follows:

- The functions $x(t)$ and $X(f)$ must be single-valued.
- The functions $x(t)$ and $X(f)$ must be 'piece wise', i.e., they can be broken into finite separate pieces.
- The functions $x(t)$ and $X(f)$ must have upper and lower bounds, and be absolutely integrable: $x(t)$ in the interval $[-\frac{1}{2}T_0, \frac{1}{2}T_0]$ such that

$$\int_{-T_0/2}^{T_0/2} |x(t)| dt < \infty, \tag{5.19}$$

  and $X(f)$ in the interval $[-1/2f_0, 1/2f_0]$ such that,

$$\int_{-1/2f_0}^{1/2f_0} |X(f)| df < \infty. \tag{5.20}$$

Thus, if the function $x(t)$ satisfies these conditions, it can be Fourier transformed to $X(f)$, i.e. transformed from the time-domain to the frequency-domain. The function $X(f)$ can also be transformed to $x(t)$, provided the conditions are met.

5.4 Discrete Fourier Transforms

In practice, signals or data are measured at discrete points with a finite number of data points. Since observed signals have a finite number of data points, they cannot be transformed using the Fourier transforms (Equations 5.15 and 5.16), because Fourier transforms are integrated from $-\infty$ to ∞ and requires continuous signals. In order to transform observed signals or artificial signals, which are discrete in nature, the Fourier transforms have to be approximated by finite sums. This results in what is known as *Discrete Fourier Transforms* (DFT) [73]. Let N be the total number of samples taken in T seconds interval, thus the time-sampling interval $\triangle\ t = T/N$ or the sampling frequency $f_s = N/T = 1/\triangle\ t$. The sampling frequency or the time-sampling interval is generally referred to as the *sampling rate*. Then the DFT can be represented as [69],

$$x_n = \frac{1}{N}\sum_{k=0}^{N-1} X_k e^{j2\pi kn/N}, \qquad n = 1, 2, ..., N \tag{5.21}$$

where n denotes discrete instances in time. And

$$X_k = \sum_{n=0}^{N-1} x_n e^{-j2\pi kn/N}, \qquad k = 1, 2, ..., N \tag{5.22}$$

where k represents discrete instances in frequency. The summations in Equations 5.21 and 5.22 may be over $0, 1, \ldots, N$ or $-N/2$ to $N/2$, but would still yield the same results [68]. The fact that DTFs are approximated from infinitely long and continuous Fourier transforms to finite discrete sums, give rise to distortions in the transformed spectrum [73]. Aliasing is one example of such distortions.

5.4.1 Aliasing

Suppose a signal is Fourier transformed from the time-domain, $x(t)$, to the frequency-domain, $X(f)$, using DFT Equation 5.22. From Equation 5.22, let $k = N + l$, i.e., k is greater that $N - 1$. Then Equation 5.22, can be re-written

as [70, 68]

$$\begin{aligned} X_{N+l} &= \sum_{n=0}^{N-1} x_n e^{-(j2\pi n/N)(N+l)}, \\ &= \sum_{n=0}^{N-1} x_n e^{-(j2\pi l/N)} e^{-(j2\pi n)}, \\ &= \sum_{n=0}^{N-1} x_n e^{-(j2\pi l/N)}, \\ &= X_l \end{aligned} \tag{5.23}$$

where $e^{-(j2\pi n)} = 1$, for all values of n. This means that for $k > N-1$, the coefficients X_k in Equation 5.22, will repeat themselves. Thus if we plot the $|X_k|$ along a frequency axis $f_k = k/N \triangle t$, where $\triangle t$ is the sampling rate or the time interval between observations, high frequency components contained in the input signal will produce ghost (spurious) frequency peaks in the lower frequency part of the output spectrum. This effect of high frequency components, contained in an input signal, creating ghost frequency peaks at the lower frequency part of the output spectrum, is known as *aliasing*. Aliasing can be avoided by making the sampling rate high enough, i.e. making the time-sampling interval small enough or the sampling frequency high enough. Let f_{max} be the highest frequency component present in the input signal. Then if the sampling interval, $\triangle t$, is made small enough so that,

$$f_{max} < \frac{1}{2 \triangle t} = \frac{f_s}{2} = f_N, \tag{5.24}$$

aliasing will be avoided. Here f_N denotes the *Nyquist frequency*, which is sometimes referred to as the *Folding frequency*. The Nyquist frequency is the highest frequency component that can be observed with the sampling rate of $\triangle t$. Frequency component of $f_N + f_a$ will appear to be at $f_N - f_a$ in the output spectrum [71], thus causing aliasing.

Consider a signal sampled at 125 Hz, i.e. the sampling-time interval, $\triangle t = 1/f_s = 8 \times 10^{-3}\ s$, with its maximum frequency component being 50 Hz. From the Nyquist equation (Equation 5.24), signals with a maximum frequency component less than 62.5 Hz can thus be Fourier transformed without the occurrence of aliasing in their spectrum, such as the case in Figure 5.1. However, if the signal had a maximum frequency component higher than the Nyquist frequency, say 80 Hz (62.5 + 17.5 Hz), then a ghost frequency component would appear in the spectrum at 62.5 − 17.5 Hz = 45 Hz, as shown in Figure 5.2. Ghost frequency components can easily be seen by varying the sampling rate. As the sampling rate is increased or decreased, ghost frequency components in the Fourier spectrum will shift by a certain factor, whereas real

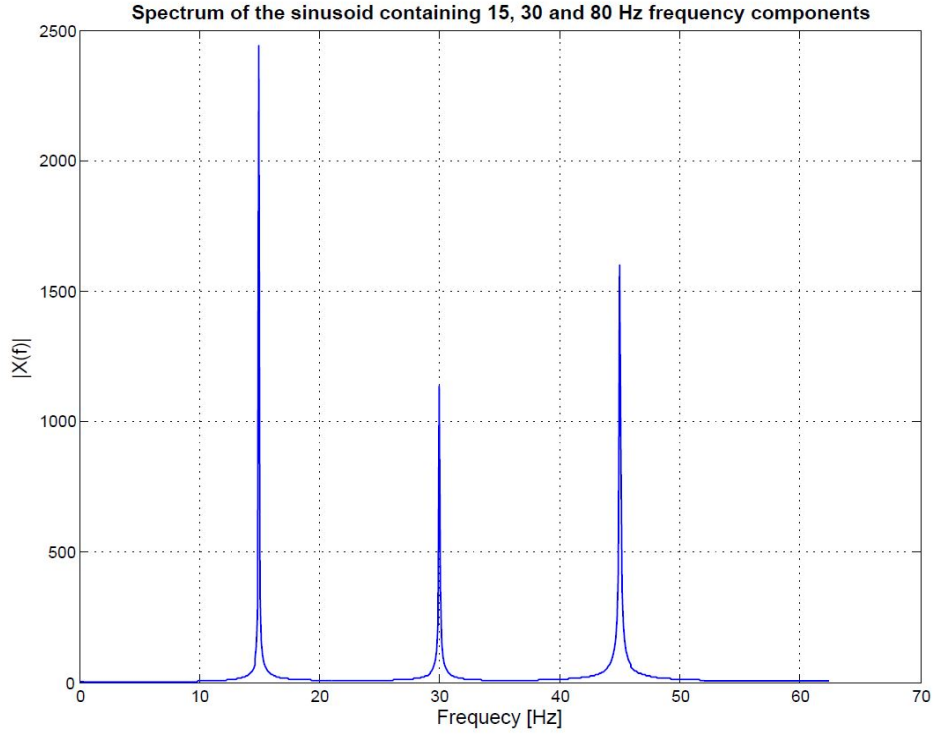

Figure 5.2: Fourier spectrum of an artificial signal sampled at 125 Hz (Nyquist frequency of 62.5 Hz), containing 15, 30 and 80 Hz frequency components. Frequency components (15 and 30 Hz) less than the Nyquist frequency creates no aliasing, while frequency component 80 Hz which is 17.5 Hz above the Nyquist frequency creates a ghost frequency component at 45 Hz (f_N − 17.5 Hz).

frequency components will maintain the same position all the time. In practice, sometimes its advisable to filter out high frequency components before Fourier transforming a given signal, to avoid aliasing [74, 70].

5.5 Fast Fourier Transforms

The discrete Fourier transform is only sufficient or effective for data sets with small number of samples, N [75]. Computing a DFT for data sets with larger N, requires a very long computing time. Since in practice, data sets usually have large number of samples, N, a much faster algorithm to compute the Fourier transform in the shortest time possible is needed. Fast Fourier Transforms (FFTs), which are just fast versions of DFTs, are instead used in computing Fourier transform for data sets with very large N. In the computation of a DFT, N^2 multiplications are required, while the FFT only requires

number of operations in the order of $N \log_2 N$ [70]. FFT is computationally processed much faster than a DFT.

5.5.1 Decimation-in-Time FFT algorithm

Consider a sequence $\{x_n\}$, $n = 0, 1, 2, \ldots, N-1$. This sequence can be split into two shorter sequences of even and odd indexed terms,

$$y_n = x_{2n}, \tag{5.25}$$

and

$$z_n = x_{2n+1}, \tag{5.26}$$

where $n = 0, 1, 2, \ldots, N/2 - 1$. The DFT of these two are,

$$Y_k = \sum_{n=0}^{N/2-1} y_n e^{-j\frac{2\pi nk}{N/2}}, \tag{5.27}$$

and

$$Z_k = \sum_{n=0}^{N/2-1} z_n e^{-j\frac{2\pi nk}{N/2}}, \tag{5.28}$$

respectively. Here $k = 0, 1, 2, \ldots, N/2 - 1$. The DFT from Equation 5.22 may be written as

$$X_k = \sum_{n=0}^{N/2-1} x_{2n} e^{-j\frac{2\pi(2n)k}{N}} + \sum_{n=0}^{N/2-1} x_{2n+1} e^{-j\frac{2\pi(2n+1)k}{N}}. \tag{5.29}$$

Substituting Equations 5.25 and 5.26, into 5.29, then,

$$X_k = \sum_{n=0}^{N/2-1} y_n e^{-j\frac{2\pi nk}{N/2}} + e^{-j\frac{2\pi k}{N}} \sum_{n=0}^{N/2-1} z_n e^{-j\frac{2\pi nk}{N/2}}. \tag{5.30}$$

Looking at Equations 5.27 and 5.28, it is evident that Equation 5.30 is just,

$$X_k = Y_k + e^{-j\frac{2\pi k}{N}} Z_k, \tag{5.31}$$

for $k = 0, 1, 2, \ldots, N/2 - 1$ [70, 69, 66]. It is clear that the FFT algorithm still contains the original DFT, but the original DFT is partitioned is such a way that FFT works much faster and is a bit more accurate than the original DFT.

5.6 Fourier Transforms Applications

There are different types of Fourier spectra with different practical applications. An artificial signal will be used to show different of these spectral types computed with MATLAB.

5.6.1 Amplitude Spectrum

The basic and simplest way to represent a spectrum is to represent its amplitude as a function of frequency. This type of spectrum is known as the *Amplitude Spectrum*(AS) [69]. From the FFT algorithm, Equation 5.31, the amplitude spectrum can be represented as $|X_k|$. If the input signal is measured in the units of nanoTesla (nT), then its amplitude spectral, $|X_k|$, will be also in nT. Suppose a signal, (see Figure 5.1):

$$x(t) = 4\sin(2\pi(15)t) + 2\cos(2\pi(30)t) + 3.2\sin(2\pi(50)t). \tag{5.32}$$

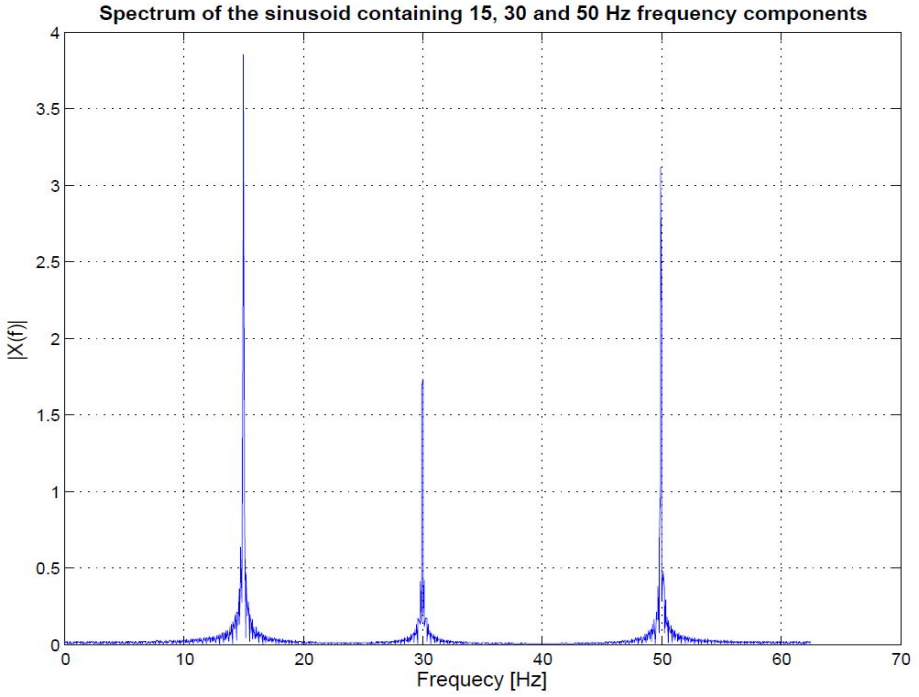

Figure 5.3: An Amplitude Spectrum: reveal frequency components present in the signal with their respective amplitudes.

With reference to Equation 5.1, it is clear that this signal contains three frequency components at 15, 30, and 50 Hz, with amplitudes 4, 2, and 3.2 respectively. The frequency components and their respective amplitudes are easily identifiable from an amplitude spectrum of this signal, as shown in Figure 5.3. However, the amplitudes of the amplitude spectrum are not exactly the amplitudes of the input signal since the signal have a finite length. The accuracy can be improved by increasing the length of the signal.

5.6.2 Power Spectrum

In practice, the signals that need to be Fourier transformed are generally noisy and the AS is sometimes not sufficient to identify frequency components contained in the noisy signals. For noisy signals, it is more suitable to use the *Power Spectrum*, (PS), which is simply the square of the amplitude spectrum, i.e., $PS = |X_k|^2$ [73]. The PS compresses the background noise and multiplies the amplitude of real frequency components, thus making them easily identifiable. Consider the signal in Equation 5.32, now with noise added. If an AS and PS are performed in the noisy signal,(see Figure 5.4), it is evident that PS is less noisy than the AS. The background noise that is present in the signal is greatly reduced in the PS as opposed to the AS. Since the PS is the square of AS, its units are nT^2 for an input signal with units nT.

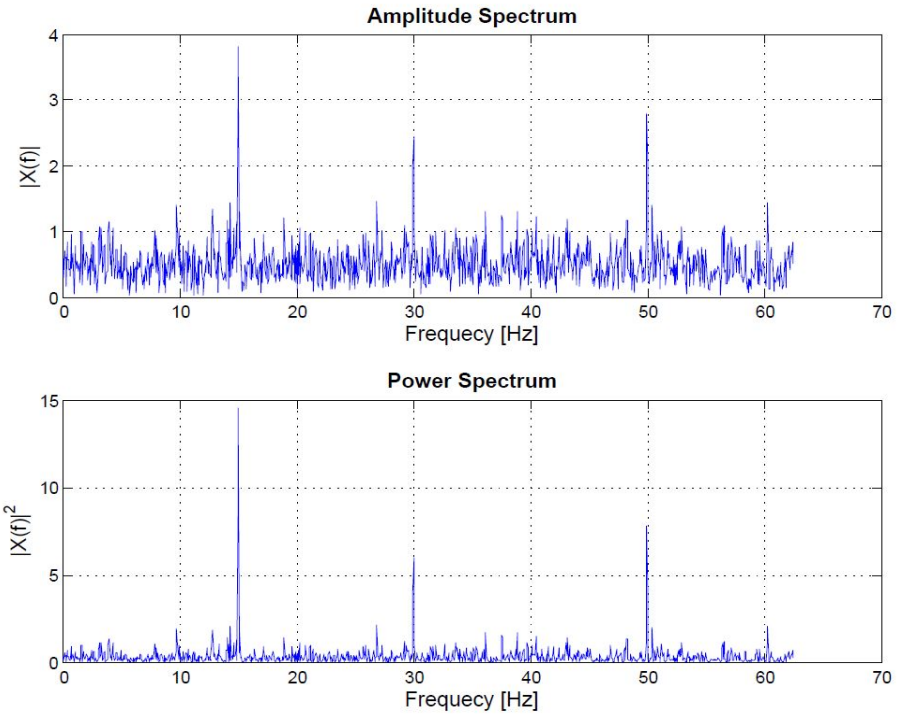

Figure 5.4: A comparison between Amplitude Spectrum and Power Spectrum of a noisy signal; its clear that the PS is less noisy than the AS, thus it is more suitable to use PS instead of AS when for noisy data.

5.6.3 Energy Spectral Density and Power Spectral Density

From Parseval's theorem, another form of spectrum, known as the *Energy Spectral Density* (ESD), can be expressed as $|X_k|^2 \times T^2$[76]. If T is in seconds and the input signal was measured in nT, then the units of this spectrum would be $[nT \cdot s]^2$ or $[nT/Hz]^2$. Fourier spectra are closely related. The *Power Spectral Density* (PSD) is easily derived from ESD by dividing it by the time interval T. This means it can be expressed as $|X_k|^2 \times T$, with units of $[nT^2 \cdot s]$ or $[nT^2/Hz]$[77].

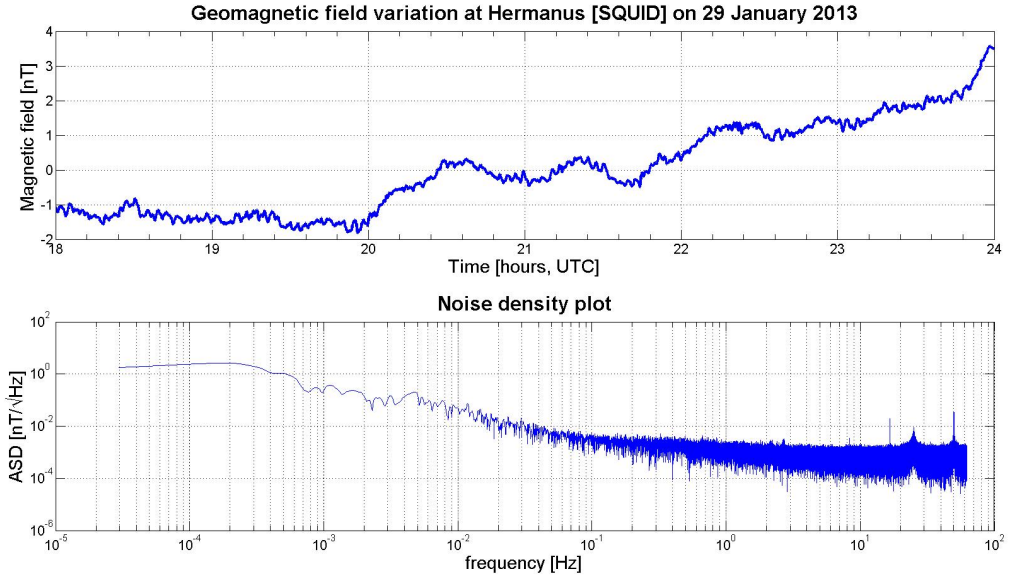

Figure 5.5: Noise density plot of Hermanus geomagnetic data.

5.6.4 Amplitude Spectral Density

The *Amplitude Spectral Density*, (ASD), results from taking the square root of the PSD, thus getting an expression, $|X_k| \times \sqrt{T}$. It has units of $[nT \cdot \sqrt{s}]$ or $[nT/\sqrt{Hz}]$. The noise spectrum may be obtained by taking a log-log plot of the ASD. For illustrative purpose, see Figure 5.5. A noise spectrum was computed using the ASD algorithm on the geomagnetic variation measured using a fairly new type of magnetometer known as a SQUID. White noise and $1/f$ noise can be easily seen from the noise density plot. The choice of which spectrum to use is generally determined by the type of data analyzed and the objective(s) of the user.

Chapter 6

Materials and Data acquisition methods

Data-sets used for this study were obtained from the SQUID and the Fluxgate magnetometers, both located at the South African National Space Agency (SANSA) Space Science, formerly known as the Hermanus Magnetic Observatory (HMO). The observatory is part of the world-wide network of magnetic observatories, the International Real-time Magnetic Observatory Network (INTERMAGNET). SANSA Space Science is situated in the small coastal town of Hermanus, and is in close proximity to the Atlantic Ocean and a small industrial area. However, the SANSA Space Science facility is magnetically clean to magnetic observatory standards.

6.1 Fluxgate data

Fluxgate data are obtained using a 3-axis FGE Fluxgate magnetometer. The FGE Fluxgate magnetometer was manufactured by the Danish Meteorological Institute in Denmark, and it has a band-width ranging from DC to 1 Hz. It is set up to measure the *hdz* geomagnetic components, see Section 4.5 for more details about geomagnetic components. However, the *hdz* Fluxgate data has to be compared to SQUID data which are the *xz* geomagnetic components. To obtain the x component of the Fluxgate data, it has to be mathematically derived using Equation 4.8,

$$x = h\cos(d). \tag{6.1}$$

The Fluxgate magnetometer is located in a magnetically clean hut within 50 meters from the SQUID magnetometer, thus they are virtually measuring the same field. The Fluxgate records data every second, with the data sampled every 5 seconds. A numerical filter is then applied to produce 1 minute data according to INTERMAGNET specifications. SANSA Fluxgate data are available at (`http://intermagnet.org/`) or can be directly obtained on site. The Fluxgate 1 minute data from INTERMAGNET are in IAGA-2002 format

with an extention of ".min". The file size is about 100 KB (One day data), with the first column being the "date", the second is "time", then "day of the year", followed by, "geomagnetic horizontal component - h", "declination - d", "z - component" and "total geomagnetic field strength - f".

6.2 SANSA Space Science SQUID system

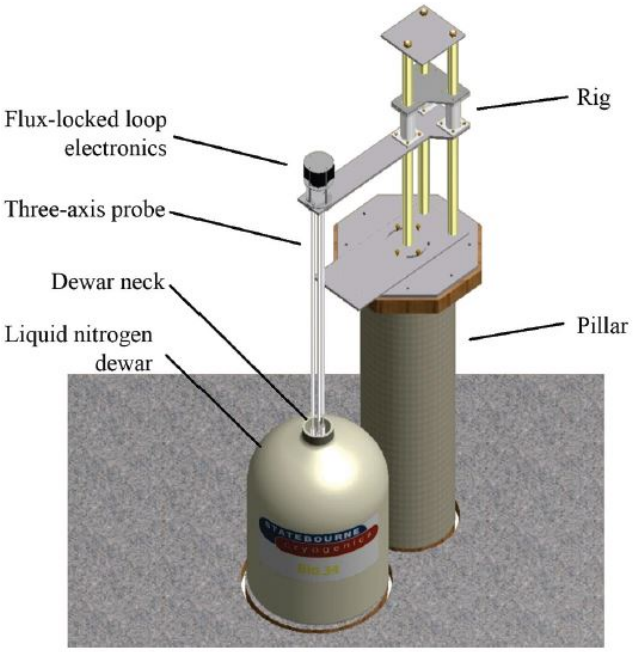

Figure 6.1: Schematic of SQUID dewar and rig (Image: courtesy of [4])

The SQUID at SANSA is a 2-axis High-T_c M2700 SQUID magnetometer from Star Cryoelectronics, with field noise characteristics of 300 fT/$\sqrt{\text{Hz}}$ at 10 Hz. The SQUID is operated at 77 K with the SQUID sensors immersed in liquid nitrogen contained in a non-magnetic dewar, as shown in Figure 6.1. The SQUID sensors are held by a non-magnetic rig which is used to lift the sensors in and out of the dewar during liquid nitrogen refills and to orientate the sensor in the $x - y$ plane. The dewar and the rig are both clamped to concrete pillars which are built on compressed sand and decoupled from each other, to minimize vibrations due to local disturbances. The SQUID is housed in a non-magnetic hut, with its floor and foundations also decoupled from the SQUID's dewar and rig pillars. For this study, the SQUID magnetometer was set up to measure only the x and z geomagnetic components. The magnetic field strength in Hermanus is about 23.6 μT in the vertical direction and 9.6

μT in the horizontal direction (x component). For further information about the SANSA SQUID refer to [4].

6.3 SQUID calibration and orientation

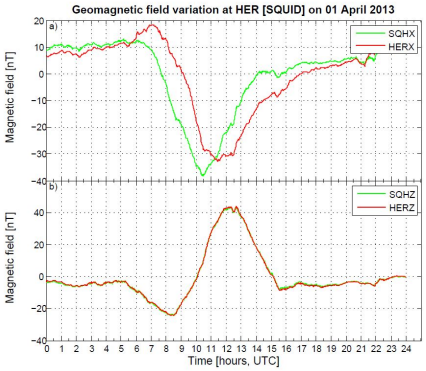

Figure 6.2: Comparison between Fluxgate and SQUID data-sets to investigate the alignment of the SQUID sensors with the x and the z geomagnetic components

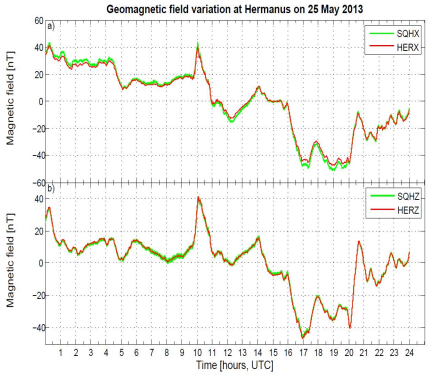

Figure 6.3: Comparison between Fluxgate and SQUID data-sets to show the SQUID sensors are aligned with the x and the z geomagnetic components, after orientation.

Currently the SANSA SQUID system is set up to measure magnetic variations in the geographical North to South direction (geomagnetic x component) and in the vertical downward direction (geomagnetic z component), with the y component of the SQUID sensor to be installed in the future. One of the challenges when setting up SQUID sensors is making sure that the sensors are measuring the desired geomagnetic component. The probes can rotate around their z-directed axes when the dewar lid is put in place, which makes it difficult to align the North-South sensor without an external reference. Since the SQUID system is in close proximity to the observatory's Fluxgate magnetometer, Fluxgate measurements serve as reference to check the alignment of the SQUID sensors to the desired geomagnetic components. The SQUID sensor measuring the geomagnetic z component is set up to be vertically aligned with the mechanical rig. Comparison between the SQUID z component measurements with that of the Fluxgate shows that the SQUID z component sensor is near perfectly aligned with geomagnetic z component, as seen on Figure 6.2b.

To measure the x geomagnetic component, the SQUID sensor must be orientated accordingly. Figure 6.2a shows the misalignment between the SQUID sensor and the geomagnetic x component, with the Fluxgate's x component used as a reference. To correct for the misalignment, the Fluxgate data are

used to determine the declination angle, d. Then, using a telescopic B3 landing compass with an accuracy of 0.1 degrees, Magnetic North (h component) is determined: see Figure 6.4 for the illustration of the alignment procedure. Once the Magnetic North is established, the landing compass is set up so that it is $90 + 25 = 115$ degrees clockwise from the Magnetic North plane, thus facing True West. The SQUID sensor is then orientated parallel to the True West plane, thus leaving the sensor near perfectly aligned with the True North. Figure 6.3 shows the comparison of the SQUID and Fluxgate data for the optimal aligned SQUID sensors.

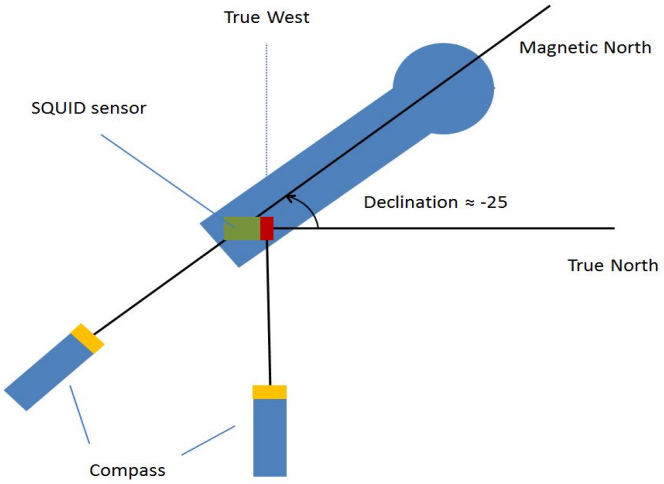

Figure 6.4: Schematic showing the procedure of aligning the SQUID x component data with the geomagnetic x component.

6.4 SQUID data acquisition

The voltage output of SQUID sensors are recorded using a National Instruments data acquisition unit (NI-DAQ USB-6281) with 18 bit analogue to digital converters and external triggering for synchronizing with the GPS time stamping system [4]. The DAQ is currently sampled at 125 Hz, but for high frequency measurements it can be sampled up to 500 kHz. To prevent aliasing from high frequency components, the SQUID sensor outputs are filtered by fourth order Butterworth active analogue filters with cutoff frequencies at 50 Hz, before being fed to the DAQ. With this data acquisition system, the SANSA SQUID setup can currently measure the amplitude of the field strength as low as 5 pT (the limit results from the sampling resolution of the DAQ, but not from the SQUIDs). SQUID data are stored on-site in a control room

at SANSA Space Science and are available for research purposes on a server at the Department of Electrical and Electronic Engineering at Stellenbosch University. The server is accessed via (`http://geomagnet.ee.sun.ac.za/`). SQUID data files are very large, with one full day's data being as big as 1 GB. The files are saved with the first column containing the "date", the second one is "time", followed by "micro second", the "filtered x component", a dummy column, the "filtered z component", a total field column, "unfiltered x component", a dummy column and "unfiltered z component". The dummy columns are provided for the future y axis.

6.5 SQUID (or Flux) jumps

Figure 6.5a shows SQUID or Flux jumps, encircled in red. SQUID jumps can either arise when the read-out system (FLL) loses and regains lock at another quantum level or appear as very low-frequency telegraph noise due to a trapped fluxon hopping between two (or more) pinning sites within the SQUID or flux transformer's structure, and/or due to a critical current fluctuation in a Josephson junction [1]. SQUID jumps due to a trapped fluxon jumping between two (or more) pinning sites typically occur in systems operated in an unshielded environment or with poor signal-to-noise ratio. For any of these cases, SQUID jumps can be greatly reduced/avoided by shielding the SQUID system from external interferences. The SQUID system at Hermanus is used to monitor or measure the geomagnetic field, hence it is operated completely unshielded. However, SQUID jumps can be manually eliminated from data as they are easily noticeable on the SQUID output. Computing the difference between two consecutive points, as shown in Figure 6.5b, the SQUID jumps can be easily identified with their corresponding times and amplitudes. This difference is calculated using the following equation,

$$x_i - x_{i+1}. \tag{6.2}$$

Plotting the difference between consecutive points against time, the jumps will appear as spikes at their corresponding time, see Figure 6.5b. Thus suitable adjustments can be made to eliminate the jumps as indicated in Figure 6.5c.

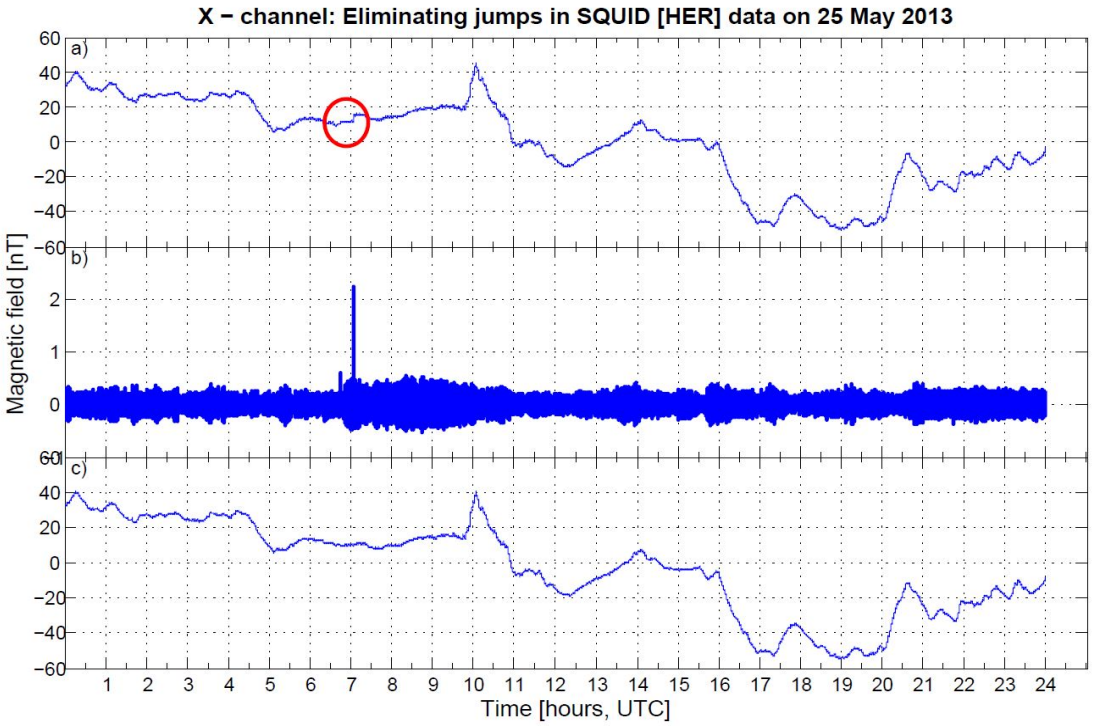

Figure 6.5: Elimination of jumps in the SQUID data (x channel): a) Geomagnetic variation measured in the x channel, with SQUID jumps encircled in red, b) The difference between two consecutive data points in the data plotted in a) - sharp peaks correspond to magnetic jumps in the data and c) Data plotted in a) now with magnetic jumps eliminated.

Chapter 7

Data Analysis

This chapter presents the comparison between geomagnetic data-sets from the SQUID and Fluxgate magnetometers located at the South African National Space Agency (SANSA) Space Science, Hermanus (South Africa). The two magnetometers are located within 50 m from each other. The frequency content of the two data-sets, obtained from these two magnetometers, were correlated for geomagnetic storms that occurred in the year 2013. This correlative study is aimed at validating the use of SQUID magnetometers as valid and reliable instruments for Space Weather or geophysical research.

Geophysical phenomena, such as earthquakes, volcanoes, and geomagnetic storms, are known to generate geomagnetic perturbations in the ionosphere and the magnetosphere. These geomagnetic perturbations are observable from geomagnetic data recorded at the Earth's surface. Thus studying geomagnetic data serves as tool for further understanding many geophysical phenomena or even predicting some of these phenomena. Conventional magnetometers, such as Fluxgates, have been used for decades for Space Weather research, monitoring the geomagnetic field. Thus comparing the performance of new magnetometers, such as SQUIDs, to magnetometers that have been tried and tested in Space Weather research can indicate whether SQUIDs are reliable for Space Weather research. In this study the comparison is performed between Fluxgate and SQUID magnetometers for geomagnetic storms. The frequency content of Fluxgate data-sets are compared to that of SQUID data-sets, thus investigating if the frequency peaks observed in a Fluxgate data-sets are also present in a SQUID data-sets.

The storms (days) studied were selected based on the Dst index. The Dst index is a measure of the strength of the horizontal geomagnetic component around the equator. On normal days (magnetically quiet), the Dst index is typically zero, or more accurately within $\pm$ 20 nT. However, during geomagnetically disturbed times (storms), the Dst index drops significantly to negative values in a short space of time. This sudden drop of the Dst index is known as the main phase of a geomagnetic storm, see Section 4.6.1. For each storm

only geomagnetic data recorded during the main phase of the storm were investigated. The Kp index, which reflects global geomagnetic activity, was also used to identify geomagnetic disturbances on storm days. Days with Kp index less than 4 are considered to be geomagnetically quiet.

The frequency range at which the two data-sets can be compared is limited by two factors, the high $1/f$ ($f-$ frequency) noise of the SQUID data below 1 mHz and the Nyquist frequency of the Fluxgate data. The Fluxgate data (INTERMAGNET) is sampled every minute, thus its Nyquist frequency is 8.33 mHz according to Equation 5.24. Due to these restrictions, the two data-sets were compared for the frequency range of 1−8 mHz only. Many of the geophysical phenomena are associated with millihertz range resonances [64], thus the frequency range (1−8 mHz) have great scientific significance. Just to mention a few, geomagnetic storms, lightning and ground motions (earthquakes) are known to produce geomagnetic pulsations with some peaks within the frequency range of 1−8 mHz or just above it.

7.1 Geomagnetic variations

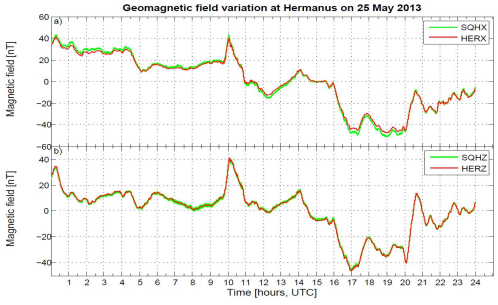

Figure 7.1: Geomagnetic variations at Hermanus, recorded using the SQUID (SQH) and Fluxgate (HER) magnetometers.

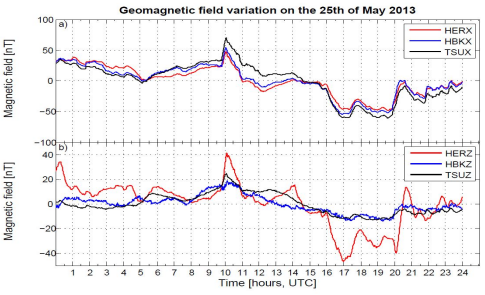

Figure 7.2: Comparison between Fluxgate data-sets obtained from Hermanus (HER), Tsumeb (TSU) and Hartebeesthoek (HBK).

Geomagnetic magnetic variations are produced by external (outside the magnetosphere) processes, such as variations in the solar dynamic pressure and internally from geophysical phenomena such as lightning or tidal motions. Significant geomagnetic variations are experienced during magnetic storms. During geomagnetic storms vast amounts of electromagnetic energy are deposited inside the magnetosphere, inducing currents that cause significant surface geomagnetic variations. Figure 7.1, shows the geomagnetic variations measured at Hermanus using both the SQUID and Fluxgate magnetometers on the 25th of May 2013 during a geomagnetic storm. The two magnetometers

are less than 50 m apart and from Figure 7.1 it is clear that they are virtually measuring the same geomagnetic field variations.

Computing the correlation coefficient further proves that the two magnetometers are measuring essentially the same field, where the full day signals are correlated in the time domain. The correlation between the measurement of the two magnetometers, in Figure 7.1, was found to be 0.9993 for the x component data and 0.9999 for the z component. The correlation was computed using a Matlab function "*corr*" which calculates the Pearson linear correlation coefficient between two given functions - which assesses linear association between two variables. The correlation coefficient ranges from -1 to $+1$, with positive correlation meaning that the two quantities increases mutually while negative correlation is when the one quantity decreases as the other increases. Moreover, 1 indicate that correlation is strong while 0 indicates there is no correlation between the given quantities.

The geomagnetic variations measured by Fluxgate magnetometers (25th of May 2013), from Hermanus (34.400°S, 19.200°E), Hartebeesthoek (25.900°S, 27.700°E) and Tsumeb (19.200°S, 17.600°E) magnetic observatories, were compared in Figure 7.2. The correlation between the Hermanus and Hartebeesthoek Fluxgates was found to be 0.9754 and 0.7622 for the x and z components, respectively. Consequently the correlation was 0.9051 and 0.7170 for the respective x and z components of Fluxgate data-sets obtained from Hermanus and Tsumeb. For the Tsumeb and Hartebeesthoek data, the correlation was 0.9545 for the x component while it was 0.8585 for the z component. The lower correlation seen between Hermanus and both the Tsumeb and Hartebeesthoek data for the z component is to be expected due to the latitudinal dependence of geomagnetic variations, especially for vertical geomagnetic components. The correlation between the Hartebeesthoek and Tsumeb data is better because they are latitudinally closer to each other than Hermanus is to both of them.

7.2 Magnetic Noise Profile

To investigate noise on both the SQUID and Fluxgate magnetometers, a log-log noise profile was computed and analyzed for both the instruments. The noise profiles of the SQUID and Fluxgate magnetometers were computed for a geomagnetically quiet day, i.e, a day with the K index at least less than 4. The K index indicates the degree of disturbance of the local horizontal component of the geomagnetic field. Figure 7.3 shows the K index computed at SANSA Space Science magnetic observatory from the 1st to the 5th of July 2013. From Figure 7.3, the 2nd of July was geomagnetically the most quiet day, but due to lack of quality data for that day, the noise profiles were computed for the 3rd instead.

Figure 7.4 shows the magnetic noise profiles for SQUID (green) and Flux-

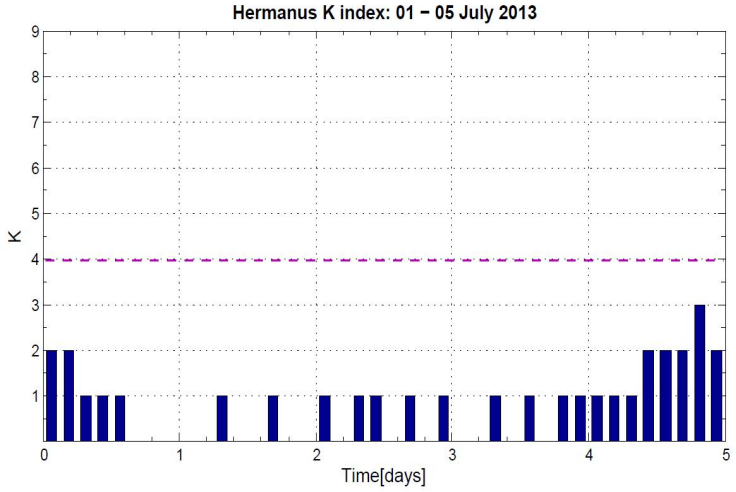

Figure 7.3: Hermanus K index over five days, indicated above

gate (red) data on the 3rd of July 2013. At 1 mHz the mean field noise is found to be 22.06 $\mathrm{nT}/\sqrt{\mathrm{Hz}}$ and goes to 5.33 $\mathrm{pT}/\sqrt{\mathrm{Hz}}$ at 10 Hz. The SQUID noise profile is dominated by $1/f$ noise, with the white noise being more apparent above 10 Hz (or just below). The 50 Hz frequency peak which is due to the electromagnetic waves from the national electricity grid, is also present in the SQUID noise profile. For the Fluxgate magnetometers from SANSA Space Science observatory, Hermanus, and Hartebeesthoek observatory, their respective magnetic noise profiles show mean field noise of 19.05 $\mathrm{nT}/\sqrt{\mathrm{Hz}}$ and 16.30 $\mathrm{nT}/\sqrt{\mathrm{Hz}}$ at 1 mHz. Moreover, the mean fied noise reduces to 3.16 $\mathrm{nT}/\sqrt{\mathrm{Hz}}$ at 8 mHz for the Hermanus Fluxgate and to 6.79 $\mathrm{nT}/\sqrt{\mathrm{Hz}}$ for the Hartebeesthoek Fluxgate. Since the field noise of the SQUID and the Fluxgates are in the same range, it follows that the noise field for both the magnetometers are due to environmental sources and not that of the instruments. The noise profile of Hermanus Fluxgate is shown in Figure 7.4 (in red) and Figure 7.5 shows that of Hartebeesthoek Fluxgate. The noise profiles of the Fluxgate magnetometers show that $1/f$ noise dominates below 1 mHz while white noise is visible above 1 mHz. With the $1/f$ noise from the SQUID and Fluxgate sensors in the same range, it shows that the $1/f$ noise is inherent to the signal, not the sensors.

7.3 Storm Analysis

The frequency content of both the data-sets obtained from the SANSA SQUID and Fluxgate magnetometers were compared by taking an FFT (amplitude spectral density - ASD) of a full day's (24 hours) time-domain data. The ASD of the SQUID x and z component data were correlated to the respective x and z components of the Fluxgate data. Here, correlation means the comparison

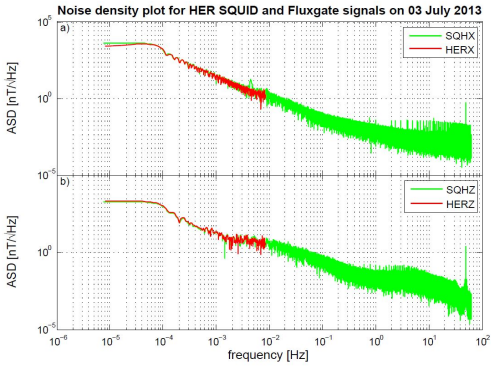

Figure 7.4: Hermanus SQUID and Fluxgate magnetic noise profiles

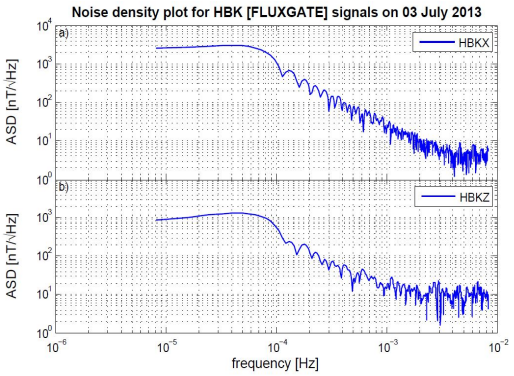

Figure 7.5: Hartebeesthoek Fluxgate magnetic noise profile

of the frequency content of SQUID and Fluxgate data sets, i.e., investigating if frequency peaks found in Fluxgate data coincide with the frequency peaks present in SQUID data. Only frequency peaks that were within 5% from each other were considered coinciding; 5% is the same range used in the previous study [9] (for consistence). A total of six storms were studied, two occurring in May, the other three in July and the last one in October. All the storms occured in the year 2013 and were of different intensities.

7.3.1 May 2013

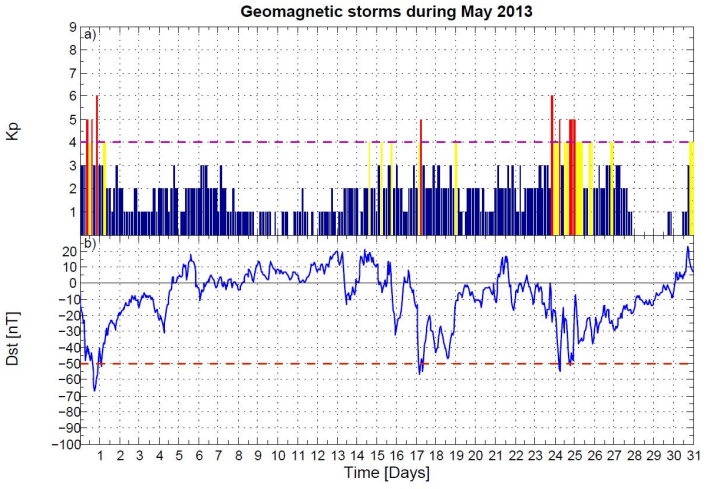

Figure 7.6: Geomagnetic disturbances during the month of May 2013, a) Kp index and b) Dst index.

Figure 7.6 shows geomagnetic disturbances during the month of May 2013. From the Dst plot, Figure 7.6b, it is clear that during this month at least three significant geomagnetic storms occurred. The first storm started on the 1st of May, with the geomagnetic horizontal component dropping just before 00:00 UT and reaching its lowest value around 19:00 UT. This geomagnetic storm will be referred to as "*Storm 1*". The second significant storm took place on the 18th, but due to lack of data for that day it was not considered for this study. The third storm took place on the 25th of May and it is hereafter referred to as "*Storm 2*". The strength of the horizontal component started to decline as from the 24th and appeared to be recovering going to on the 25th. However, on the 25th, it declined much further and reached its lowest around 08:00 UT. As the H-component was recovering, it dropped again around 12:00 before it started to recover as the 25th was about to end. Using the geomagnetic storm classification discussed earlier (see Section 4.6), Storm 1 can be classified as a *moderate storm*, while Storm 2 is a *minor* storm.

Storm 1 (Moderate)

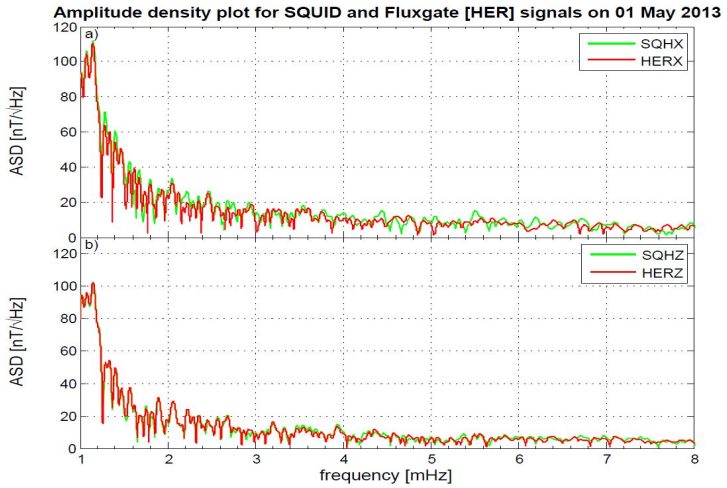

Figure 7.7: Amplitude spectral density of SQUID data-set compared to the amplitude spectral density of the Fluxgate data-set. a) x component and b) z component.

Storm 1 (main-phase) occurred on the 1st of May 2013. The amplitude spectral density of the x- and z- components of both the SQUID and Fluxgate data are compared in Figure 7.7. Comparing the x components of these magnetometers, Figure 7.7a, 86.21 % of the frequency peaks present in the x component Fluxgate data, are also present in the SQUID x component, with an exception of frequency peaks located at 1.849, 4.079, 4.164, 4.305, 5.264,

5.410, 5.580 and 6.412 mHz. Moreover, frequency peaks found at 3.016, 4.112, 4.239, 5.326, 5.834, 6.027, 6.196, 6.483 and 6.723 mHz in the SQUID data are not present in the Fluxgate data. For the z component, all (100 %) frequency peaks found in the Fluxgate data are present in the SQUID data and vice versa, see Figure 7.7b. Thus the correlation between the SQUID and Fluxgate data-sets for this storm is 93.11 %. About 90 % of the peaks from SQUID data that coincided with Fluxgate peaks were within 0.5 % of the Fluxgate peaks.

Storm 2 (Minor)

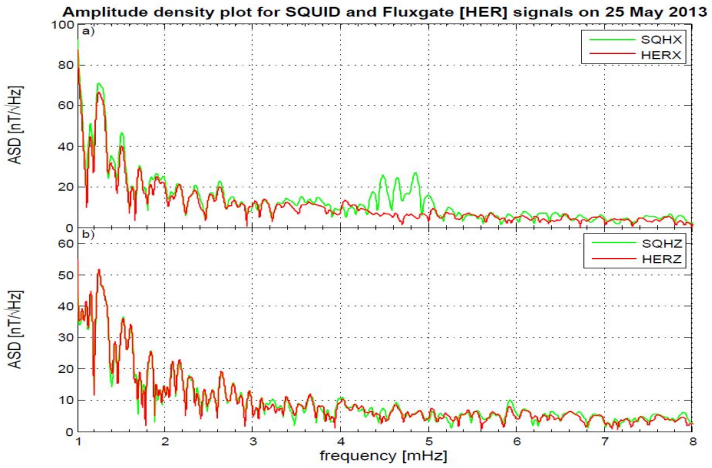

Figure 7.8: Amplitude spectral density of SQUID data-set compared to the amplitude spectral density of the Fluxgate data-set. a) x component and b) z component.

Figure 7.8 shows the amplitude spectral density of both the SQUID and Fluxgate data-sets recorded on the 25th of May 2013, during the main phase of a storm. The x and the z components of both the SQUID and Fluxgate data are respectively compared in terms of their frequency content. All the significant frequency components contained in both x and z components of the Fluxgate data, appear in the x and z components of SQUID data, respectively. Thus, for this particular day the SQUID data correlates 100 % with Fluxgate data. However, not all the frequency components contained in the SQUID data are present in the Fluxgate data. Over 92 % of the SQUID peaks lied within 0.5 % of Fluxgate peaks.

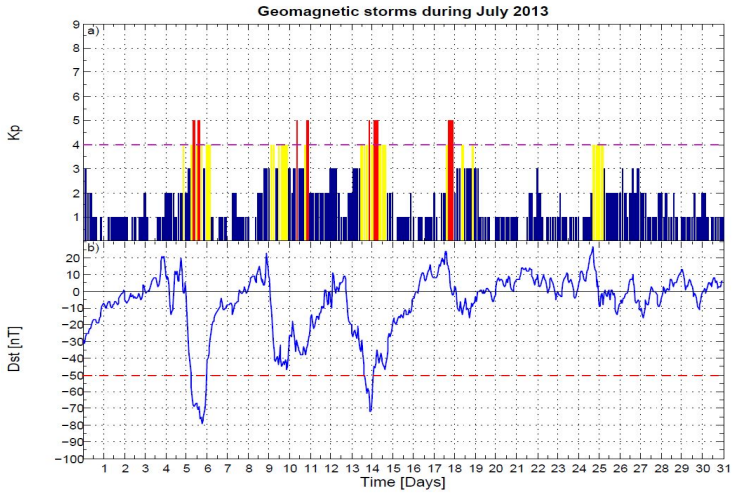

Figure 7.9: Geomagnetic disturbances during the month of May 2013, a) Kp index and b) Dst index.

7.3.2 July 2013

Figure 7.9 shows the Dst and Kp indices for the month of July. With reference to the Dst index, Figure 7.9b, a total of three storms occurred during July 2013. The first storm, which will be referred to as "*Storm 3*" for this study, occurred on the 6th, with the main phase of the storm starting just before 00:00 UT. Immediately after the Dst or horizontal component recovered from Storm 3, another storm followed. This storm, "*Storm 4*", took place on the 10th and the 11th. The third and last storm of the month, "*Storm 5*", was on the 14th of July. Using the Dst values, Storms 3 and 5 can be classified as *moderate storms* while Storm 4 is a *minor storm*.

Storm 3 (Moderate)

Figure 7.10 shows the x and z components of the Fluxgate data recorded on the 6th of May compared to those of the SQUID data for the same day. In Figure 7.10a 82.26 % of the frequency peaks found in the Fluxgate x component data were also present in SQUID x component data. Frequency peaks found at 1.887, 2.997, 3.369, 4.248, 4.484, 5.175, 5.396, 5.481, 6.092, 6.337, 6.808 and 7.626 mHz, in the Fluxgate data were not present on the SQUID data, consequently, peaks found at 1.341, 2.503, 2.729, 3.138, 3.284, 4.564 and 4.945 mHz in the SQUID data was not present in the Fluxgate data. Figure 7.10b shows the z component, where 87.30 % of the peaks present in the Fluxgate data were also found in SQUID data with only frequency peaks found at 2.762, 4.963, 5.217, 5.283, 5.356, 5.815, 5.895 and 6.742 mHz absent. Moreover, peaks found at 1.214, 2.503, 2.729, 3.138, 3.284, 4.564 and 4.945 mHz were absent

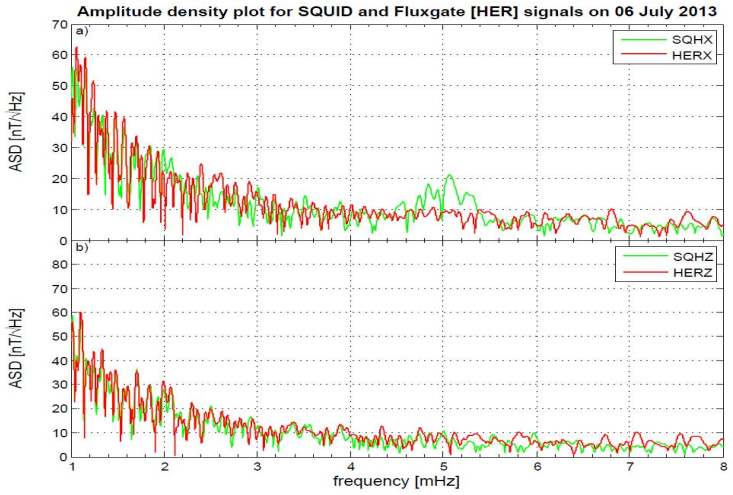

Figure 7.10: Amplitude spectral density of SQUID data-set compared to the amplitude spectral density of the Fluxgate data-set. a) x component and b) z component.

in the Fluxgate data. Overall, SQUID data correlates with Fluxgate data by 84.78 %. For this storm, about 66 % of the SQUID frequency peaks were within 0.5 % of Fluxgate peaks.

Storm 4 (Minor)

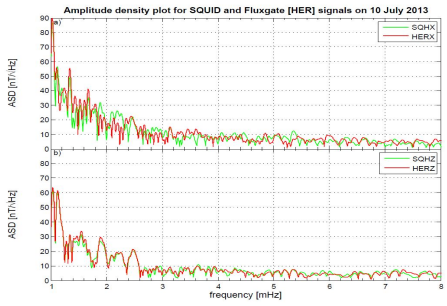

Figure 7.11: Amplitude spectral density of SQUID data-set compared to the amplitude spectral density of the Fluxgate data-set. a) x component and b) z component.

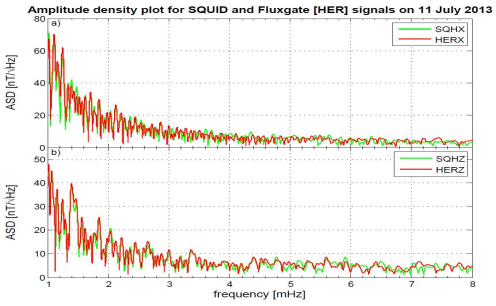

Figure 7.12: Amplitude spectral density of SQUID data-set compared to the amplitude spectral density of the Fluxgate data-set. a) x component and b) z component.

Storm 4 was analysed over two days, the 10th and 11th of July, represented by Figures 7.11 and 7.12 respectively. On the 10th the comparison between the x component of both the SQUID and Fluxgate data-sets showed that 86.67

% of the peaks found in the Fluxgate data are also present in the SQUID data, with peaks at 2.131, 3.609, 4.135, 4.248, 5.086 and 5.443 mHz absent. Moreover, for the z component, 88.89 % of the peaks from Fluxgate are also present in the SQUID data, with the exception of peaks located at 1.750, 1.797, 3.030 and 4.135 mHz. Frequency peaks found at 1.195, 1.468, 3.063, 3.383, 3.430, 3.830 and 4.921 mHz in the SQUID x component data and at 4.404 and 4.921 mHz in the z component data, were absent in the respective Fluxgate's x and z components data.

For the 11th, only 89.58 % of the peaks found in the Fluxgate's x component data were also present in the SQUID data, with peaks at 1.426, 2.394, 2.498, 3.637 and 3.881 mHz absent. Frequency peaks found at 2.183, 2.310, 2.922, 3.242, 3.331, 4.023, 4.352 and 4.728 mHz in the SQUID's x component data were absent in the Fluxgate data. The SQUID's x component data contained 90.91 % of the peaks found in the Fluxgate data, with only peaks at 1.976, 4.526, 4.596 and 5.297 mHz missing. The overall correlation of SQUID data to Fluxgate is 89.01 % for this storm, with over 75 % of the SQUID peaks within 0.5 % of Fluxgate peaks.

Storm 5 (Moderate)

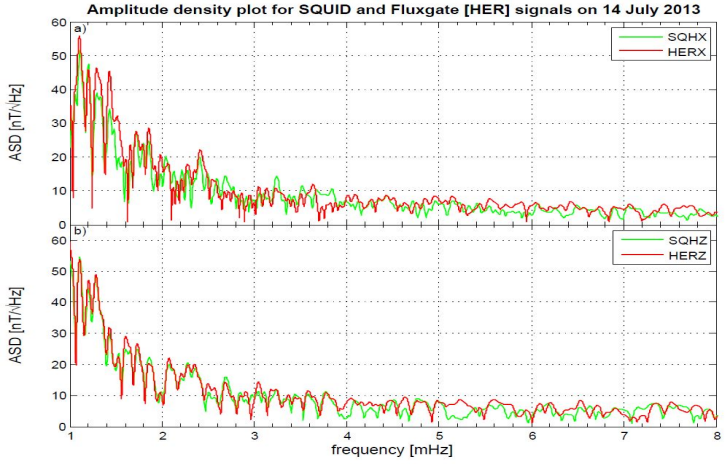

Figure 7.13: Amplitude spectral density of SQUID data-set compared to the amplitude spectral density of the Fluxgate data-set. a) x component and b) z component.

Storm 5 took place on the 14th of July. The SQUID's x component data contained 88.57 % of the frequency peaks found in the Fluxgate's x component data, with only peaks at 2.169, 2.545, 2.630 and 2.724 mHz absent from the SQUID data. Moreover, frequency peaks at 1.059, 1.327, 1.478, 1.571 2.494

and 3.849 mHz in the SQUID data are also not present in thet Fluxgate data. For the z component, Figure 7.13b, 93.33 % of frequency peaks in the Fluxgate data are also found in the SQUID data, with only the exception of peaks at 3.185 and 4.634 mHz. The correlation overall was 90.95 %, with over 75 % of SQUID frequency components with in 0.5 % of Fluxgate.

7.3.3 October 2013

In the month of October 2013, a couple of geomagnetic storms occurred. However, only the storm that took place on the 2nd of October will be discussed. The Dst index decreased as low as -75 nT on this day, while the Kp increased to 8, Figure 7.14. Sudden storm commencement took place at around 03:00 UT followed by the main-phase until about 08:00 UT. According to the Kp index this storm can be classified as an intense storm.

Storm 6 (Intense)

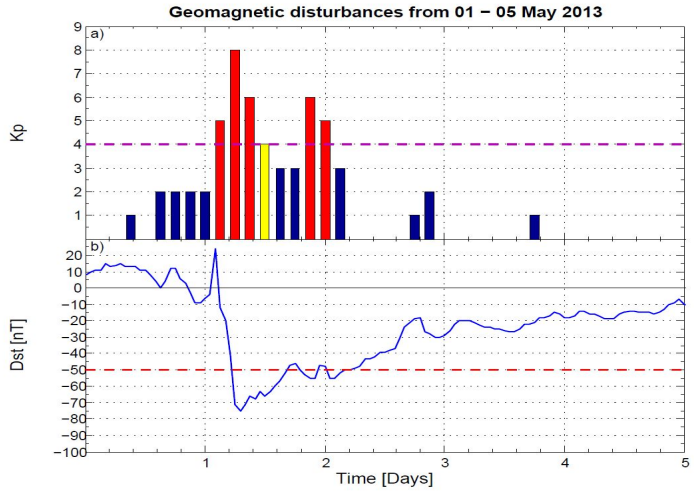

Figure 7.14: Geomagnetic disturbances from the 1st to the 5th of October 2013 a) Kp and b) Dst indices.

Storm 6 occured on the 2nd of October 2013, as seen from Figure 7.14b. The correlation between the SQUID and Fluxgate data-sets recorded on the day of the storm's main phase is as follows; Comparing the SQUID's and Fluxgate's x component data, it was found that 80.56 % of the frequency peaks in the Fluxgate data are also present in the SQUID's data, see Figure 7.15a. Moreover, frequency peaks at 1.303, 1.412, 1.844, 3.002, 4.046, 5.208 and 5.617 mHz were only present in the Fluxgate data. Frequency peaks at 1.181, 1.355, 2.211 and 4.107 mHz found in the SQUID data, were absent in

the Fluxgate data. Comparison of the SQUID z component data with that of the Fluxgate, also showed a good correlation of the frequency peaks contained in the two data-sets. It was found that 87.5 % of the frequency peaks present in the Fluxgate data are also present in the SQUID's data. Only frequency peaks at 3.021, 3.566 and 5.152 mHz in the Fluxgate data, were absent in the SQUID data. Overall, 84.03 % of the frequency peaks in the Fluxgate data were also present in the SQUID data, with over 85 % lying within 0.5 % of Fluxgate peaks.

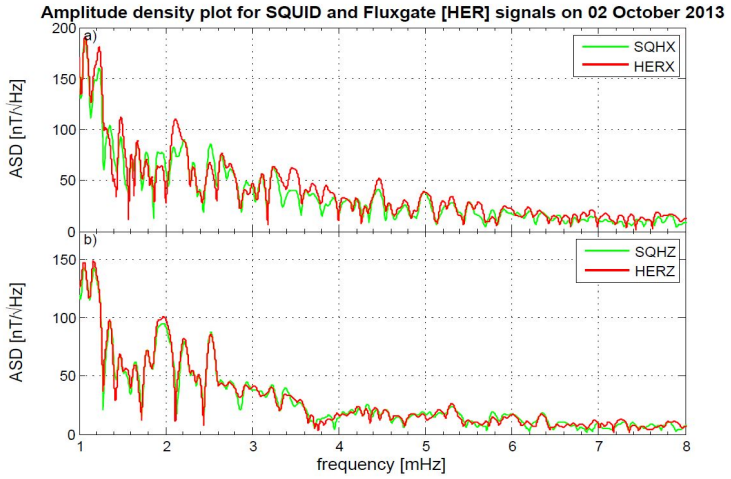

Figure 7.15: Amplitude spectral density of SQUID data-set compared to the amplitude spectral density of the Fluxgate data-set. a) x component and b) z component.

7.4 Coinciding frequency peaks

The comparison of the x and z components of both the SQUID and Fluxgate data, showed that there were frequency peaks appearing (coinciding) in both axes for SQUID and Fluxgate data, as listed in Table 7.1 for each storm studied. All bold (hereafter) frequency peaks fall $\pm$ 0.1 mHz from the so called "*magic*" frequencies, which are frequency peaks that constantly appear in geomagnetic data but due to lack of direct evidence to specific sources they were termed magic frequencies. These peaks appear at frequencies, 1.3, 1.9, 2.6, 3.1, 3.4 and 4.2 mHz [78] in geomagnetic data and they are associated with different Solar wind-Magnetosphere-Ionospheric processes. Frequency peak 1.3 mHz and other lower peaks, have been associated with geomagnetic pulsations due to variations in the solar wind dynamic pressure [64].

Table 7.1: Coinciding frequency peaks: Peaks appearing in both the x and z components of both the SQUID and Fluxgate data

Coinciding Frequency Peaks [mHz]						
Storm 1	Storm 2	Storm 3	Storm 4a	Storm 4b	Storm 5	Storm 6
1.073	1.153	1.017	1.021	1.012	1.111	1.054
1.148	**1.247**	1.064	1.125	1.106	1.205	1.473
1.289	1.510	1.106	**1.280**	1.162	**1.294**	1.788
1.336	1.609	1.158	**1.341**	**1.247**	1.430	**1.986**
1.402	1.713	**1.242**	1.416	**1.332**	1.558	–
1.473	1.774	**1.294**	1.548	**1.388**	1.605	–
1.567	**1.840**	**1.332**	1.619	1.482	1.717	–
1.619	**1.906**	**1.388**	1.670	1.567	**1.859**	–
1.670	**1.981**	1.430	**1.892**	1.619	**1.986**	–
1.755	–	1.482	–	1.713	–	–
1.802	–	1.529	–	1.760	–	–
1.896	–	1.572	–	**1.844**	–	–
1.995	–	1.661	–	**1.901**	–	–
–	–	1.708	–	–	–	–
–	–	1.760	–	–	–	–
–	–	**1.849**	–	–	–	–
–	–	**1.934**	–	–	–	–
–	–	**1.995**	–	–	–	–
2.047	2.084	2.075	2.099	2.033	2.075	2.315
2.226	2.169	2.169	2.202	2.122	2.211	2.390
2.291	2.343	2.221	2.263	2.226	2.277	**2.517**
2.353	**2.527**	2.305	2.437	2.367	2.348	**2.639**
2.418	**2.644**	2.357	**2.682**	2.447	**2.592**	**2.748**
2.461	2.762	2.447	2.823	**2.602**	**2.687**	2.992
2.564	2.865	**2.630**	2.889	**2.654**	2.809	
2.691	–	**2.682**	–	2.729	2.912	–
2.809	–	2.865	–	2.781	–	–
–	–	–	–	2.823	–	–
–	–	–	–	2.875	–	–
3.091	**3.027**	**3.002**	3.138	**3.002**	**3.049**	3.223
3.148	**3.133**	**3.096**	**3.463**	**3.190**	3.214	–
3.204	**3.383**	**3.195**	–	**3.416**	**3.369**	–
3.345	3.646	3.242	–	3.609	**3.435**	–
3.543	–	**3.420**	–	–	3.670	–
3.623	–	3.651	–	–	–	–
3.689	–	3.754	–	–	–	–
3.778	–	3.891	–	–	–	–
3.844	–	–	–	–	–	–
3.943	–	–	–	–	–	–
4.366	4.008	4.023	4.037	–	–	**4.220**
4.587	**4.135**	**4.117**	**4.300**	–	–	**4.300**
–	**4.244**	**4.164**	–	–	–	4.582
–	–	4.752	–	–	–	–
5.504	–	–	–	–	–	5.297

Chapter 8

Conclusion and Discussion

This chapter presents a brief discussion and conclusion of the findings of this study. The results will be summarized and their significance will be discussed. Lastly, possible and planned future works related to SQUID magnetometers are considered.

8.1 Summary of the results

The frequency content of both the SQUID and Fluxgate data-sets show a number of recurring frequency peaks. Here, only the peaks that were present in both the SQUID's and Fluxgate's, x and z components data-sets were considered. In 6 out of the 7 days studied, there were recurrence of frequency peaks at 1.5, 1.6, 1.7, **1.9**, 2.0, 2.2, 2.3, **2.6**, 2.7 and 2.9 mHz. Frequency peaks at 1.1, **1.3**, 1.4, 1.8, 2.8 and 3.2 mHz appeared in 5 of the 7 storm days. While frequency peaks at 1.0, 1.2, 2.1, 2.4, 3.0, 3.1 and **3.4** mHz only recurred in 4 of the 7 days. Frequency peaks at 2.5, 3.6, 3.7 and **4.2** mHz were only present in 3 of the 7 days. Note that only frequency peaks that were within ± 0.1 mHz from a given frequency peak named above were considered to fall under that frequency peak. The presence of the so-called magic frequencies, in bold, further supports the analogy that most geophysical phenomena resonates at milli-Hertz frequency range.

The correlation between the SQUID and Fluxgate data-sets was as good as expected. The correlation of the frequency content between the SQUID and Fluxgate data-sets for each storm was as follows: Storm 1 = 93.11 %, Storm 2 = 100 %, Storm 3 = 84.78 %, Storm 4 = 89.01 %, Storm 5 = 90.95 % and Storm 6 = 84.03 %. The overall correlation between the SQUID and Fluxgate data-sets for this study was thus 90.31 %, with the correlation at the worst case being 84.03 %. The SQUID system and the Fluxgate magnetometer are within 50 m from each other, hence this good correlation. Looking at the comparison of the SQUID and Fluxgate data, its clear that all the prominent frequency peaks present in the Fluxgate data coincide with the peaks contained in the

SQUID data. However, the Fluxgate data did not always contain all prominent frequency peaks present in the SQUID data.

8.2 Conclusion

The correlation obtained from this study is far better than the correlation from the previous study [9]. From the previous study, the overall (average) correlation was 66.8 %, with the correlation being 59 % at the very least and 75 % at best. The main reason the correlation was not as high as it might be, was due to the distances between the SQUID system and the 3 Fluxgates from which the data-sets were obtained (the Fluxgates were all located more than 500 km away from the SQUID). For the study on the Hermanus data the overall correlation was found to be 90.95 %. Moreover, at the very best the correlation was as high as 100 %, with the lowest correlation obtained being 84.03 %. The high correlation obtained from this study was to be expected since the SQUID and Fluxgates used for this study are located within 50 m from each other. Being in such close proximity, the results obtained in this study are more reliable and gives more confidence in the comparison.

Moreover, this proximity also help in isolating signals (frequency peaks) that can be detected by the SQUID magnetometer, but not the Fluxgate. For this study, SQUID data always showed good coincidence with Fluxgate data, but in some cases such as Storms 3 and 4, for instance, the were some prominent frequency peaks in the SQUID data that were absent in the Fluxgate data. Those frequency peaks appeared in the SQUID's x component data for Storms 3 and 4, and in both cases they were within the $4 - 6$ mHz frequency range. These frequency components are possibly due to near-field sources, i.e. sources that only affect the SQUID, but not the Fluxgate, such as fluctuations of air pressure inside the SQUID hut as the wind buffets the door, or possibly some other effect localized to the SQUID measurement system, control electronics or interface cables that respond to interference, but does not affect the fluxgate.

The correlation obtained in this study further supports and gives more confidence to the previous study. The objective of the previous study was to validate the used of SQUID magnetometers as valid instruments to be used in Space Weather or geophysical research. With the correlation obtained in that study, it was concluded that the SQUID magnetometers can thus be used as reliable Space Weather research instruments. Since the correlation obtained in this study is far better than the one from the previous study; it is now clear that SQUID magnetometers can yield the same results as Fluxgate magnetometers, if not better. Thus, SQUID magnetometers can be valid and reliable Space Weather research instruments. The use of SQUID magnetometers for Space Weather or geophysical research over conventional magnetometers, like Fluxgates, promises to yield far better results than these magnetometers.

SQUID magnetometers are not necessarily superior to other conventional magnetometers. However, their high sensitivity and broad bandwidth, gives them an upper hand when compared to other magnetometers. For instance, SQUID magnetometers can be sampled up to 500 kHz whereas Fluxgates often have a low cut-off frequency. This means that SQUIDs can study various Space Weather or geophysical phenomena that resonates at higher frequencies, which Fluxgates will not be able to study due to their limited bandwidth. On top of that, SQUID magnetometers are more sensitive than most other magnetometers. The high sensitivity enable SQUID magnetometers to measure very faint geomagnetic signals. The combined broad bandwidth and high sensitivity, thus give SQUIDs an advantage over most conventional magnetometers.

8.3 Limitations

This study was subject to the limitations and challenges of the SANSA Space Science SQUID system. The SANSA Space Science SQUID system has been operational since late 2012, with only two channels (x and z components) currently operational. This limited the correlative study to be performed using only two channels, the x and z components. The other limitation was that the liquid nitrogen in which the SQUID system operates is currently refilled manually. During liquid nitrogen refilling, the SQUID system is not operational for some time, which means a loss of data. Currently an automatic liquid nitrogen refill system is under development, and a third SQUID channel will be installed in the near future.

Apart from these practical aspects, the SQUID system has its own limitations. The filters limit the bandwidth on the SQUIDs to below 50 Hz and the resolution is currently limited by the data acquisition system (5 pT), not by the SQUID system. Since the SQUID is currently sampled at 125 Hz, filters with cut-off frequency below 50 Hz are needed to avoid aliasing in the SQUID data. To achieve broader bandwidth, the sampling rate must be increased. However, for this study the bandwidth was sufficient being less than 50 Hz. It is worth noting that computing the noise profile of the SQUID indicated that SQUID noise levels are within the acceptable limit. The comparison between the SQUID and Fluxgate noise profiles showed that the SQUID and Fluxgate measurements are both affected by environmental or natural noise at ultra-low frequencies. It would thus require some data processing mathematics to get smaller signals out, if at all possible.

8.4 Recommendations and Future works

The correlation between the SQUID and Fluxgate data-sets was first performed in the previous study [9]. However, the correlation between SQUID

and Fluxgate data-sets obtained from magnetometers in such close proximity, as in this study, has never been done before. There are various techniques discussed in this study that can be of great use moving forward. For instance, the orientation techniques mention in Section 6.3 could be very useful for anyone planning to set up a new SQUID system in the future. The SQUID jumps removal technique, see Section 6.5, also is also a tool that could be of great help since SQUID jumps cannot be completely prevented from occurring. The technique could be improved by creating a technique or computer program that can automatically detect and remove SQUID jumps.

The are also various projects that are currently under development or planned in the near future, to improve the performance of the SANSA Space Science SQUID system. Research shows that SQUID magnetometers may be less noisy when cooled in a zero field [35]. A shielding system to create a zero field when cooling the Hermanus SQUID system, is currently under development. Cooling SQUIDs in a zero field prevents flux trapping in the body, thus preventing $1/f$ noise that is due to fluxon jumping between two or more pinning sites. The development of an automatic nitrogen refilling system is also one other important project to be undertaken, as this will ensure continuous operation of the SQUIDs, thus continuous data. The resolution of the DAQ can also be improved by using a 24-bit DAQ, for instance.

The results obtained is this study further supports the use of the Hermanus SQUID in the proposed long-term **A**dvanced **U**ltrasensitive real-**T**ime **U**pgraded **M**agnetic sensor or **N**etwork (AUTUMN) project for studying earthquake and Space Weather electromagnetic signals. Under the right conditions electromagnetic signals emitted before an earthquake can be detected using a SQUID magnetometer, thus this network could serve as a warning system to natural hazards such as earthquakes. The Hermanus SQUID magnetometer could be used in the future to study geophysical phenomenons, for example, the effect of lightning, rain or strong winds on geomagnetic data. Since the SQUID is also located near the ocean, it can further be used to study the effect of tidal motions on geomagnetic data.

Appendices

Appendix A

Downloading and processing Hermanus SQUID data

A.1 Downloading Hermanus SQUID data

Hermanus SQUID data is available on-site (SANSA Space science SQUID control room) and it can also be downloaded from a server at the Department of Electrical and Electronic Engineering at Stellenbosch University via (`http://geomagnet.ee.sun.ac.za/`). One full day's data, sampled at 125 Hz, is about 1 MB in size and its formatted as follows. The data file contains ten (10) columns of data variables in total, thought couple columns are dummies. The first column is the "*date*", the second being the "*time*" , followed by the "*micro second*", the "*filtered x component*", a dummy column, the "*filtered x component*", a dummy column, "*unfiltered x component*", a dummy column and the "*unfiltered z component*". The dummy columns are provided for future y axis.

A.2 Computing the ASD

The MATLAB code used to compute the Amplitude Spectral Density was adopted from Temwani's theses [9]. The ASD was computed using the Wiener-Khintchine Theorem and the following program shows the resulting frequency spectrum plot.

```
%Computing the Amplitude Spectral Density

clear all
close all
clc

delay = 0*3600+0*60+0; %delay from the beginning of the file
```

```
winlength = 24*3600;  %length of the temporal signal in seconds
%---------------Loading data files-----------------------------
%----------SQUID data file--------
SQH = load('File location\file-name');
%-------Fluxgate data file--------
HER = load('File location\file-name');
%----------------------------------------------------------------
%---Assigning variables to different coloumns from data-sets---
%-------------SQUID--------------
SQHX = SQH(:,4);SQHX = SQHX - mean(SQHX);
SQHZ = SQH(:,6);SQHZ = SQHZ - mean(SQHZ);
%--------------Fluxgate-----------
HERH = HER(:,4);
HERY = HER(:,5);
HERZ = HER(:,6);HERZ = HERZ - mean(HERZ);
%----------------------------------------------------------------
%---------------Deriving the fluxgate's x-component------------
HERD = asin(HERY./HERH);
HERX = HERH .*cos(HERD);HERX = HERX - mean(HERX);
%----------------------------------------------------------------
%----------------Calculating the SQUID sensitivity-------------
dSQHX = max(SQHX) - min(SQHX);
dSQHZ = max(SQHZ) - min(SQHZ);
dHERX = max(HERX) - min(HERX);
dHERZ = max(HERZ) - min(HERZ);
SENSX = dHERX/dSQHX;
SENSZ = dHERZ/dSQHZ;
%--Mutlying the SQUID data with their respective sensitivities-
SQHX = SQHX*SENSX;
SQHZ = SQHZ*SENSZ;
%----------------------------------------------------------------
%--------------------SQUID Spectral Analysis-------------------
SQHN = length(SQHX);
SQHf = 125; %sampling frequency of SQUID data.
SQHdt = 1/SQHf; %sampling rate in seconds
SQHNn2 = 2^nextpow2(SQHN); %number of fft points as a power of 2
SQHf2 = (0:SQHNn2-1)*SQHf/SQHNn2; % frequency axis
time2 = 0:SQHdt:(SQHN-1)*SQHdt; % time axis

SQHX = detrend(SQHX);
SQHZ = detrend(SQHZ);
lag2 = 0.25*SQHN; %define according to whether interested in low
%or high frequencies. For high frequencies lag ~ SQHN
```

```
%---unbiased option scales to the correct amplitude
SQHX = 2*xcorr(SQHX,lag2,'unbiased');
SQHX(1:lag2) = []; % remove correlation at negative lags
% Hann window has best tread off for
fequency resolution and amplitude accuracy
SQHX = 2*SQHX .* hanning(length(SQHX),'periodic');
SQHZ = 2*xcorr(SQHZ,lag2,'unbiased');
SQHZ(1:lag2) = [];
SQHZ = 2*SQHZ .* hanning(length(SQHZ),'periodic');

%Wiener-Khinchin theorem, ESD = energy
%spectral density in nT^2
ESD_squidH = 2*abs(fft(SQHX,SQHNn2)/length(SQHX));
ESD_squidZ = 2*abs(fft(SQHZ,SQHNn2)/length(SQHZ));

%Amplitude spectral density, nT/sqrt(Hz);
ASD_squidH = sqrt(ESD_squidH*(SQHN*SQHdt));
ASD_squidZ = sqrt(ESD_squidZ*(SQHN*SQHdt));
%-------------------------------------------------------------
%-----------------Fluxgate Spectral Analysis ------------------
HERN = length(HERX);
HERdt2 = 24*3600/HERN; HERfs2 = 1/HERdt2;
HERNn2 = 2^nextpow2(1024*HERN);
HERf2 = (0:HERNn2-1)*HERfs2/HERNn2; % frequency axis
time2 = 0:HERdt2:(HERN-1)*HERdt2; % time axis

HERX = detrend(HERX);
HERZ = detrend(HERZ);
HERlag2 = 0.25*HERN;

%---unbiased option scales to the correct amplitude
HERX = 2*xcorr(HERX,HERlag2,'unbiased');
HERX(1:HERlag2) = []; % remove correlation at negative lags
HERX = 2*HERX .* hanning(length(HERX),'periodic');
HERZ = 2*xcorr(HERZ,HERlag2,'unbiased');
HERZ(1:HERlag2) = [];
HERZ = 2*HERZ .* hanning(length(HERZ),'periodic');

ESD_herH = 2*abs(fft(HERX,HERNn2)/length(HERX));
ESD_herZ = 2*abs(fft(HERZ,HERNn2)/length(HERZ));

ASD_herH = sqrt(ESD_herH*(HERN*HERdt2));
ASD_herZ = sqrt(ESD_herZ*(HERN*HERdt2));
```

```
%-------------------------------------------------------------

figure,...
    subplot(2,1,1),...
    plot(1000*SQHf2(1:SQHNn2/2),ASD_squidH(1:SQHNn2/2),'g',...
    1000*HERf2(1:HERNn2/2),ASD_herH(1:HERNn2/2),'r'),...
    grid,legend('SQHX','HERX'),...
    title('Title of the plot',...
    'FontWeight','bold','FontSize',12),...
    ylabel('ASD [nT/{\surd}Hz]','FontSize',12),..
    xlim([1 8]);,...
    subplot(2,1,2),...
    plot(1000*SQHf2(1:SQHNn2/2),ASD_squidZ(1:SQHNn2/2),'g',...
    1000*HERf2(1:HERNn2/2),ASD_herZ(1:HERNn2/2),'r'),...
    grid,legend('SQHZ','HERZ'),...
    ylabel('ASD [nT/{\surd}Hz]','FontSize',12),...
    xlabel('frequency [mHz]','FontSize',12),...
    xlim([1 8]);,...
    samexaxis('abc','xmt','on','ytac','join','yld',1)
```

List of References

[1] J. Clarke and A. L. Braginski, eds., *The SQUID Handbook*, vol. 1. WILEY-VCH Verlag GmbH & Co. KGaA, Weinhem, July 2004.

[2] J. E. Lenz, "A review of Magnetic Sensors," *Proceedings of the IEEE*, vol. 78, June 1990.

[3] J. K. Hargreaves, *The solar-terrestrial environment* . Press Syndicate of the University of Cambridge, 1992.

[4] L. J. J. van Vuuren, A. Kilian, T. J. Phiri, E. P. di Borgo, P. Febvre, E. Saunderson, E. T. Lochner, and D. J. Gouws, "Implementation of an unshielded SQUID as a geomagnetic sensor," 2013.

[5] R. L. Fagaly, "Superconducting quantum interference device instruments and applications ," *REVIEW OF SCIENTIFIC INSTRUMENTS*, vol. 77, 2006.

[6] P. Ripka, "Review of fluxgate sensors," *Sensors and Actuators A*, vol. 33, pp. 129–141, February 1992.

[7] G. Waysand, P. Barroy, R. Blancon, S. Gaffet, C. Guilpin, J. Marfaing, E. P. di Borgo, M. Pyee, M. Auguste, D. Boyer, and A. Cavaillou, "Seismo-Ionosphere Dection by Underground SQUD in the Low-Noise Enviroment in LSBB - Rustrel, France," *European Physics Journal of Applied Physics*, 2009.

[8] G. Waysand, J. Marfaing, E. P. di Borgo, R. Blancon, M. Pyee, M. Yedlin, P. Barroy, M. Auguste, D. Boyer, A. Cavaillou, J. Poupeney, and C. Sudre, "Earth-ionosphere couplings, magnetic storms, seismic precursors and TLEs: Results and prospets of the [SQUID] system in the low-noise underground laboratory of Rustrel-Pays d'Apt," *Comptes Rendus Physique*, vol. 12, pp. 192–202, 2011.

[9] T. J. Phiri, "Correlation between SQUID and Fluxgate magnetometer data for geomagnetic storms," Master's thesis, December 2012.

[10] T. P. Orlando and K. A. Delin, *Foundations Of Applied Superconductivity*, vol. First Edition. Prentice Hall, January 1991.

[11] R. d. B. Ouboter, "Heike Kamerlingh Onnes's Discovery of Superconductivity ," *Scientific American*, March 1997.

[12] M. Tinkham, *Introduction to Superconductivity*. Courier Dover Publications, second ed., June 2004.

[13] J. Dewar, "Preliminary Note on the Liquefaction of Hydrogen and Helium," Royal Institution Proceeding, May 1898.

[14] O. H. Kamerlingh, "Investigations into the properties of substances at low temperatures, which have led, amongst other things, to the preparation of liquid helium," *Nobel Lecture*, December 1913.

[15] O. H. Kamerlingh, "Further experiments with liquid helium. C. On the change of electric resistance of pure metals at very low temperatures etc. IV. The resistance of pure mercury at helium temperatures," Proceedings of the Royal Netherlands Academy of Arts and Sciences (KNAW), May 1911.

[16] P. Cambell, "A superconductivity primer," *Nature*, vol. 330, November 1987.

[17] I. Asimov, *How did we find out about Superconductivity?* . Walker and Co., NY 1988, first ed., 1988.

[18] D. D. Hughes, "The Critical Current of Superconductors : an Historic review," *Low Temperature Physics*, vol. 27, Septemper-October 2001.

[19] M. J. Akhtar, "100 years of superconductivity (1911-2011)," *The Nucleus*, vol. 48, pp. 261–268, December 2011.

[20] R. Kropschot and V. Arp, "Superconducting Magnets," *Cryogenics*, vol. 2, pp. 1–5, September 1961.

[21] J. Bardeen, L. N. Cooper, and J. R. Schrieffer, "Theory of Superconductivity," *Physic Review*, vol. 108, December 1957.

[22] J. E. Hirsch, "BCS theory of superconductivity: it is time to question its validity ," *Physica Scripta*, vol. 80, September 2009.

[23] W. Buckel and R. Kleiner, *Superconductivity : Fundamentals and Applications*. WILEY-VCH Verlag GmbH & Co. KGaA, Weinheim, 2nd ed., May 2004.

[24] D. Larbalestier, D. Alex Gurevich, D. M. Feldmann, and A. Polyanskii, "High T_c superconducting materials for electric power applications," *Nature*, vol. 414, November 2001.

[25] S. Tanaka, "High-Temperature superconductivity ," *Japanese Journal of Applied Physics*, vol. 45, August 2006.

[26] P. W. Anderson, "How Josephson discovered his effect," *Physics Today*, November 1970.

[27] A. A. Golubov, M. Y. Kupriyanov, and E. ll'ichev, "The Current-phase relation in Josephson junction," *Reviews of Modern Physics*, vol. 76, April 2004.

[28] P. W. Anderson and J. M. Rowell, "Probable observation of the Josephson superconducting tunneling effect," *Physical Review Letters*, vol. 10, March 1963.

[29] I. Giaever, "Dection of the ac Josephson effect," *Physical Review Letters*, vol. 14, May 1965.

[30] H. Yoshida, "Application of the AC Josephson-Effect for Precise Measurement ," *IEICE Transactions on Electronics*, vol. E83-C, January 2000.

[31] R. Doll and M. Nabäuer, "Experimental proof of magnetic quantization in a superconducting ring," *Physical Review Letters*, vol. 7, July 1961.

[32] B. S. Deaver and W. M. Fairbank, "Experimental proof for quantized flux in superconducting cylinders," *Physical Review Letters*, vol. 7, July 1961.

[33] N. Byers and C. N. Yang, "Theoritical considerations concerning quantized magnetic flux in superconducting cylinders," *Physical Review Letters*, vol. 7, July 1961.

[34] D. Drung, "High-performance DC SQUID read-out electronics," *Physica C*, vol. 368, pp. 134–140, 2002.

[35] S. Krey, H.-J. Barthelmess, and M. Schilling, "Low-frequency noise and linearity of a YBa_2 Cu_3 O_7 dc superconducting quantum interference device magnetometer in static magnetic fields," *Journal of Applied Physics*, vol. 86, December 1999.

[36] M. J. Caruso, C. H. Smith, T. Bratland, and R. Schneider, "A new perspective on magnetic field sensing," *Nonvolatile Electronics*, December 1998.

[37] I. Tavarozzi, S. Comani, C. D. Gratta, G. L. Romani, S. D. Luzio, D. Brisinda, S. Gallina, M. Zimarino, R. Fenici, and R. D. Caterina, "Current perspective Magnetocardiography: current status and perspectives. Part I: Physical principles and instrumentation," *Italian Heart Journal*, vol. 3, February 2002.

[38] J. Lenz and A. S. Edelstein, "Magnetic Sensors and Their Applications," *IEEE Sensors Journal*, vol. 6, June 2006.

[39] F. Primdahl, "The Fluxgate magnetometer," *Journal of Physics E: Scientific Instruments*, vol. 12, 1979.

[40] P. Ripka, "Advances in fluxgate sensors," *Sensors and Actuators A*, vol. 106, pp. 8–14, 2003.

[41] F. Kaluza, A. Grüger, and H. Grüger, "New and future applications of fluxgate sensors," *Sensors and Actuators A*, vol. 106, pp. 48–51, 2003.

[42] J. Lenz and A. S. Edelstein, "Magnetic Sensors and Their Applications," *IEEE Sensors Journal*, vol. 6, June 2006.

[43] M. Moldwin, *An Introduction to Space Weather*. Cambridge University Press, 2008.

[44] A. K. Singh, D. Siingh, and R. P. Singh, "Space Weather: Physics, Effects and Predictability ," *Surveys in Geophysics*, vol. 31, pp. 581–638, 2010.

[45] K. R. Lang, *The Cambridge Encyclopedia of the SUN*. Cambridge University Press, 2001.

[46] A. Hanslmeier, *The Sun and Space Weather*. Kluwer Academic Publishers, 2002.

[47] K. Scherer, H. Fichtner, B. Heber, and U. Mall, eds., *Space Weather : The Slogan Behind Physics*. Springer-Verlag Berlin Heidelberg, Inc, 2005.

[48] N. O. Weiss, "Sun Structure and Dynamics," *Space Science Reviews*, vol. 124, pp. 13–22, May 2006.

[49] T. Bai and P. A. Sturrock, "Classification of solar flares," *Annual review of astronomy and astrophysics*, vol. 27, pp. 421–467, 1989.

[50] H. Elliot, "The nature of sloar flares," *Planetary and Space Science*, vol. 12, pp. 657–660, February 1964.

[51] J. R. Herman and R. A. Goldberg, *Sun, Weather, and Climate*. U.S. Goverment Printing Office, 1978.

[52] J. M. Wilcox, "The interplanetary magnetic field. Solar origin and terrestrial effects," *Space Science Reviews*, vol. 8, pp. 258–328, April 1968.

[53] R. Nakamura, "Substorms and their solar wind causes," *Space Science Reviews*, vol. 124, pp. 91–101, November 2006.

[54] J. G. Lyon, "The Solar Wind–Magnetosphere– Ionosphere System ," *Science*, vol. 288, June 2000.

[55] Y. Ebihara and Y. Miyoshi, *Dynamic Inner Magnetosphere: A Tutorial and Recent Advances*, vol. 3. Springer Dordrecht Heidelberg London New York, 2011.

[56] X. Li and M. A. Temerin, "The Electron Radiation Belt," *Space Science Reviews*, vol. 95, pp. 569 – 580, 2001.

[57] C. T. Rusell, "The Solar Wind interaction with the Earth's Magnetosphere: A tutorial," *Plasma Science*, vol. 28, pp. 1818–1830, December 2000.

[58] L. F. McNamara, *The Ionosphere: Communication, Surveilance, and Diretion Finding*. Krieger Publishing Company, 1991.

[59] W. H. Campell, *Introduction to Geomagnetic Fields*. Cambridge University Press, 1997.

[60] Y. Kamide and W. Baumjohann, *Magnetosphere - Ionosphere coupling*. Springer-Verlag, 1993.

[61] R. L. McPherron and P. O'Brien, "Predicting Geomagnetic Activity: The D_{st} Index," *Geophysical Monograph*, vol. 125, 2001.

[62] W. D. Gonzalez, J. A. Joselyn, Y. Kamide, H. W. Kroehl, G. Rostoker, B. T. Tsurutani, and V. M. Vasyliunas, "What is a geomagnetic storm?," *Journal of Geophysical Research*, vol. 99, pp. 5771–5792, April 1994.

[63] Y. Kamide, N. Yokoyama, W. Gonzalez, B. Tsurutani, I. Daglis, A. Brekke, and S. Masuda, "Two-step developmentof geomagnetic storms ," *JOURNAL OF GEOPHYSICAL RESEARCH*, vol. 103, pp. 6917–6921, April 1998.

[64] R. L. McPherron, "Magnetic Pulsations: Their Sources And Relation To Solar Wind and Geomagnetic Activity," *Surveys in Geophysics*, vol. 26, pp. 545–592, 2005.

[65] D. Pollock, *A Handbook of Time-Series Analysis, Signal Processing and Dynamics* . Academic Press, 1999.

[66] W. L. Briggs and V. E. Henson, *The DFT : An owner's Manual for the Discrete Fourier Transform*. Society for Industrial and Applied Mathematics, 1995.

[67] P. J. Brockwell and R. A. Davis, *Introduction to Time Series and Forecasting*. Springer-Verlag New York, Inc, second ed., 2002.

[68] P. Bloomfield, *Fourier Analysis of Time Series : An Introduction*. John Wiley & Sons, Inc, second ed., 2000.

[69] R. E. Ziemer, W. H. Tranter, and D. R. Fannin, *Signals and Systems : Continuous and Discrete*. Prentice Hall, fourth ed., 1998.

[70] D. E. Newland, *An Introduction to Random Vibrations, Spectral & Wavelet Analysis*. Dover Publications, Inc, third ed., 1993.

[71] J. F. James, *A Student's Guide to Fourier Transforms : With applications in Physics and Engeneering* . Cambridge University Press, third ed., 2011.

[72] M. J. Lghthill, *An Introduction to Fourier Analysis and Generalised Functons*. Cambridge University Press, 1964.

[73] J. Kauppinen and J. Partanen, *Fourier Transforms in Spectroscopy* . Wiley-VCH Verlag GmbH, 2001.

[74] D. R. Brillinger, *Time Series Data Analysis and Theory*. Society for Industrial and Applied Mathematics, 2001.

[75] S. Winograd, "On computing the Discrete Fourier Transform ," *Proceedings of the National Academy of Sciences of the United States of America*, vol. 73, pp. 1005–1006, April 1976.

[76] S. D. Stearns, *Digital Signal Analysis*. Hayden Book Company, Inc, 1975.

[77] R. W. Harris and T. J. ledwidge, *Introduction to Noise Analysis*. Pion Limited, 1974.

[78] F. Plaschke and K. H. Glassmeier, "Properties of standing Kruskal-Schwarzschild-modes at the magnetopause," *Annales Geophysicae*, vol. 29, pp. 1793 – 1807, 2011.